2

Vol. 77
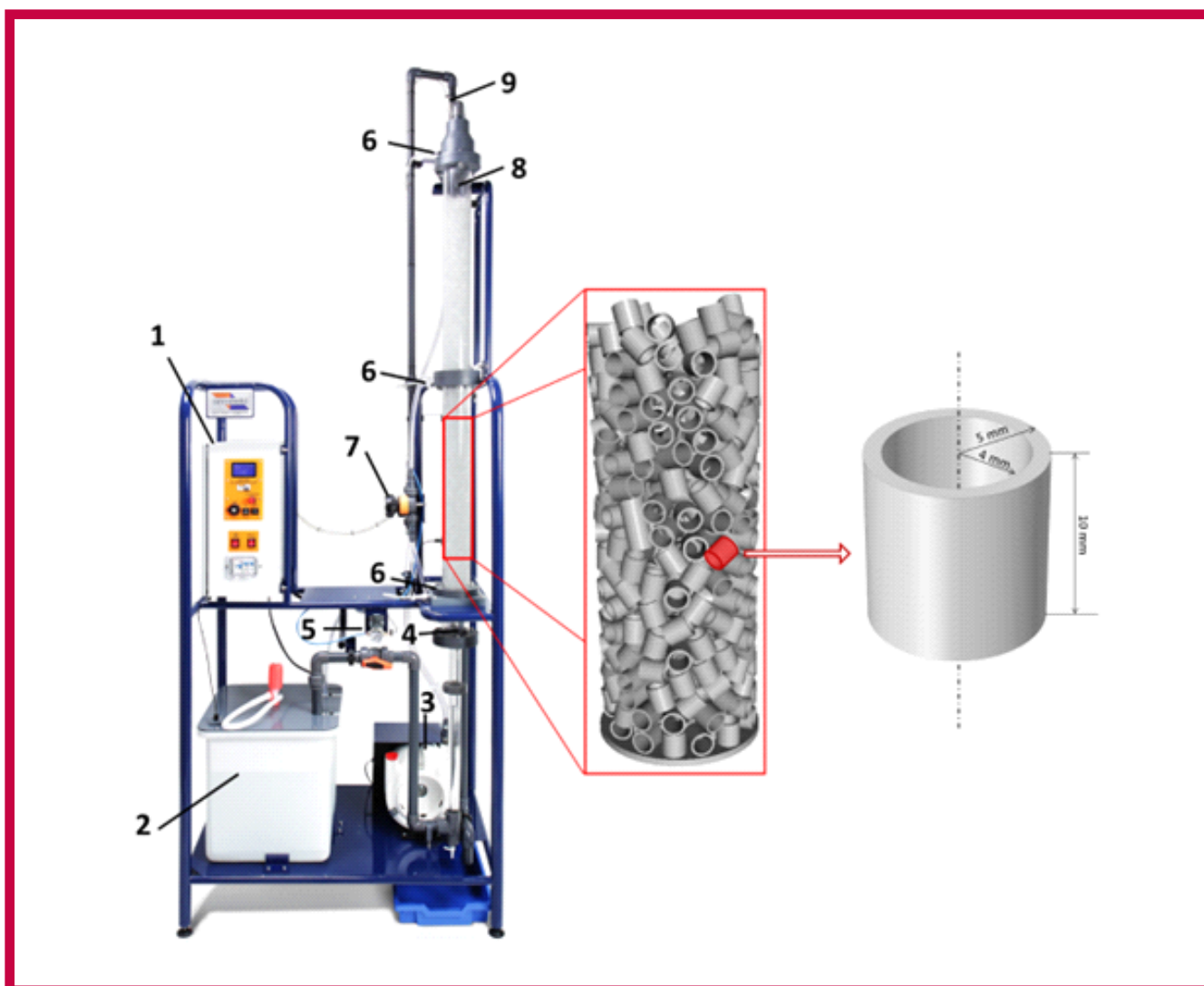
Hemijska industrija

Časopis Saveza hemijskih inženjera Srbije

Chemical Industry

Aktivnosti Saveza hemijskih inženjera Srbije pomažu:

**MINISTARSTVO NAUKE,
TEHNOLOŠKOG RAZVOJA
I INOVACIJA
REPUBLIKE SRBIJE**

Tehnološko-metalurški fakultet
Univerziteta u Beogradu

Prirodno-matematički fakultet
Univerziteta u Novom Sadu

Institut za tehnologiju nuklearnih i
drugih mineralnih sirovina, Beograd

Tehnološki fakultet
Univerziteta u Novom Sadu

Institut za hemiju, tehnologiju i metalurgiju
Univerziteta u Beogradu

Fakultet tehničkih nauka
Univerziteta u Novom Sadu

Tehnološki fakultet
Univerziteta u Nišu, Leskovac

Fakultet tehničkih nauka
Univerziteta u Prištini
Kosovska Mitrovica

Institut IMS, Beograd

DCP HEMIGAL
Leskovac

Elixir Prahovo

Srbija

SHI

Beograd

Chemical Industry
Химическая промышленность

Hemijska industrija

Časopis Saveza hemijskih inženjera Srbije
Journal of the Association of Chemical Engineers of Serbia
Журнал Союза химических инженеров Сербии

| **VOL. 77** | **Beograd, april-juni 2023.** | **Broj 2** |

SADRŽAJ/CONTENTS

Experimental and modeling studies of mass transfer and hydrodynamics in a packed bed absorption column for CO_2 – water system

Dario D. Balaban[1,2], Branislava G. Nikolovski[1], Mitar D. Perušić[2] and Goran S. Tadić[2]

[1]University of Novi Sad, Faculty of Technology Novi Sad, Bulevar cara Lazara 1, 21000 Novi Sad, Serbia
[2]University of East Sarajevo, Faculty of Technology Zvornik, Department of Process Engineering, Karakaj 1, 75400 Zvornik, Republic of Srpska, Bosnia and Herzegovina

Abstract

This paper presents research on hydrodynamics and mass transfer in a packed absorption column. Experimental data on dry column pressure drop, flooding point, and efficiency of absorption of CO_2 in water is obtained on a lab-scale absorption column packed with Raschig rings. Auxiliary parts of equipment together with chemical analyses provide simple monitoring and collecting the data. All obtained data were used to test different mathematical models for a given problem, *i.e.* for determination of the dry column pressure drop, flooding point and the overall gas transfer unit height. For dry column pressure drop, models developed primarily for packed columns described the data the best, with the Billet model generating a 6.54 % mean error, followed by Mackowiak and Stichlmair models. In flooding point calculations, empirical models were tested and models of Lobo, Leva and Takahshi gave the best results. Mass transfer (absorption) experiments gave expected results, since absorption efficiency increased with the increase in the liquid/gas flow rate ratio, *i.e.* with approaching the flooding point. The Onda's model was used to calculate partial mass transfer coefficients in liquid and gas phases based on which the height of the overall gas transfer unit was estimated and subsequently compared with the experimental data. Deviation of calculated and experimental results for the height of the overall gas transfer unit is in the expected range of 0-20 %, with mean value of 15.5 %. In conclusion, the available models for determination of the investigated hydrodynamics and mass transfer parameters in packed absorption columns gave adequate results in comparison to the experimental values.

Keywords: pressure drop; flooding; height of transfer unit.

Available on-line at the Journal web address: http://www.ache.org.rs/HI/

1. INTRODUCTION

Absorption is one of the most important unit operations, primarily due to its application in flue gas cleaning, carbon capture and wastewater treatment. Mass transfer in absorption columns is usually enhanced by column packing, which increases the interphase surface area throughout the column. Proper design and evaluation of packed towers require accurate models to predict hydrodynamics and mass transfer coefficients [1].

The complex nature of the system (multiphase flow through a porous medium, short residence time, mass and heat transfers, flooding phenomenon) has led researchers to develop empirical and semi-empirical mathematical models, considering different parameters affecting the absorption process. Complete models are obtained by considering large databases of results of absorption experiments (geometry of the system, type of packing, flow rates, *etc.*) and fitting the data to the proposed model. This approach can result in models which are not suitable for most of absorption systems, mainly due to the lack of overall data for new absorption systems and geometries.

Since column packings can have complex geometries and different sizes, different approaches were used in modeling of the pressure drop across the column as well as the flooding phenomenon. The most common approach consists of

fitting experimental data to proposed equations resulting in a series of empirical and semi-empirical models, which have been used for decades [2]. In recent times, researchers have taken a turn and began using machine learning [3], and especially computational fluid dynamics to model multiphase flow through porous media [4-9]. This approach has proven to provide more accurate results in assessment of pressure drop in packed columns.

In mass transfer modeling, general models for prediction of mass transfer coefficients are uncommon due to specific characteristics of each absorption system. Since the focus of the present research is on absorption of CO_2 in water, it is worth mentioning that several models can be found in literature for specific systems, usually for those which include common solvents like amines and sodium hydroxide [10-14]. Due to the complex nature of mass transfer in absorption columns, proper design and evaluation of columns require prior research on a lab-scale level for the specific system, providing complete information about mass transfer and hydrodynamics in the column.

The aim of this research was to conduct several types of experiments on a lab-scale packed column for absorption of CO_2 in water and to describe the obtained data with models available in literature. The main focus of experimental work was to obtain data for dry column pressure drop, flooding point, absorption efficiency, and height of the overall gas transfer unit. Also, since the CO_2-water system is rare in the industrial absorption applications, available data are scarce [15], so that the data obtained in these experiments could be used in further research and in more accurate model development.

2. MATERIALS AND METHODS

In order to investigate and analyze hydrodynamics and mass transfer, several types of experiments were performed on a lab-scale packed absorption column Armfield UOP7-MKII ("Armfield", England), Figure 1.
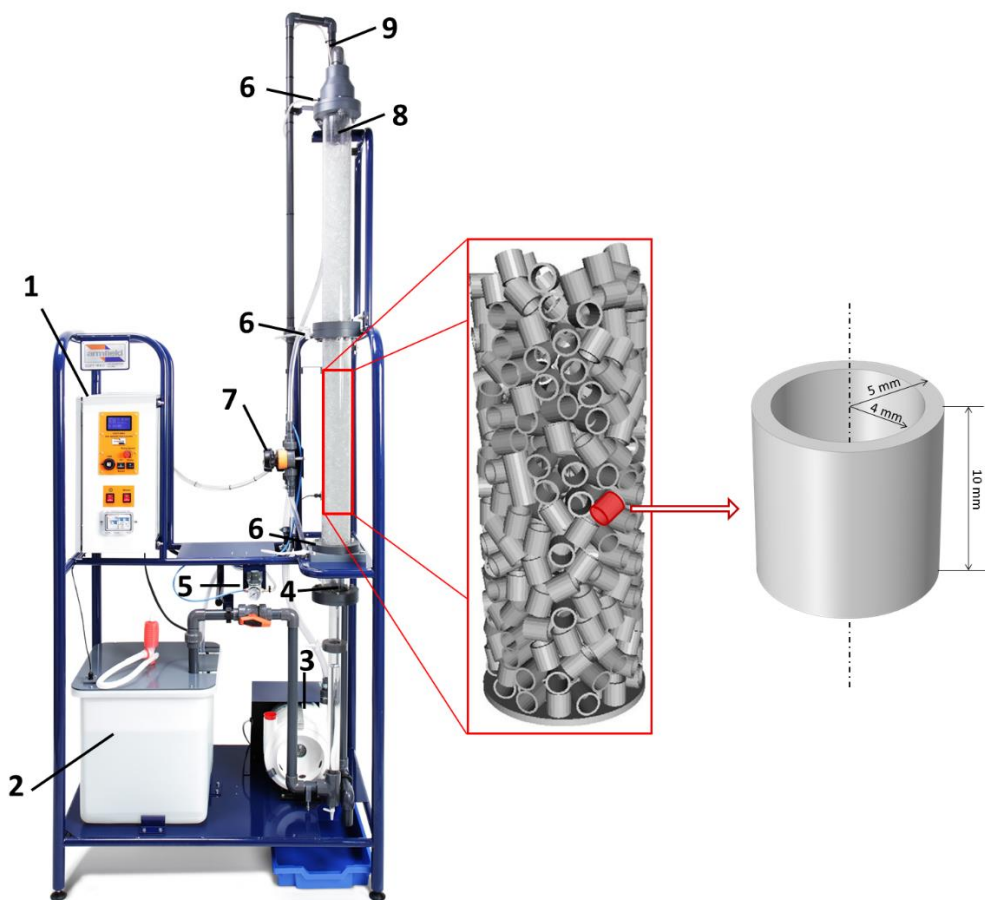

Figure 1. Armfield UOP7-MKII absorption unit system with packing; 1 –control console with a display, 2 – water tank with the pump, 3 – air compressor, 4 – gas mixture inlet, 5 – CO_2 flow control valve, 6 – pressure measurement points, 7 – water flow control valve, 8 – water inlet, 9 – gas mixture outlet [17]

This unit is designed for implementation of counter current CO$_2$/H$_2$O or CO$_2$/dilute NaOH absorption systems, and it features electronic instrumentation for measurement of fluid flow, temperature, CO$_2$ concentration and pressure drop through the column, as well as for control of liquid and gas flow rates and data logging. The column is made of clear acrylic and is packed in two stages with 10×10 mm glass Raschig rings (specific surface area of 440 m^2 m^{-3}). The height of each stage is approximately 0.58 m, with the column diameter of 0.08 m. Pressure measurement points are located at the base, center and top of the column, which enable calculation of pressure drops in the top and bottom stages. The concentration of CO$_2$ in the mixture with air at the top and at the bottom of the column is measured by electronic gas sensors, while electronic flow meters provide accurate measurements of liquid and gas flow rates. Liquid and gas temperature readings are obtained by thermistors in the liquid tank and at the inlet gas line. All data is sent to a connected PC, where real-time logging and subsequent data analyses can be performed. Tap water was used as the liquid phase, whereas ambient air and CO$_2$ from a pressure cylinder ("Messer", Bosnia and Herzegovina) represent the gas phase.

Experiments, as well as overall research, were divided in three stages: determination of dry pressure drop and column flooding (hydrodynamics) and absorption studies (mass transfer).

In dry pressure drop experiments, air flow rate was varied from 20 to 150 l min^{-1}, and pressure drop values for both stages of the column were measured. For modelling purposes, packed bed porosity was determined by the water displacement method, by measuring the total packed bed volume in one section and volume of water needed to completely fill the section.

In flooding experiments, water flow rate was varied from 2 to 8 l min^{-1}, and for each experiment air flow rate was increased until flooding occurred while collecting the data.

In absorption experiments, different combinations of flow rates were used, air flow rate was varied from 40 to 70 l min^{-1}, water flow rate from 1 to 5 l min^{-1}, and CO$_2$ flow rates used were 3 and 4 l min^{-1}. Air and CO$_2$ streams were mixed together before entering the bottom of the column. In order to obtain a complete mass balance, required for further calculations, CO$_2$ concentrations in liquid phase at the bottom and at the top of the column were determined by titration of the liquid samples with 0.0277 M NaOH ("Sineks Laboratory", Bosnia and Herzegovina), as recommended by the equipment supplier. Each analysis was performed three times. Based on the obtained results and known CO$_2$ concentration in the feed air-CO$_2$ mixture, the outlet CO$_2$ concentration is calculated according to the CO$_2$ mass balance for the entire column. Absorption experiments lasted until equilibrium was reached, verified by automatic plotting the outlet gas CO$_2$ concentration against time provided by the data logging software. When the outlet gas CO$_2$ concentration appeared to be constant in a 1 min interval, the experiment was completed.

2. 1. Mathematical model

Several equations and approaches were used to model the pressure drop in packed dry column: the Ergun equation, and the Billet, Mackowiak, Ozahi, Li and Stichlmair models. The equivalent diameter of the Raschig ring was calculated as a Sauter diameter (the diameter of a sphere with the same volume/surface area ratio as a particle of interest), according to the packing dimensions. The Ergun equation [18] was used for pressure drop calculations, Eq. (1), in the transition flow type through a porous medium:

$$\Delta P_{\text{ergun}} = H_c 150 \frac{(1-\varepsilon)^2}{\varepsilon^3} \frac{u_v \mu_v}{d_p^{\,2}} + H_c 1.75 \frac{1-\varepsilon}{\varepsilon^3} \frac{\rho_v \cdot u_v^{\,2}}{d_p} \tag{1}$$

The Billet model [19] takes into account free space available next to the wall of the column and uses a friction factor, which is a function of packing size and material, as shown in Eq. (2):

$$\Delta P_{\text{Billet}} = H_c \psi_0 \frac{a_t}{\varepsilon^3} \frac{F_v}{2K} \tag{2}$$

The Mackowiak model [20] is similar to the Billet model, with the only difference in the friction factor which is here only a function of the modified Reynolds number, as shown in Eq. (3):

$$\Delta P_{\text{Mackowiak}} = H_c \psi_0 \frac{(1-\varepsilon)}{\varepsilon^3} \frac{F_v^{\,2}}{d_p K} \tag{3}$$

Ozahi [21] has also developed a similar model, Eq. (4), with the friction factor being a function of the modified Reynolds number and packing sphericity:

$$\Delta P_{Ozahi} = H_c \left(\frac{276}{Re_o} + 1.76\psi^2 \right) \frac{(1-\varepsilon)}{\varepsilon^3 \psi^2} \frac{\rho_v u_v^2}{d_p} \tag{4}$$

The Li's model [22] represents a modified form of the Ergun equation, which takes into account the packing sphericity, as shown in Eq. (5):

$$\Delta P_{Li} = H_c 150 \frac{(1-\varepsilon)^2}{\varepsilon^3} \frac{u_v \mu_v}{\psi^2 d_p^2} + H_c 1.75 \frac{1-\varepsilon}{\varepsilon^3} \frac{\rho_V u_v^2}{\psi d_p} \tag{5}$$

The Stichlmair model [23] is an empirical model, similar to the Mackowiak model, which takes into account the friction factor which is a function of the Reynolds number, as shown in Eq. (6):

$$\Delta P_{Stichlmair} = H_c 0.75 f_0 \frac{(1-\varepsilon)}{\varepsilon^{4.65}} \frac{\rho_v u_v^2}{d_p} \tag{6}$$

Many authors have developed mathematical models for prediction of gas flow rate at which flooding occurs in a packed column. Almost every available model is empirical, obtained from numerous experimental data. Hence, most of the models represent nonlinear correlations between nondimensional groups of parameters, for example, models of Sherwood [23], Lobo and Leva [2]. These models identify two key nondimensional groups of parameters, as shown in Eqs. (7) and (8):

$$X = \frac{u_L}{u_{flood}} \sqrt{\frac{\rho_L}{\rho_G}} \tag{7}$$

$$Y = \frac{u_{flood}^2}{g} \frac{\rho_v}{\rho_L} \frac{a_t}{\varepsilon^3} \mu_L^{0.2} \tag{8}$$

Also, all three models follow a similar form, Eq. (9):

$\log(Y) = -a \log^2(X) - b \log(X) - c$ (9)

Parameters *a*, *b* and *c* for these models are given in Table 1.

Table 1. Parameters in different flooding point correlations [2]

Model	*a*	*b*	*c*
Sherwood	0.2866	1.0997	1.6784
Lobo	0.252	1.041	1.732
Leva	0.27	1.076	1.705

Also, we have compared two additional models with the experimental data that is the Bertetti and Takahashi models [2], presented by Eqs. (10) and (11), respectively:

$$4.85\mu_L^{0.04} \left(\frac{\rho_v}{\rho_L} \right)^{0.33} u_{flood}^{0.67} + 4.1\mu_L^{0.1} u_L^{0.67} = \frac{6.4\varepsilon}{a_t^{0.33}} \tag{10}$$

$$\sqrt{u_{flood}} \left(\frac{\rho_v \mu_L^{0.2} a_t}{\rho_L \varepsilon^3 g} \right)^{0.25} + \sqrt{u_L} \left(\frac{\mu_L^{0.2} a_t}{\varepsilon^3 g} \right)^{0.25} = 0.552 \tag{11}$$

In mass transfer studies a series of absorption experiments was performed in which inlet and outlet CO_2 concentrations in both liquid in gas phases were determined. The obtained data can be used for comparisons with mathematical model predictions. Here, the Onda's model [24] was used, Eqs. (12) and (13), as its derivation was based on the data in line with the experimental absorption system and the packing type. The Onda's model allows for determination of partial mass transfer coefficients in gas and liquid phases *via* following relations, respectively:

$$\frac{k_G}{a_t}\frac{RT}{D_V} = 2\left(\frac{V}{a_t\mu_V}\right)^{0.7}\left(\frac{\mu_V}{\rho_V D_V}\right)^{\frac{1}{3}}\left(a_t d_p\right)^{-2} \tag{12}$$

$$k_L\left(\frac{\rho_L}{\mu_L g}\right)^{\frac{1}{3}} = 0.0051\left(\frac{L}{a_w\mu_L}\right)^{\frac{2}{3}}\left(\frac{\mu_L}{\rho_L D_L}\right)^{\frac{-1}{2}}\left(a_t d_p\right)^{0.4} \tag{13}$$

where a_w is the wetted specific surface area of the packing, which is calculated From Eq. (14):

$$\frac{a_w}{a_t} = 1 - \exp\left(-1.45\left(\frac{\sigma_c}{\sigma_L}\right)\left(\frac{L}{a_t\mu_L}\right)^{0.1}\left(\frac{L^2 a_t}{\rho_L^2 g}\right)^{-0.05}\left(\frac{L^2}{\rho_L\sigma_L a_t}\right)^{0.2}\right) \tag{14}$$

Liquid and gas diffusivity values were adopted from the literature [24]. In order to model equilibrium phase compositions, the Henry's law was used, since only dilute solutions appeared through the column. The Henry's constant was calculated from the temperature dependence for the given system, as shown in Eq. (15):

$$\ln K_H = a_1 + \frac{b_1}{T_{abs}} + c_1\ln(T_{abs}) + d_1 T_{abs} \tag{15}$$

with the constants a_1 = 159.865, b_1 = -8741.55, c_1 = -21.669 and d_1 = 0.00110259. The Henry's constant is then used to compute the equilibrium partial pressure and concentration of CO_2 in gas phase, Eq (16), which is necessary for determination of the equilibrium line slope, Eq (17).

$$Y^*_{CO_2} = \frac{p^*_{CO_2}}{p_{atm} - p^*_{CO_2}} \tag{16}$$

$$m = \frac{Y^*_{CO_2,in} - Y^*_{CO_2,out}}{X_{CO_2,out} - X_{CO_2,in}} \tag{17}$$

According to the *NTU* method, height of a packed column can be calculated by Eqs. (18) and (19):
$$Z = HTU \cdot NTU \tag{18}$$
$$Z = H_{OG} \cdot N_{OG} \tag{19}$$

N_{OG} represents an overall number of gas phase transfer units and can be calculated numerically by the well-known Eq. (20):

$$N_{OG} = \int_{Y_1}^{Y_2}\frac{dY}{Y_{CO_2} - Y^*_{CO_2}} \tag{20}$$

In this way, the experimental height of the overall gas phase transfer unit can be calculated (for a known height of the packed column), while heights of gas and liquid transfer units can be calculated from the obtained partial mass transfer coefficients, according to Eqs. (21) and (22):

$$H_G = \frac{G_m}{k_G a_w P} \tag{21}$$

$$H_L = \frac{L_m}{k_L a_w C_T} \tag{22}$$

Finally, the value of the height of the overall gas transfer unit can be obtained from the slope of the equilibrium line, eq. (23):

$$H_{OG} = H_G + m\frac{G_m}{L_m}H_L \tag{23}$$

This approach allows for indirect comparison of the used mathematical model and experimental results, through comparison of experimental and calculated heights of the overall gas transfer unit, eq. (23). For all experimental and calculated data, mean absolute percentage error (MAPE) was used as a measure of prediction accuracy.

3. RESULTS AND DISCUSSION

As stated in the experimental section, in pressure drop experiments the air flow rate was varied and pressure drops in the top and bottom parts of the packed column were logged. The obtained values were then summed, to provide the total pressure drop in the column, which was later compared to the values obtained by using different mathematical models. The experiments resulted in expected values, since the pressure drop through a porous media increased exponentially with the increase in gas flow rate. For a given range of air flow rates, the pressure drops were calculated by Eqs (1-6) and the obtained results are displayed in Figure 2.
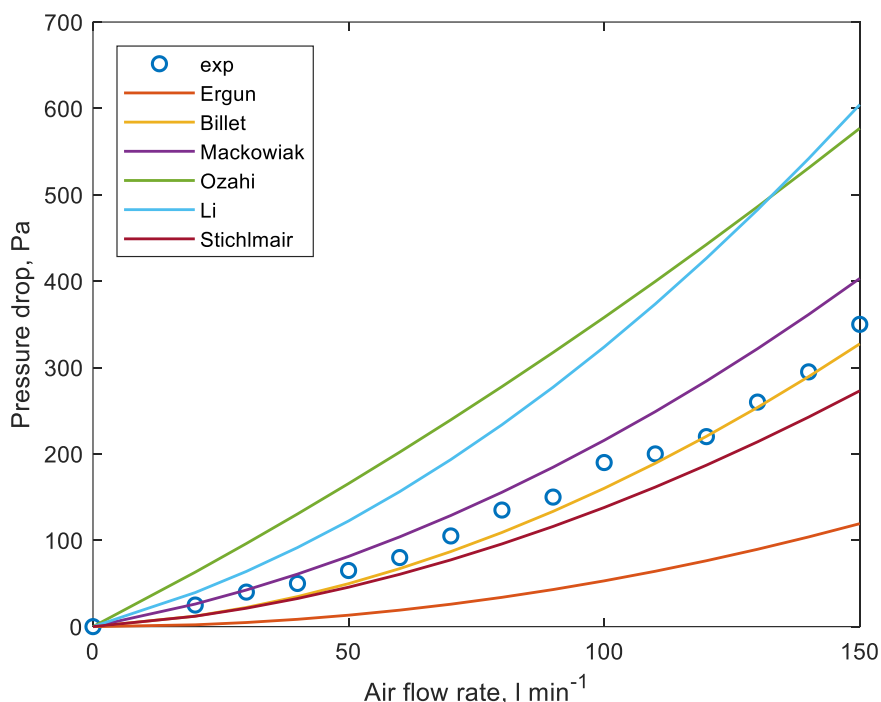
Figure 2. Pressure drop values for different air flow rates: experimental (symbols) and predicted values by different models (lines)

It can be concluded that the models that provided the best results are the models which were developed primarily for packed columns (*i.e.* the Billet, Mackowiak and Stichlmair models), with the MAPE values in the range of ±20 %. The Billet model gave the best approximation, since the obtained MAPE value was 6.5 %.

As stated in the experimental section, in flooding experiments, for a given water flow rate, the air flow rate varied until flooding in the column occurred (Table 2).

Table 2. Experimental air flow rate and superficial velocity at the flooding point for a given water flow rate

$\dot{V}_L$ / l min^{-1}	2	3	4	5	6	7	8
$\dot{V}_{flood}$ / l min^{-1}	190	140	106	75	57	45	35
$u_{flood,exp}$ / m s^{-1}	0.63	0.46	0.35	0.25	0.19	0.15	0.12

Different models were tested against the experimental data, mostly providing adequate results, since the mean percentage error did not differ much from values obtained in the original model development. MAPE values for all of the used models are shown in Table 3.

Table 3. MAPE values for different models in prediction of flooding points

Model	Bertetti	Lobo	Leva	Takahashi	Sherwood
MAPE, %	35.4	13.2	17.4	14.1	23.2

As stated before, models of Sherwood, Lobo and Leva were developed in a similar way, with the same nondimensional groups of parameters, only with different constants in the general equation (see Eq. 9). The obtained experimental values of *X* and *Y*, as well as model equations are displayed in Figure 3.
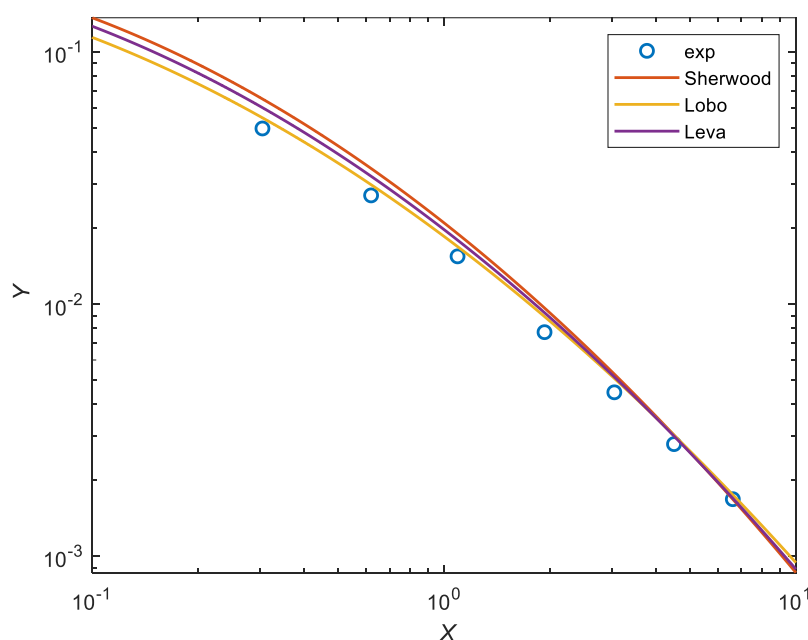
Figure 3. Experimental values (symbols) and predicted by mathematical models (lines, Eq. 9) of nondimensional groups of parameters (Eqs 7 and 8) for flooding points in the packed column

In mass transfer experiments, air, water and CO_2 flow rates were varied, while inlet and outlet CO_2 concentrations were measured and calculated, which allowed for determination of the absorption efficiency, *i.e.* percentage of absorbed CO_2 in each experiment. For constant air and CO_2 flow rates, the increase in water flow rate resulted in an increase in absorption efficiency, as the column system is approaching the flooding point. In every set of experiment, flooding data were used to determine the most preferable water flow rate for given conditions, since the highest absorption efficiency is usually at flow rates slightly below the flooding point. Results of individual experiments are shown in Figure 4.

The results follow linear trends with the highest efficiencies obtained at highest water flow rates. For constant water and CO_2 flow rates, the absorption efficiency decreases with the increase in air flow rate, which is in accordance with the column flooding approach theory.

Heights of the overall gas transfer unit were calculated according to Eqs. (19) and (20) for each experiment (labeled as $H_{OG,exp}$), while the calculated values by the Onda's method are labeled as $H_{OG,calc}$. For each experiment, those two values are compared in order to validate the model with the experimental data. The parity plot of calculated and experimental values of H_{OG} is shown in Figure 5.

It can be concluded that the used model overestimates values of partial mass transfer coefficients, since the calculated height of the overall gas transfer unit is lower than the experimental value. However, the calculation error is mostly in the range of 10-20 %, which is in accordance with model derivation in the original reference [24]. Also, it can be concluded that the error was lower for lower values of H_{OG}, *i.e.* for higher liquid/gas flow rate ratios. The average percentage error for all experiments is 15.5 %.
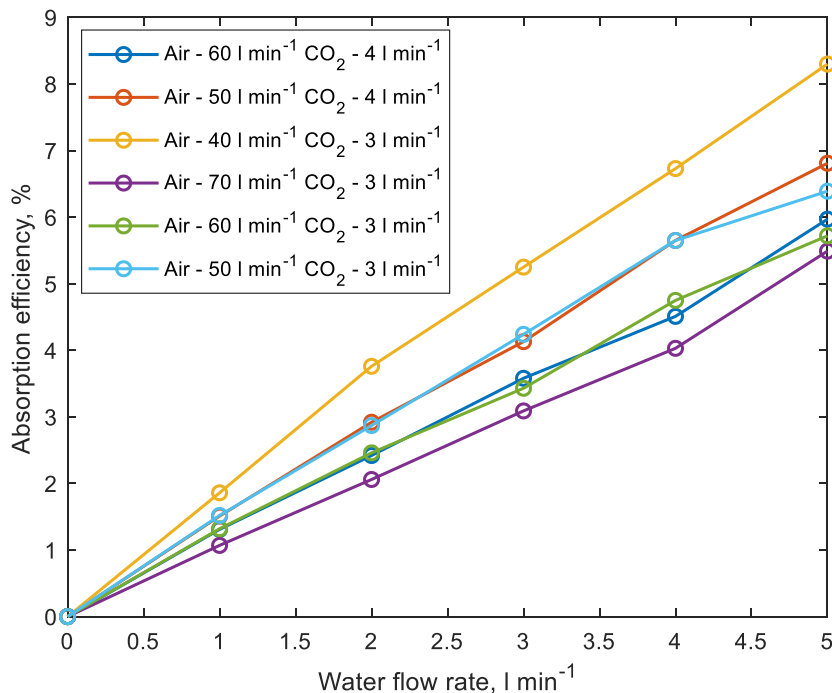
Figure 4. Absorption efficiency as a function of water flow rate for different gas phase compositions and flow rates
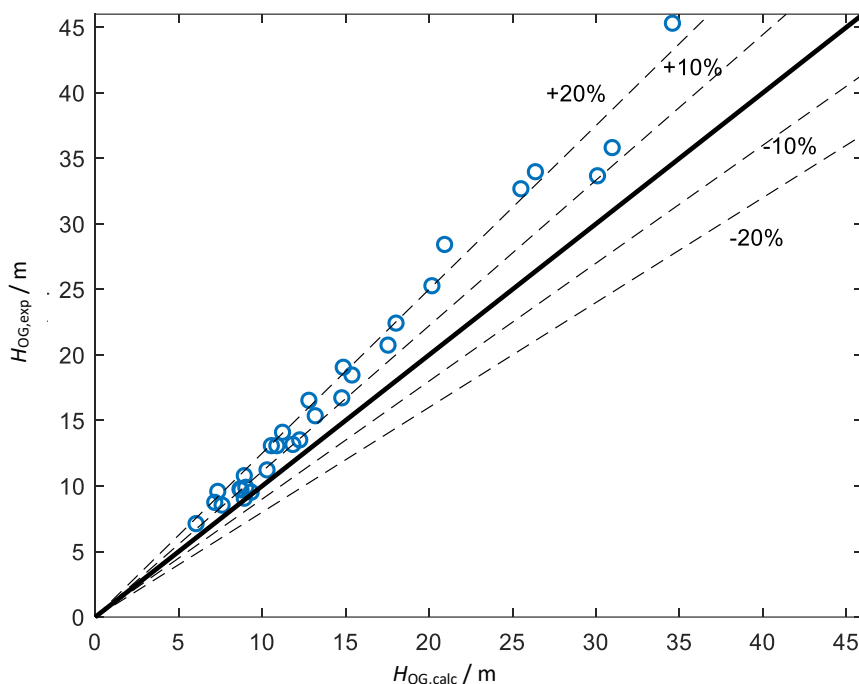
Figure 5. Parity plot for experimental and calculated heights of the overall gas transfer unit

4. CONCLUSION

Mathematical modelling of hydrodynamics and mass transfer in packed absorption columns is a complex procedure, since there are many parameters which can affect mass and momentum transfers in multiphase porous systems. Since absorption is one of the most important unit operations, many authors have developed models, both empirical and theoretical, that describe the mentioned phenomena. In order to provide more experimental data on absorption in packed columns and to model the obtained experimental results, a lab-scale absorption unit was used in the present work. This unit is particularly beneficial for demonstration of basic principles of absorption, flooding points, pressure

drop, mass transfer and effectiveness of CO_2 absorption in water in packed columns. A series of experiments were conducted in order to obtain data for pressure drop across the column at various gas flow rates, flooding points at different flow rates and the absorption efficiency. For each set of experimental data, models found in literature were used in order to describe the obtained data. The Billet model proved to be the most suitable for prediction of dry column pressure drop with the MAPE value of ~6.5 %, which was slightly lower than those found for the models of Stichlmair and Mackowiak. Flooding points were evaluated by using several empirical models, and most of them (*i.e.* Lobo, Leva, Takahashi and Sherwood) gave adequate results, with the MAPE values in the range of 13-23 %, which is acceptable taking into account the complex phenomenon of column flooding. In mass transfer calculations, the Onda's model was used, describing well the obtained experimental results. The obtained results can be used for further investigation of CO_2 – water based packed bed absorption systems, as well as packed bed columns in general, since unconventional Raschig ring size was used as a packing.

5. NOMENCLATURE

a	Parameter in flooding correlation
a_1	Parameter in Henry's equation
a_t / m^2 m^{-3}	Specific surface area of a packing
a_w / m^2 m^{-3}	Wetted specific surface area of a packing
b	Parameter in flooding correlation
b_1	Parameter in Henry's equation
c	Parameter in flooding correlation
c_1	Parameter in Henry's equation
C_T / kmol m^{-3}	Total molar concentration
d_1	Parameter in Henry's equation
D_L / m^2 s^{-1}	Liquid diffusivity
d_p / m	Equivalent diameter of a packing
D_V / m^2 s^{-1}	Diffusivity in vapor
f_0	Friction factor
F_v / m s^{-1} $(kg$ $m^{-3})^{0.5}$	Gas capacity factor
g / m s^{-2}	Gravitational constant
G_m / kmol m^{-2} s^{-1}	Molar flow rate of gas per unit area
H_c / m	Column height
H_G / m	Height of the gas phase transfer unit
H_L / m	Height of the liquid phase transfer unit
H_{OG} / m	Height of the overall gas phase transfer unit
H_{OL} / m	Height of the overall liquid phase transfer unit
HTU / m	Height of transfer unit
K	Wall factor
k_G / kmol m^{-2} s^{-1} Pa^{-1}	Gas film mass transfer coefficient
k_L / m s^{-1}	Liquid film mass transfer coefficient
L / kg m^{-2} s^{-1}	Mass flow rate of liquid per unit area
L_m / kmol m^{-2} s^{-1}	Molar flow rate of liquid per unit area
m	Slope of equilibrium line
N_{OG}	Number of overall gas phase transfer units
NTU	Number of transfer units
P / Pa	Total system pressure
p^* / Pa	Equilibrium partial pressure
R / J $kmol^{-1}$ K^{-1}	Universal gas constant
Re_0	Modified Reynolds number
T / K	Temperature

T_{abs} / K	Absorption temperature
u_{flood} / m s^{-1}	Flooding velocity
u_L / m s^{-1}	Superficial liquid velocity
u_v / m s^{-1}	Superficial gas velocity
V / kg m^{-2} s^{-1}	Mass flow rate of gas per unit area
X	Nondimensional flooding number
X^* / kmol kmol^{-1}	Equilibrium liquid phase content (ratio)
X_{CO_2} / kmol kmol^{-1}	Liquid phase CO_2 content (ratio)
Y	Nondimensional flooding number
$Y^*_{CO_2}$ / kmol kmol^{-1}	Equilibrium gas phase CO_2 content (ratio)
Y_{CO_2} / kmol kmol^{-1}	Gas phase CO_2 content (ratio)
Z / m	Height of packed column

Greek letters

ε	Packed bed porosity
μ / Pa s	Dynamic viscosity
σ_L / N m^{-1}	Liquid surface tension
σ_c / N m^{-1}	Critical surface tension
ρ / kg m^{-3}	Density
ψ	Particle sphericity
ψ_0	Drag coefficient

REFERENCES

[1] Flagiello D, Parisi A, Lancia A, Di Natale F. A review on gas-liquid mass transfer coefficients in packed-bed columns. *ChemEngineering*. 2021; 5(3): 43. https://doi.org/10.3390/chemengineering5030043

[2] Piché S, Larachi F, Grandjean BPA. Flooding capacity in packed towers: Database, correlations, and analysis. *Ind Eng Chem Res.* 2001; 40(1): 47-487. https://doi.org/10.1021/ie000486s

[3] Shahsavand A, Derakhshan Fard F, Sotoudeh F. Application of artificial neural networks for simulation of experimental CO2 absorption data in a packed column. *J Nat Gas Sci Eng*. 2011; 3(3): 518-529. https://doi.org/10.1016/j.jngse.2011.05.001

[4] Marek M. CFD modelling of gas flow through a fixed bed of Raschig rings. *J Phys Conf Ser*. 2014; 530(1): 012016. https://doi.org/10.1088/1742-6596/530/1/012016

[5] Haroun Y, Raynal L. Use of Computational Fluid Dynamics for Absorption Packed Column Design. *Oil Gas Sci Technol.* 2016; 71(3): 43. https://doi.org/10.2516/ogst/2015027

[6] Basha OM, Wang R, Gamwo IK, Siefert NS, Morsi BI. Full-Scale CFD Modeling of Multiphase Flow Distribution in a Packed-bed Absorber with Structured Packing Mellapak 250Y. *Int J Chem React Eng.* 2020; 18(3): 1–17. https://doi.org/10.1515/ijcre-2019-0207

[7] Lu X, Xie P, Ingham DB, Ma L, Pourkashanian M. Modelling of CO_2 absorption in a rotating packed bed using an Eulerian porous media approach. *Chem Eng Sci.* 2019; 199: 302–318. https://doi.org/10.1016/j.ces.2019.01.029

[8] Dixon AG. COMSOL Multiphysics Simulation of 3D Single-phase Transport in a Random Packed Bed of Spheres. *Proc COMSOL Conf Bost.* 2014; 15261(2013): 15261.

[9] Marek M. Gas flow maldistribution in random packed beds of non-spherical particles – A CFD study. *Chem Eng Sci.* 2019; 197: 296–305. https://doi.org/10.1016/j.ces.2018.12.032

[10] Pan W, Galvin J, Huang WL, Xu Z, Sun X, Fan Z, Liu K. Device-scale CFD modeling of gas-liquid multiphase flow and amine absorption for CO_2 capture. *Greenh Gases Sci Technol.* 2018; 8(3): 603–620. https://doi.org/10.1002/ghg.1770

[11] Krauß M, Rzehak R. Reactive absorption of CO_2 in NaOH: An Euler-Euler simulation study. *Chem Eng Sci*. 2018; 181: 199-214. https://doi.org/10.1016/j.ces.2018.01.009

[12] Mores P, Scenna N, Mussati S. A rate based model of a packed column for CO_2 absorption using aqueous monoethanolamine solution. *Int J Greenh Gas Control.* 2012; 6: 21–36. https://doi.org/10.1016/j.ijggc.2011.10.012

[13] Tontiwachwuthikul P, Meisen A, Lim CJ. CO_2 absorption by NaOH, monoethanolamine and 2-amino-2-methyl-1-propanol solutions in a packed column. *Chem Eng Sci.* 1992; 47(2): 381–390. https://doi.org/10.1016/0009-2509(92)80028-B

[14] Lin SH, Shyu CT. Performance characteristics and modeling of carbon dioxide absorption by amines in a packed column. *Waste Manag.* 1999; 19(4): 255–262. https://doi.org/10.1016/S0956-053X(99)00135-X

[15] Ali S, Akhtar J. Hydrodynamics of Packed Bed Column: Study of the Column for the Absorption of CO₂ in Water and its Efficiency. *Mass Spectrom Purif Tech.* 2018; 04(01): 2–6. https://doi.org/10.4172/2469-9861.1000122

[16] Niegodajew P, Marek M. Analysis of orientation distribution in numerically generated random packings of Raschig rings in a cylindrical container. *Powder Technol.* 2016; 297: 193–201. https://doi.org/10.1016/j.powtec.2016.04.024

[17] Armfield. UOP7 MKII – Gas Absorption Column n.d. https://armfield.co.uk/product/uop7-mkii-gas-absorption-column/

[18] Reddy RK, Joshi JB. CFD modeling of pressure drop and drag coefficient in fixed and expanded beds. *Chem Eng Res Des.* 2008; 86(5): 444–453. https://doi.org/10.1016/j.cherd.2007.12.007

[19] Billet R, Schultes M. Modelling of Pressure Drop in Packed Columns. *Trans Znsr Chem Eng.* 1991; 14(6): 167–174. https://doi.org/10.1002/ceat.270140203

[20] Çarpinlioğlu MÖ, Özahi E. A simplified correlation for fixed bed pressure drop. *Powder Technol.* 2008; 187(1): 94–101. https://doi.org/10.1016/j.powtec.2008.01.027

[21] Ozahi E, Gundogdu MY, Carpinlioglu MÖ. A modification on Ergun's correlation for use in cylindrical packed beds with non-spherical particles. *Adv Powder Technol.* 2008; 19(4): 369–381. https://doi.org/10.1163/156855208X314985

[22] Li L, Ma W. Experimental Study on the Effective Particle Diameter of a Packed Bed with Non-Spherical Particles. *Transp Porous Media.* 2011; 89(1): 35–48. https://doi.org/10.1007/s11242-011-9757-2

[23] Stichlmair J, Bravo JL, Fair JR. General model for prediction of pressure drop and capacity of countercurrent gas/liquid packed columns. *Gas Sep Purif.* 1989; 3(1): 19–28. https://doi.org/10.1016/0950-4214(89)80016-7

[24] Onda K, Sada E, Murase Y. Liquid-side mass transfer coefficients in packed towers. *AIChE J.* 1959; 5(2): 235–9. https://doi.org/10.1002/aic.690050220

Eksperimentalna istraživanja i modelovanje prenosa mase i hidrodinamike u apsorpcionoj koloni sa punjenjem za sistem CO₂ – voda

Dario D. Balaban[1,2], Branislava G. Nikolovski[1], Mitar D. Perušić[2] i Goran S. Tadić[2]

[1]Univerzitet u Novom Sadu, Tehnološki fakultet Novi Sad, Bulevar cara Lazara 1, 21000 Novi Sad, Srbija
[2]Univerzitet u Istočnom Sarajevu, Tehnološki fakultetZvornik, Katedra za procesno inženjerstvo, Karakaj 1, 75400 Zvornik, Republika Srpska, Bosna i Hercegovina

(Stručni rad)

Izvod

U ovom radu predstavljeni su rezultati istraživanja o prenosu mase i hidrodinamici u apsorpcionoj koloni sa punjenjem. Eksperimentalno je ispitivana laboratorijska apsorpciona kolona sa Rašiigovim prstenovima i dobijeni su rezultati za pad pritiska, tačke plavljenja i efikasnost apsorpcije CO₂ u vodi. Prateća oprema uređaja i hemijske analize omogućile su jednostavno dobijanje i praćenje podataka. Svi dobijeni rezultati su korišteni za testiranje različitih matematičkih modela za dati problem, *tj.* za pad pritiska u suvoj koloni, za određivanje tačke plavljenja i visine prenosne jedinice u gasnoj fazi. Za pad pritiska u suvoj koloni, modeli primarno razvijeni za kolone sa punjenjem najbolje su opisali eksperimentalne podatke, gde je model Bileta (Billet) dao srednju grešku od ~6.5 %, a prate ga modeli Makovjaka (Mackowiak) i Štihlmera (Stichlmair). U proračunu tačke plavljenja testirani su empirijski modeli, od kojih su najbolje rezultate dali modeli Loboa (Lobo), Leva (Leva) i Takahašija (Takahashi). Eksperimenti prenosa mase (apsorpcije) su dali očekivane rezultate, s obzirom da se efikasnost apsorpcije povećavala sa porastom odnosa protoka tečnost/gas, tj. približavanjem tački plavljenja. Model Onde (Onda) je korišten za određivanje parcijalnih koeficijenata prenosa mase u tečnoj i gasnojfazi, na osnovu kojih je određena visina prenosne jedinice u gasnoj fazi i poređena sa eksperimentalnim podacima. Odstupanje izračunatih i eksperimentalnih rezultata za visinu prenosne jedinice je bilo u očekivanom rasponu od 0-20%, sa srednjom greškom od 15.5 %. Može se zaključiti da dostupni modeli za određivanje datih parametara hidrodinamike i prenosa mase u apsorpcionim kolonama sa punjenjem daju prihvatljive rezultate u poređenju sa eksperimentalno određenim vrednostima.

Ključne reči: pad pritiska; plavljenje; visina prenosne jedinice

Atmospheric release of organic solvents due to hazardous events in the paints and varnishes industry

Danijela J. Stojadinović, Amelija V. Đorđević, Ivan M. Krstić and Jasmina M. Radosavljević

Faculty of Occupational Safety, University of Niš, Niš, Serbia

Abstract

Technogenic risk is the result of creation and development of hazards that originate from accidents in the technosphere. It involves emissions of hazardous industrial substances into the work and natural environments, fires, radioactive contamination, and contamination by toxic substances during their transport and storage. The qualitative and quantitative technogenic risk assessment has to be performed during the use, handling, transport, and storage of hazardous substances if it is decided that specific environmental elements at a specific location are likely to become exposed to hazardous substances, leading to environmental degradation. This paper discusses vulnerability zones – specifically, the high lethality zone and the irreversible effects zone – that are formed due to hazardous events or accidents in the paints and varnishes industry. Accidents are discussed in terms of exposure to solvents classified as hazardous to ecosystem components, the biosphere, anthroposphere, and the human population during their atmospheric dispersion. The vulnerability zones are designated using the REHRA (Rapid Environmental and Health Risk Assessment) methodology and their spatial arrangement is used to perform the risk assessment for the purpose of notifying authorized institutions and the public about a potentially increased risk at the hazard location and/or the immediate vicinity.

Keywords: reference distance; high lethality zone, irreversible effects zone, hazard.

1. INTRODUCTION

Paints and varnishes industry, as a branch of the chemical industry, utilizes a wide variety of hazardous substances (toxic, flammable, and explosive) in production processes, which may cause chemical accidents. These accidents are accompanied with the risk of release of larger amounts of hazardous substances into the environment, leading to pollution and degradation of the affected environmental medium. Human health is most severely affected by outdoor ambient air pollution, which can be caused by fires, explosions, or propagation of toxic dispersing clouds generated during accidents by leaked substances used in the chemical industry.

The paints and varnishes industry utilizes different raw materials and intermediate goods, and technological procedures are so heterogeneous that production of paints and varnishes cannot be described in general terms. Operation of this industry creates different types of water, air, and soil pollution. Therefore, for any environmental risk assessment it is essential to know chemical composition of input as well as substances that leave the technological process in case and enter the environment.

Evaporation of a solvent and mixing of its vapour with air accelerates air flow and generation of dispersion clouds at longer or shorter distances from the emission point. Owing to their toxicity, solvents may have undesirable physiological effects on the exposed population if they exceed the maximum allowed concentrations for ambient air. There are considerable differences in toxic effects of solvents, ranging from fatal toxicity to delayed toxicity long after exposure [1]. Organic solvents are classified as hazardous substances, not only because of their toxicity but also because of their high flammability and explosiveness, which increase the risk of fires that propagate quickly and are not easily suppressed. In

case of hazardous events, physicochemical properties of organic solvents entail different levels of risk both to the health of people exposed and to the environment.

Globally, there have been multiple hazardous events in recent years involving leaks and emissions of organic solvents with accompanying fires and/or explosions and deaths of dozens of people such as: acetic acid leak in Texas, USA, in 2021 [2]; vinyl chloride plant explosion in Mexico and ethylene glycol plant fire in Saudi Arabia, both in 2016 [3]; chemical industry accident of unknown origin in Taiwan in 2016, but subsequent analysis showed the presence of methanol, xylene, and butanol in the air [4]; alcohol explosion in a chemical plant tank in France in 2015, [5]; benzene leak in China in 2014, [6], and many more.

In Serbia, production of paints, varnishes, and other coatings, which involves organic solvents, takes place in about 150 plants with a continuous growing trend [7]. Serbian output was 128,119 t in 2018, 134,583 t in 2019, and 172,792 t in 2020 [8]. In recent years, following accidents in this branch of Serbian industry were recorded: Leskovac, 2006 [9]; near Niš, 2007 [10]; near Pirot, 2013 [11]; near Užice, 2019 [12]; and once again near Niš, 2020 [13].

This paper delineates vulnerability zones, specifically those with fatal outcomes and those with severe undesirable effects on humans and the environment, after paints and varnishes industry accidents involving leaks of organic solvents and formation of dispersion clouds. The vulnerability zone boundaries were calculated by using the REHRA (Rapid Environmental and Health Risk Assessment) methodology based on physicochemical properties and leaked quantities of organic solvents. This paper focuses solely on liquid organic solvents.

2. MATERIALS AND METHODS

2. 1. Organic solvents used in the paints and varnishes industry

Solvents used in the paint and varnish industry belong to different groups and classes of compounds, and they do not have common chemical properties. The simplest classification of solvents is into organic and inorganic solvents. Organic solvents are compounds that convert solid compounds or liquid non-volatile organic compounds into solutions without changing chemically. Organic solvents, which are used in the paint and varnish industry, are applied in mixtures, to which other diluents or fillers are added, to give the solution an appropriate viscosity. Organic solvents used in paints and varnishes are non-colloidal liquids that dissolve basic components and, when a film is formed, evaporate from the coating under normal conditions [14]. Regarding the physical properties, pure solvents are usually clear liquids, heavier or lighter than water, but their vapours are always heavier than air and closer to the ground. Solvent evaporation and mixing of the vapour with atmospheric air accelerates air flow. Physiological effects of organic solvents are produced only under specific conditions and at specific concentrations, which are taken as one of the factors of the solvent toxicity.

As the number and quantities of solvents increase, so does the level of hazard during the work. A large number and variety of solvents (different physical, chemical, and toxic properties) create particular problems in technical terms and in terms of occupational and environmental safety both under normal circumstances and during accidents. This leads to varying levels of health hazard to the exposed people in terms of type and severity of poisoning.

Organic solvents are also highly flammable and explosive substances, which is why their release or leak can cause quick-spreading fires that are difficult to suppress and that generate toxic dispersion clouds. During accidents involving the release or leaks of organic solvents, their volatility is the key property for determining environmental and health risk. Evaporation rate is an important physical property of solvents related to toxicity and it is usually, although not always, proportional to the boiling point. In addition to volatility, another important factor for assessing the hazard of organic solvent toxic effects is the boiling point and vapour pressure. The lower the boiling point of an organic solvent, the higher its volatility, which increases the probability of high vapour concentrations in the atmosphere.

Vapour pressure is also associated with substance toxicity. It is a well-known fact that, under normal external conditions, a highly toxic solvent with a low vapour pressure is less hazardous than a liquid with almost the same toxicity but with a lower vapour pressure. Some methodologies utilize the "risk index" (eq. 1) to assess the risk of organic solvent toxicity in the occupational and environmental atmospheres [15]:

$$Ir = \frac{p}{MDK} \tag{1}$$

where *Ir* is risk index, *p* is vapoure pressure (101.325 kPa at 303 K) and MDK is maximum allowable concentration of organic solvent in the atmosphere, cm^3/m^3

It can be therefore concluded that only a complete study of physicochemical properties of organic solvents can indicate the hazards and harms during the work with these substances and determine the protective measures for occupational and environmental safety.

According to their level of hazard, organic solvents are classified as [16,17]:

- relatively benign solvents, which rarely harm human health under normal work conditions (petrol, ethyl chloride, ethyl acetate*, etc.*);
- low-toxicity solvents, which may affect health under specific work conditions (ethylene glycol, *etc.*);
- medium-toxicity solvents, which may cause permanent health harm under normal work conditions (toluene, xylene, amyl alcohol, trichloroethylene, *etc.*);
- high-toxicity solvents, which may cause permanent health damage in small amounts (benzene, carbon disulphide, methanol, nitrobenzene, *etc.*).

2. 2. Calculation of reference distance and potentially vulnerable zone upon release of organic solvents into the atmosphere

This paper relies on the REHRA methodology for rapid environment and health risk assessment pertaining to immediate effects of sudden release of organic solvents due to an accident in a paints and varnishes factory [16,17]. This methodology was developed for the primary purpose of enabling a quick assessment of the damage scope related to accidents that may originate in the chemical industry. The REHRA methodology is based on the use of a set of specific forms for the assessment and analysis of risks associated with accidents involving emission of hazardous substances. The results thus obtained are implemented in risk management procedures and in the selection of sites for industrial facilities during spatial planning and development of prediction techniques for emergency planning management in factories with increased likelihood of severe accidents. The methodology is also used to determine reference distance zones within which the unwanted effects of accidents are felt and to define vulnerability zone boundaries.

2. 2. 1. Reference distance calculation

Reference distance (*RD*) from the accident epicentre refers to boundaries of the zone within which fatalities among the exposed population are to be expected. The procedure for determining the RD involves integration of hazardous properties of substances (flammability, toxicity, explosiveness, etc.) and their released quantity due to an accident. This method relies on the use of a series of tables for assessment and management of technogenic and environmental risks. The procedure for determining the *RD* includes listing all hazardous substances in the hazard formulation stage of the risk assessment. Having been listed, the hazardous substances are then labelled and classified. The initial parameters for substance classification are the toxicity class and the volatility class. The toxicity class is based on the LC_{50} value of a substance (Table 1) [17]. LC_{50} is the median lethal concentration of a substance that in a defined time interval leads to the death of 50% of experimental animals.

Table 1. Toxicity classes (TOX) of substances based on LC$_{50\ FOR\ RATS\ -\ (4H)}$ [17]

Content, ppm	Toxicity class
0.01 – 0.1	8
0.1 – 1	7
1 – 10	6
10 – 100	5
100 – 1000	4
1000 – 10000	3
10000 – 100000	2

The volatility class is estimated based on the vapour pressure (p_V) at 20°C, boiling temperature (T_B) under normal conditions, or based on operating pressure (*p*), as shown in Table 2 [16,17].

Table 2. Volatility classes (VL) of toxic substances [17]

Physical parameter	Volatility class
Toxic liquids	
$p_V \leq 5$ kPa	1
5 kPa$<p_V \leq 30$ kPa	2
$p_V > 30$ kPa	3
Toxic gases converted to liquid under pressure	
$T_B > $ **-8.15** °C	3
$T_B \leq $ **-8.15** °C	4
Toxic gases converted to liquid by freezing	
$T_B > $ **-28.15** °C	3
$T_B \leq $ -28.15 °C	4
Toxic gases under pressure	
$p < $ 0.3 MPa	2
0.3 MPa $\leq p < $ 2.5 MPa	3
$p \geq$ 2.5 MPa	4

The values shown in Tables 1 and 2 can be used to determine the toxicity class of substances in relation to LC_{50} and the volatility class. Table 3 shows the toxicity classes of substances according to the combination of LC_{50} and volatility class [16,17].

Table 3. Classification of toxic substances based on the sum of the toxicity (TOX) and volatility classes (VL) [17]

TOX + VL	CLASS
< 6	Low
7	Medium
8	High
9	Very high
10 - 12	Extreme

According to physicochemical characteristics of substances and their toxicity, the REHRA methodology provides groups of hazard categories for substances used in the chemical industry [18,19]. Table 4 provides an overview of organic solvents [18] used in the production of paints and varnishes [20], according to their chemical structure, and shows their hazard category according to the REHRA methodology [16,17].

Table 4. Groups of hazard categories of organic solvents used in the production of paints and varnishes [17]

Substance, CAS no.	Physicochemical properties	Group of hazardscat[a]
Aromatic hydrocarbons		
Benzene, 71-43-2	Flammable liquid with vapour pressure <30 kPa at 20°C (Flash point< 20°C)	1 & 3
Toluene, 108-88-3	Flammable liquid with vapour pressure <30 kPa at 20°C (Flash point< 20°C)	1 & 3
Xylene, 1330-20-7	Flammable liquid with vapour pressure <30 kPa at 20°C (Flash point> 20°C)	1 & 3
Naphthalene, 91-20-3	Flammable liquid with vapour pressure <30 kPa at 20°C (Flash point> 20°C)	1 & 3
Alcohols		
Methanol, 67-56-1	Flammable liquid with vapour pressure <30 kPa at 20°C (Flash point> 20°C)	1 & 3
Ethanol, 64-17-5	Flammable liquid with vapour pressure <30 kPa at 20°C (Flash point> 20°C)	1 & 3
Propanol, 71-23-8	Flammable liquid with vapour pressure <30 kPa at 20°C (Flash point> 20°C)	1 & 3
n-Butanol, 71-36-3	Flammable liquid with vapour pressure <30 kPa at 20°C (Flash point> 20°C)	1 & 3
Amyl alcohol, 123-51-3	Flammable liquid with vapour pressure <30 kPa at 20°C (Flash point> 20°C)	1 & 3
Cyclohexanol, 108-93-0	Flammable liquid with vapour pressure <30 kPa at 20°C (Flash point> 20°C)	1 & 3
Ethyleneglycol, 107-21-1	Flammable liquid with vapour pressure <30 kPa at 20°C (Flash point> 20°C)	1 & 3
Benzylalcohol, 100-51-76	Flammable liquid with vapour pressure <30 kPa at 20°C (Flash point> 20°C)	1 & 3
Ethers and acetals		
Ethyl ether, 60-29-7	Flammable liquid with vapour pressure >30 kPa at 20°C	4 & 6
n-Propyl ether, 108-20-3	Flammable liquid with vapour pressure <30 kPa at 20°C (Flash point> 20°C)	1 & 3
Ethyl ether, 60-29-7	Flammable liquid with vapour pressure <30 kPa at 20°C (Flash point> 20°C)	1 & 3

Substance, CAS no.	Physicochemical properties	Group of hazardscat[a]
Aldehydes and ketones		
Acetaldehyde, 75-07-0	Flammable liquid with vapour pressure > 30 kPa at 20°C	4 & 6
Acrolein, 107-02-8	Medium-toxicity liquids	18 & 21
Furfural, 98-01-1	Flammable liquid with vapour pressure <30 kPa at 20°C (Flash point> 20°C)	1 & 3
Acetone, 67-64-1	Flammable liquid with vapour pressure <30 kPa at 20°C (Flash point> 20°C)	1 & 3
Acetic acid, 64-19-7	Flammable liquid with vapour pressure <30 kPa at 20°C (Flash point> 20°C)	1 & 3
Formic acid, 64-18-6	Flammable liquid with vapour pressure <30 kPa at 20°C (Flash point> 20°C)	1 & 3
Esther		
Methylformate, 107-31-3	Flammable liquid with vapour pressure> 30 kPa at 20°C.	4 & 6
Ethylformate, 109-94-4	Flammable liquid with vapour pressure <30 kPa at 20°C (Flash point> 20°C)	1 & 3
Methyl acetate, 79-20-9	Flammable liquid with vapour pressure <30 kPa at 20°C (Flash point> 20°C)	1 & 3
Ethyl acetate,141-78-6	Flammable liquid with vapour pressure <30 kPa at 20°C (Flash point> 20°C)	1 & 3
Chlorinated hydrocarbons		
Chloroform, 67-66-3	Low-toxicity liquids (vapour pressure 21.3 kPa at 20°C)	16 & 17
Carbon tetrachloride, 56-23-5	Low-toxicity liquids (vapour pressure 11.9 kPa at 20°C)	16 & 17
Ethylchloride, 75-09-2	Flammable gas converted to a liquid under pressure	7 & 9
Dichloroethane, 107-06-2	Flammable liquid with vapour pressure <30 kPa at 20°C (Flash point> 20°C)	1 & 3
Trichloroethylene, 79-01-6	Low-toxicity liquids (vapour pressure 9.2 kPa bar at 20°C)	16 & 17
Tetrachloroethylene, 127-18-4	Low-toxicity liquids (vapour pressure 1.9 kPa bar at 20°C)	16 & 17
Chlorobenzene, 108-90-7	Flammable liquid with vapour pressure <30 kPa at 20°C (Flash point> 20°C)	1 & 3
Organic nitrogen compounds		
Aniline, 62-53-3	Flammable liquid with vapour pressure <30 kPa at 20°C (Flash point> 20°C)	1 & 3
Pyridine, 110-86-1	Flammable liquid with vapour pressure <30 kPa at 20°C (Flash point> 20°C)	1 & 3
Acetonitrile, 75-05-8	Flammable liquid with vapour pressure <30 kPa at 20°C (Flash point> 20°C)	1 & 3
Nitrobenzene, 98-95-3	Flammable liquid with vapour pressure <30 kPa at 20°C (Flash point> 20°C)	1 & 3
Organic sulfur compounds		
Carbondisulphide, 75-15-0	Flammable liquid with vapour pressure> 30 kPa at 20°C	4 & 6
Compounds with multiple functional groups		
Methylene glycol, 109-86-4	Flammable liquid with vapour pressure <30 kPa at 20°C (Flash point> 20°C)	1 & 3
Ethylene glycol, 107-21-1	Flammable liquid with vapour pressure <30 kPa at 20°C (Flash point> 20°C)	1 & 3
Diethylene glycol, 111-46-6	Flammable liquid with vapour pressure <30 kPa at 20°C (Flash point> 20°C)	1 & 3
o-Chloroaniline, 95-51-2	Flammable liquid with vapour pressure <30 kPa at 20°C (Flash point> 20°C)	1 & 3

[a]Groups of hazard categories are determined by the REHRA methodology [17].

According to the REHRA methodology, after a substance has been classified into a group of hazard categories, a reference hazard number is assigned depending on the method of storage. For instance, if a substance belongs to the hazard category group 1 & 3 and if it is stored in a storage facility inside a storage tank, its hazard reference number is 1, as shown in Table 5.

Table 5. Classification of types of hazardous substances and their storage methods [17].

Substance type	Substance characteristics	Ref. Hazard No.	Storage method
Flammable liquids	p_V< 3×10⁴ Pa at 20°C	[1]	Storage facility with a storage tank
		[3]	Other
Flammable liquids	p_V> 3×10⁴ Pa at 20°C	[4]	Storage facility with a storage tank
		[6]	Other
Flammable gases	Gas converted to a liquid under pressure	[7]	Storage above ground, truck or rail tank
		[9]	Other
Toxic liquids	Low-toxicity	[16]	Storage facility with a storage tank
		[17]	Other
Toxic liquids	Medium-toxicity	[18]	Storage facility with a storage tank
		[21]	Other

Reference numbers from Table 5 are combined with the maximum quantity that can realistically be released during a single accident according to the matrix shown in Table 6. The reference number points to a single row, while the maximum substance quantity that can be released points to a single column. The combination of the two factors in the matrix determines the category of the effect associated with the event under observation (specified by a letter and a Roman numeral). The propagation boundary is presented as a category marked with a capital letter of the alphabet, and the shape of the effect of the dispersion cloud propagation is marked with a Roman numeral (Table 7).

Table 6. Categories of vulnerability zones according to the distance from the hazard point of origin depending on the quantity of released hazardous substance (Q_i) [16,17]

REF.HAZ. NO.	Q_i / t								
	0-1	1-5	5-10	10-50	50-200	200-1000	1000-5000	5000-10000	>10000
[1]	-	-	-	-	-	AI	BI	BI	CI
[3]	-	-	-	AI	BI	CI	DII	X	X
[4]	-	-	-	-	-	BI	CII	CII	DII
[6]	-	-	-	BII	CII	DII	EII	X	X
[7]	-	AI	BI	CI	DI	EI	FI	X	X
[9]	-	BII	CIII	CIII	DIII	X	X	X	X
[16]	-	-	-	-	-	AII	AII	BII	CIII
[17]	-	-	-	AIII	AII	BII	CII	CII	CII
[18]	-	-	-	AIII	BIII	DIII	EIII	FIII	FIII
[21]	-	BII	CIII	DIII	EIII	FIII	FIII	X	X

Notes: X designates that this substance/quantity combination is not found in regular industry practice; – designates negligible effects

The combinations shown in Table 6 are elaborated in Table 7 in order to determine the category of damage (marked by a letter of the alphabet), reference distance (*RD*) that defines the boundaries of high lethality zones, estimation of the surface area potentially threatened by the accident (*DS*), and the shape of the effect from dispersion cloud propagation (*DF*), marked by the Roman numerals I, II, and III. In this way, the most precise value of the scope of vulnerability will be calculated by interpolating the data from Table 7 with the corresponding data referring to the ranges of released substance quantities (Table 6). This piece of data is particularly important for calculating the impact of hazards on all analyzed environmental components and the human population.

Roman numerals in Table 7 refer to the effect shape as a circle of the dispersion cloud propagation, which centre is the hazard point of origin; numeral II is a semi-circle whose centre is the hazard point of origin, facing leeward; and numeral III is 1/10 of a circle with a point of the hazard point of origin, also facing leeward.

Determination of the effect shape and vulnerability boundaries (Table 7) is essential for assessing the impact of the hazardous substances on all analyzed environmental elements and the human population so that preventive and safety measures can be defined for the designated zones of dispersion cloud propagation.

Table 7. Toxic substance propagation boundaries according to category, with reference distance

Category	*RD* / m	*DF*		
		I	II	III
		DS / ha		
A	0 - 25	0.2	0.1	0.02
B	25 - 50	0.8	0.4	0.1
C	50 - 100	3	1.5	0.5
D	100 - 200	12	6	1
E	200 - 500	80	40	8
F	500 - 1000	300	150	30
G	1000 - 3000	-	-	300
H	3000 - 10000	-	-	1000

2. 2. 2. Calculation of vulnerability zone boundaries after the release of an organic solvent

Assessment of risk severity for ecosystem components, the biosphere, the anthroposphere, and the human population due to a hazardous substance explosion is performed by means of determining two vulnerability zones.

The first vulnerability zone is the high lethality zone, within which fatalities among the exposed population and severe damage to ecosystem components and/or the biosphere and/or the anthroposphere are to be expected. The radius of this zone due to toxic substance dispersion is determined by the following equation [16,17]:

$$RD_d = RD_{min} + \frac{\left(Q - Q_{i_{min}}\right)}{\left(Q_{i_{max}} - Q_{i_{min}}\right)}\left(RD_{max} - RD_{min}\right), \tag{2}$$

where: RD_d is a reference distance that is defined as the radius of the high lethality zone, which can be in the form of a full circle, semicircle or 1/10 of a circle (Tables 6 and 7) and is expressed in meters, RD_{min} – minimum reference distance, RD_{max} is maximum reference distance (Table 7), Q is released quantity (Table 7), $Q_{i\,min}$ is minimum quantity value within the range of hazardous substance release for a given vulnerability zone category (Table 6) and $Q_{i\,max}$ is maximum quantity value within the range of hazardous substance release for a given vulnerability zone category (Table 6).

Another zone that forms during accidents is the irreversible effects zone, within which the expected effects may be severe, but not sufficient to be lethal to the exposed human population. The scope of the irreversible effects zone is estimated by using the impact coefficient I (eq. 3). Multiplying the values of RD_d (high lethality zone radius) with impact coefficient I defines boundaries of the irreversible effects zone, formed due to accidents involving toxic non-flammable substances. The impact coefficient for flammable or explosive substances has the constant value of 2. However, for toxic non-flammable substances, the impact coefficient is a function of LC_{50}, according to the equation [16,17]:

$$I = 0.35 + 0.65\sqrt{\frac{LC_{50\,30min}}{IDLH}} \tag{3}$$

where: $IDLH$ –'immediately dangerous to life or health' concentration of toxic non-flammable substance when inhaled [21,22].

3. RESULTS AND DISCUSSION

Table 8 shows calculated vulnerability zone radii for organic solvents used in the paints and varnishes production and classified in the hazard category group 1 & 3 (Table 4). Substances in this group are flammable liquids with vapour pressure lower than 30 kPa at 20 °C and a flash point lower or higher than 20 °C (Table 4). These substances are categorized as low-toxicity substances. Reference distance for these substances was calculated under the assumption that the substances are stored in a way that yields larger vulnerability zones in case of an accident than the zones when the substances are stored in storage tanks. The calculations were made for the least favourable storage conditions during an accident, corresponding to reference number 3 according to Table 5.

Table 9 shows calculated reference distances for leaks of flammable, toxic, and explosive organic solvents from the hazard category group 4 & 6 (Table 4), whose vapour pressure is higher than 30 kPa at 20 °C. Again, the reference distance is determined for the least favourable storage conditions for organic solvents used in production, corresponding to reference number 6 according to Table 5.

Table 10 shows calculated reference distances for leaks of flammable toxic gases that are converted into liquids under pressure for production purposes. These substances belong to the hazard category group 7 & 9 (Table 4). To calculate the reference distance, reference number 7 was used, referring to the storage of these substances above the ground or their transport in trucks or rail tanks.

Table 11 shows calculated vulnerability zone radii, *i.e.* reference distance, for low-toxicity organic solvents belonging to the hazard category group 16 & 17. The calculations are based on reference number 17 for the least favourable conditions of toxic dispersion cloud propagation after an accident.

Reference distance for medium-toxicity liquid organic solvents from the hazard category group 18 & 21 is calculated for the least favourable conditions of dispersion cloud propagation after an accident. The results are shown in Table 12.

Table 8. Reference distance (RD$_d$) at different released quantities of organic solvents (Q) belonging to the group of hazardous substances with the reference number 3 and their propagation surface area (DS)

Q from 10 to 500 t			Q from 510 to 1000 t			Q from 1100 to 5000 t		
Q / t	RD$_d$ / m	DS / ha	Q / t	RD$_d$ / m	DS / ha	Q / t	RD$_d$ / m	DS / ha
10	0		510	69.375		1100	102.5	
20	6.25		520	70		1200	105	
30	12.5	0.2	530	70.625		1300	107.5	
40	18.75		540	71.25		1400	110	
50	25		550	71.875		1500	112.5	
60	25		560	72.5		1600	115	
70	26.67		570	73.125		1700	117.5	
80	28.33		580	73.75		1800	120	
90	30		590	74.375		1900	122.5	
100	31.67		600	75		2000	125	
110	33.33		610	75.625		2100	127.5	
120	35		620	76.25		2200	130	
130	36.67	0.8	630	76.875		2300	132.5	
140	38.33		640	77.5		2400	135	
150	40		650	78.125		2500	137.5	
160	41.67		660	78.75		2600	140	
170	43.33		670	79.375		2700	142.5	
180	45		680	80		2800	145	
190	46.67		690	80.625		2900	147.5	
200	48.33		700	81.25		3000	150	
210	50.625		710	81.875		3100	152.5	
220	51.25		720	82.5		3200	155	
230	51.875		730	83.125		3300	157.5	
240	52.5		740	83.75		3300	157.5	
250	53.125		750	84.375	3.0	3400	160	
260	53.75		760	85		3500	162.5	6.00
270	54.375		770	85.625		3600	165	
280	55		780	86.25		3700	167.5	
290	55.625		790	86.875		3800	170	
300	56.25		800	87.5		3900	172.5	
310	56.875		810	88.125		4000	175	
320	57.5		820	88.75		4100	177.5	
330	58.125		830	89.375		4200	180	
340	58.75		840	90		4300	182.5	
350	59.375		850	90.625		4400	185	
360	60	3.0	860	91.25		4500	187.5	
370	60.625		870	91.875		4600	190	
380	61.25		880	92.5		4700	192.5	
390	61.875		890	93.125		4800	195	
400	62.5		900	93.75		4900	197.5	
410	63.125		910	94.375		5000	200	
420	63.75		920	95				
430	64.375		930	95.625				
440	65		940	96.25				
450	65.625		950	96.875				
460	66.25		960	97.5				
470	66.875		970	98.125				
480	67.5		980	98.75				
490	68.125		990	99.375				
500	68.75		1000	100	6.00			

Table 9. Reference distance (RD_d) with the released quantity of organic solvents (Q) belonging to the group of hazardous substances with reference number 6 and their propagation surface area (DS)

Q from 10 to 500 t			Q from 510 to 1000 t			Q from 1100 to 5000 t		
Q / t	RD_d / m	DS / ha	Q / t	RD_d / m	DS / ha	Q / t	RD_d / m	DS / ha
10	25		510	138.75		1100	207.5	
20	31.25		520	140		1200	215	
30	37.5	0.4	530	141.25		1300	222.5	
40	43.75		540	142.5		1400	230	
50	50		550	143.75		1500	237.5	
60	53.33		560	145		1600	245	
70	56.67		570	146.25		1700	252.5	
80	60		580	147.5		1800	260	
90	63.33		590	148.75		1900	267.5	
100	66.67		600	150		2000	275	
110	70		610	151.25	6.00	2100	282.5	
120	73.33		620	152.5		2200	290	
130	76.67	1.5	630	153.75		2300	297.5	
140	80		640	155		2400	305	
150	83.33		650	156.25		2500	312.5	
160	86.67		660	157.5		2600	320	
170	90		670	158.75		2700	327.5	
180	93.33		680	160		2800	335	
190	96.67		690	161.25		2900	342.5	
200	100		700	162.5		3000	350	
210	101.25		710	163.75		3100	357.5	
220	102.5		720	165		3200	365	
230	103.75		730	166.25		3300	372.5	
240	105		740	167.5		3400	380	
250	106.25		750	168.75		3500	387.5	40.00
260	107.5		760	170		3600	395	
270	108.75		770	171.25		3700	402.5	
280	110		780	172.5		3800	410	
290	111.25		790	173.75		3900	417.5	
300	112.5		800	175		4000	425	
310	113.75		810	176.25		4100	432.5	
320	115		820	177.5	6.00	4200	440	
330	116.25		830	178.75		4300	447.5	
340	117.5		840	180		4400	455	
350	118.75	6.00	850	181.25		4500	462.5	
360	120		860	182.5		4600	470	
370	121.25		870	183.75		4700	477.5	
380	122.5		880	185		4800	485	
390	123.75		890	186.25		4900	492.5	
400	125		900	187.5		5000	500	
410	126.25		910	188.75				
420	127.5		920	190				
430	128.75		930	191.25				
440	130		940	192.5				
450	131.25		950	193.75				
460	132.5		960	195	40.00			
470	133.75		970	196.25				
480	135		980	197.5				
490	136.25		990	198.75				
500	137.5		1000	200				

Table 10. Reference distance (RD$_d$) with the released quantity of organic solvents (Q) belonging to the group of hazardous substances with reference number 7 and their propagation surface area (DS)

Q from 1 to 45 t			Q from 46 to 450 t			Q from 460 to 900 t			Q from 1000 to 5000 t		
Q / t	RD$_d$ / m	DS / ha	Q / t	RD$_d$ / m	DS / ha	Q / t	RD$_d$ / m	DS / ha	Q / t	RD$_d$ / m	DS / ha
1	0		46	95		460	297.5		1000	500	80
2	6.25		47	96.25		470	301.25		1100	512.5	
3	12.5	0.2	48	97.5	0.3	480	305		1200	525	
4	18.75		49	98.75		490	308.75		1300	537.5	
5	25		50	100		500	312.5		1400	550	
6	30		60	106.67		510	316.25		1500	562.5	
7	35		70	113.33		520	320		1600	575	
8	40	0.8	80	120		530	323.75		1700	587.5	
9	45		90	126.67		540	327.5		1800	600	
10	50		100	133.33		550	331.25		1900	612.5	
11	51.25		110	140		560	335		2000	625	
12	52.5		120	146.67		570	338.75		2100	637.5	
13	53.75		130	153.33	12	580	342.5		2200	650	
14	55		140	160		590	346.25		2300	662.5	
15	56.25		150	166.67		600	350		2400	675	
16	57.5		160	173.33		610	353.75		2500	687.5	
17	58.75		170	180		620	357.5		2600	700	
18	60		180	186.67		630	361.25		2700	712.5	
19	61.25		190	193.33		640	365		2800	725	
20	62.5		200	200		650	368.75		2900	737.5	
21	63.75		210	203.75		660	372.5		3000	750	300
22	65		220	207.5		670	376.25		3100	762.5	
23	66.25		230	211.25		680	380	80	3200	775	
24	67.5		240	215		690	383.75		3300	787.5	
25	68.75		250	218.75		700	387.5		3400	800	
26	70		260	222.5		710	391.25		3500	812.5	
27	71.25		270	226.25		720	395		3600	825	
28	72.5	3.0	280	230		730	398.75		3700	837.5	
29	73.75		290	233.75		740	402.5		3800	850	
30	75		300	237.5		750	406.25		3900	862.5	
31	76.25		310	241.25		760	410		4000	875	
32	77.5		320	245		770	413.75		4100	887.5	
33	78.75		330	248.75	80	780	417.5		4200	900	
34	80		340	252.5		790	421.25		4300	912.5	
35	81.25		350	256.25		800	425		4400	925	
36	82.5		360	260		810	428.75		4500	937.5	
37	83.75		370	263.75		820	432.5		4600	950	
38	85		380	267.5		830	436.25		4700	962.5	
39	86.25		390	271.25		840	440		4800	975	
40	87.5		400	275		850	443.75		4900	987.5	
41	88.75		410	278.75		860	447.5		5000	1000	
42	90		420	282.5		870	451.25				
43	91.25		430	286.25		880	455				
44	92.5		440	290		890	458.75				
45	93.75		450	293.75		900	462.5				

Comparison of propagation zone sizes or the calculated reference distances shown in Tables 8 to 12 is represented in Figure 1, which leads to a conclusion that under the same conditions of organic solvent release/leak, the largest high lethality zones are formed for the group of hazardous substances 18 & 21 with the reference number 21, while the smallest zones are formed for the group of hazardous substances 1 & 3, with the reference number 3, and the group 16 & 17, with the reference number 17.

Table 11. Reference distance (RD$_d$) with the released quantity of organic solvents (Q) belonging to the group of hazardous substances with reference number 17 and their propagation surface area (DS)

Q from 10 to 500 t			Q from 510 to 1000 t			Q from 1100 to 5000 t		
Q / t	RD_d / m	DS / ha	Q / t	RD_d / m	DS / ha	Q / t	RD_d / m	DS / ha
10	0		510	34.688		1100	51.25	
20	1.3167		520	35		1200	52.5	
30	2.632	0.02	530	35.313		1300	53.75	
40	3.947		540	35.625		1400	55	
50	5.263		550	35.938		1500	56.25	
60	6.579		560	36.25		1600	57.5	
70	7.895		570	36.563		1700	58.75	
80	9.211		580	36.875		1800	60	
90	10.526		590	37.188		1900	61.25	
100	11.842		600	37.5		2000	62.5	
110	13.158		610	37.813		2100	63.75	
120	14.474		620	38.125		2200	65	
130	15.789	0.1	630	38.438		2300	66.25	
140	17.105		640	38.75		2400	67.5	
150	18.421		650	39.063		2500	68.75	
160	19.737		660	39.375		2600	70	
170	21.053		670	39.688		2700	71.25	
180	22.368		680	40		2800	72.5	
190	23.684		690	40.313		2900	73.75	
200	25		700	40.625		3000	75	1.5
210	25.313		710	40.938		3100	76.25	
220	25.625		720	41.25		3200	77.5	
230	25.938		730	41.563		3300	78.75	
240	26.25		740	42.188		3400	80	
250	26.563		750	42.5	0.4	3500	81.25	
260	26.875		760	42.813		3600	82.5	
270	27.188		770	43.125		3700	83.75	
280	27.5		780	43.438		3800	85	
290	27.813		790	43.75		3900	86.25	
300	28.125		800	37.813		4000	87.5	
310	28.438		810	44.063		4100	88.75	
320	28.75		820	44.375		4200	90	
330	29.063		830	44.688		4300	91.25	
340	29.375		840	45		4400	92.5	
350	29.688		850	45.313		4500	93.75	
360	30	0.4	860	45.625		4600	95	
370	30.313		870	45.938		4700	96.25	
380	30.625		880	46.25		4800	97.5	
390	30.938		890	46.563		4900	98.75	
400	31.25		900	46.875		5000	100	
410	31.563		910	47.188				
420	31.875		920	47.5				
430	32.188		930	47.813				
440	32.5		940	48.125				
450	32.813		950	48.438				
460	33.125		960	48.75				
470	33.438		970	49.063				
480	33.75		980	49.375				
490	34.063		990	49.69				
500	34.375		1000	50	1.5			

Table 12. Reference distance (RD_d) with the released quantity of organic solvents (Q) belonging to the group of hazardous substances with reference number 21 and their propagation surface area (DS)

| Q from 10 to 490 t			Q from 500 to 1000 t			Q from 1100 to 5000 t		
Q / t	RD_d / m	DS / ha	Q / t	RD_d / m	DS / ha	Q / t	RD_d / m	DS / ha
10	100		500	531.25		980	581.25	
20	125		510	532.292		990	582.292	
30	150	1.0	520	533.33		1000	583.333	
40	175		530	534.375		1100	593.75	
50	200		540	535.417		1200	604.167	
60	220		550	536.458		1300	614.583	
70	240		560	537.5		1400	625	
80	260		570	538.542		1500	635.417	
90	280		580	539.5833		1600	645.833	
100	300		590	540.625		1700	656.25	
110	320		600	541.667	30.00	1800	666.667	
120	340		610	542.708		1900	677.083	30.00
130	360	8.0	620	543.75		2000	687.5	
140	380		630	544.792		2100	697.917	
150	400		640	545.833		2200	708.333	
160	420		650	546.875		2300	718.75	
170	440		660	547.917		2400	729.167	
180	460		670	548.958		2500	739.583	
190	480		680	550		2600	750	
200	500		690	551.042		2700	760.417	
210	501.04		700	552.083		2800	770.833	
220	502.08		710	553.125		2900	781.25	
230	503.125		720	554.167		3000	791.667	
240	504.168		730	555.208		3100	802.083	
250	505.208		740	556.25		3200	812.5	
260	506.25		750	557.292		3300	822.917	
270	507.2912		760	558.333		3400	833.333	
280	508.33		770	559.375		3500	843.75	
290	509.375		780	560.417		3600	854.167	
300	510.418		790	561.458		3700	864.5833	
310	511.458		800	562.5		3800	875	
320	512.5		810	563.542		3900	885.417	
330	513.542		820	564.583		4000	895.833	
340	514.583		830	565.625		4100	906.25	
350	515.625	30.00	840	566.667	30.00	4200	916.667	
360	516.667		850	567.7083		4300	927.083	30.00
370	517.708		860	568.75		4400	937.5	
380	518.75		870	569.792		4500	947.917	
390	519.79		880	570.833		4600	958.333	
400	520.83		890	571.875		4700	968.75	
410	521.875		900	572.917		4800	979.167	
420	522.9167		910	573.958		4900	989.583	
430	523.958		920	575		5000	1000	
440	525		930	576.042				
450	526.042		940	577.083				
460	527.083		950	578.125				
470	528.125		960	579.167				
480	529.167		970	580.208				
490	530.208		980	581.25				
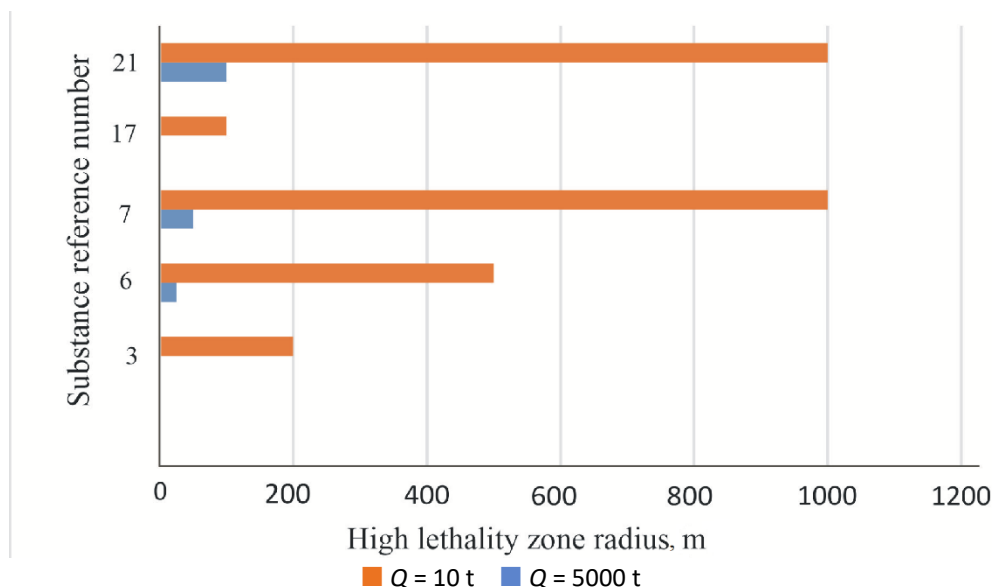
Figure 1. High lethality zone radii upon the release of Q = 10 t and Q = 5000 t of organic solvents according to their hazardous substance reference number

The impact coefficients (eq. 3) of toxic non-flammable substances that are used as organic solvents in paints and varnishes production are given in Table 13.

Table 13. Impact coefficient, I, and reported LC$_{50}$ and IDLH values [22] of toxic organic solvents in the paints and varnishes industry

Non-flammable organic solvent	Impact coefficient	LC_{50}FOR RATS - (0,5h) / ppm [22]	IDLH /ppm [22]
Acrolein	3.68	131 – 0.5 h	5
Chloroform	4.38	19.23 – 0.5h	500
Carbon tetrachloride	6.31	16.80– 0.5 h	200
Trichloroethylene	5.49	62.59– 0.5h	1000
Tetrachloroethylene	5.99	11.32– 0.5 h	150

After determining the reference distance (RD_d) of dispersion cloud atmospheric propagation from the accident point of origin and determining the impact coefficient (I), the following step is to map vulnerability zones and delineate the high lethality zone and the irreversible effects zone. Figure 2 shows an example of a map of the high lethality zone (orange circle on the map), which was calculated and shown in Table 8 above for the hypothetical leak of 120 t of benzene in a model paints and varnishes factory. The yellow doughnut in Figure 2 delineates the irreversible effects zone for this hypothetical event. The irreversible effects zone boundaries were obtained by means of multiplying the reference distance (RD_d) by 2, since benzene is a flammable substance (Table 4). Benzene dispersion has a circular shape for the 120 t leak since it is a toxic substance in the hazard category group 1 & 3 (Table 4) with the reference number 3 (Table 5), so that the shape of propagation (DF) is marked by the Roman numeral I according to Table 7.

Figure 3 shows another example of a map for the hypothetical leak of 250 t of carbon tetrachloride in the same model paints and varnishes factory. The shape of dispersion propagation of this substance, classified in the hazard category group 16 & 17 (Table 4) with the reference number 17 (Table 5), is a semi-circle with a centre at the point of origin of the leak and facing leeward, which is marked by the Roman numeral II according to Table 7. The reference distance for the leak of organic solvents in group 16 & 17 with the reference number 17 is given in Table 11, while the calculated impact coefficient for carbon tetrachloride is given in Table 13. The irreversible effects zone boundaries for this leak were obtained by multiplying the reference distance by the impact coefficient provided in Table 13.
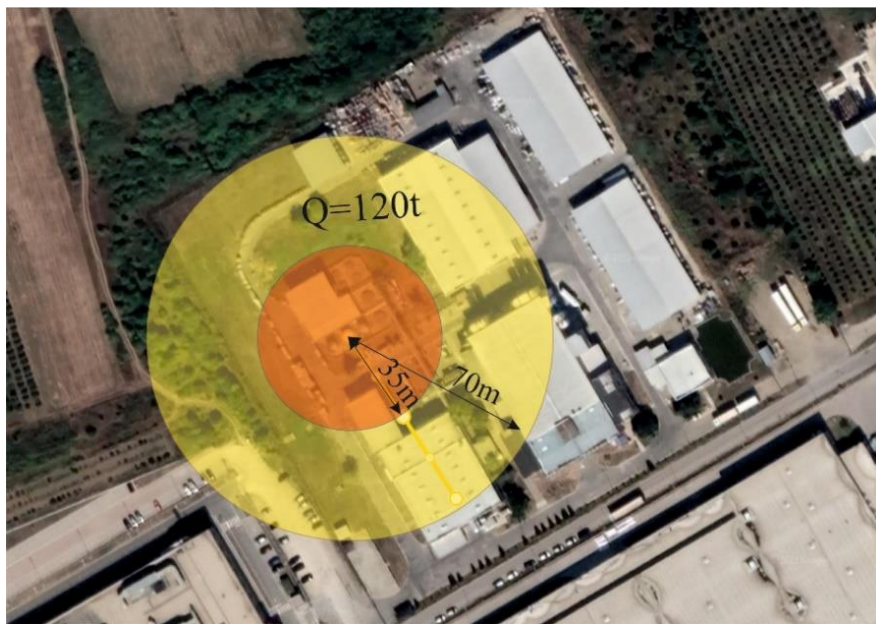
Figure 2. High lethality zone (orange) and irreversible effects zone (yellow) for a hypothetical leak of 120 t of benzene in a model paints and varnishes factory

Figure 3. High lethality zone (orange) and irreversible effects zone (yellow) during the hypothetical leak of 250 t of carbon tetrachloride in a model paints and varnishes factory

The shape of hazardous dispersion propagation of a substance emitted into the atmosphere during an accident may also be 1/10 of a circle, in addition to a full and semi-circle, with the release/leak point of origin facing leeward. Figure 4 shows the map of a hypothetical leak of 5,000 t of acrolein (C_3H_4O) in a model paints and varnishes factory. Acrolein belongs in the 18 & 21 group of hazardous substances (Table 4). For the leak of 5,000 t under conditions defined by the reference number 21, the reference distance is given in Table 12 and the impact coefficient in Table 13. As in the previous case, the irreversible effects zone was determined by multiplying the reference distance by the impact coefficient, and it is shown in yellow in Figure 4, while the high lethality zone is shown in orange. The shape of hazardous propagation is marked by the Roman numeral III (Table 7) and defined as 1/10 of a circle with the release and/or leak point of origin facing leeward.

Figure 4. High lethality zone (orange) and irreversible effects zone (yellow) during the hypothetical leak of 5000 t of acrolein in a model paints and varnishes factory

Every possible case of release or leak of organic solvents used in paints and varnishes production can be represented on a map based on their calculated reference distances, given in Tables 8-12, and their calculated impact coefficients, given in Table 13. The map representation has practical implications for design analysis and performing the environmental impact assessment study, as it can help predict vulnerability zone propagation through urban areas. Another practical benefit of mapping vulnerability zones pertains to accident events, when it is necessary to determine the vulnerability zone territory in which appropriate safety and mitigation measures should be implemented.

4. CONCLUSION

Processes in chemical industry are inherently not absolutely safe and potentially pose a threat of chemical hazards. During hazardous events in this industry, there is increased likelihood of larger amounts of hazardous substances being released and causing fires, explosions, or toxic gas dispersions. There have been multiple occasions worldwide where chemical accidents happened due to the leak and emission of organic solvents that in turn resulted in fires and/or explosions, killing dozens of people. Since there is a justified need, both globally and in Serbia, for the production of paints, varnishes, and other coatings that require organic solvents, it is necessary to predict dimensions of toxic dispersion clouds propagating after the potential release/leak of these solvents during hazardous events. Severity of the effects of organic solvent explosions on ecosystem components, the biosphere, anthroposphere, and human population depends on physicochemical properties and toxicity of these solvents, as well as on the quantities that form the dispersion clouds. After the analysis of vulnerability zones formed during hazardous events in paints and varnishes production, using the REHRA methodology, the following conclusions can be drawn.

- Atmospheric release/leak of organic solvents, which are flammable liquids with vapour pressure lower than 30 kPa at 20 $^{\circ}$C and flash point below or over 20 $^{\circ}$C, and their dispersions will form high lethality zones that will be smaller than those formed due to release of other solvents under the same conditions. The shape of dispersion propagation is a circle or a semi-circle with the point of origin as the centre and facing leeward. The high lethality zone radius ranges from 0 to 200 m during the release/leak of 10 to 5,000 t of such a solvent. There are considerably more organic solvents with these properties in use in paints and varnishes production than any other organic solvents.

- Comparison of calculated sizes of high lethality zones due to organic solvent release/leak showed that the largest zones would be created due to hypothetical acrolein release/leak. The dispersion cloud is in the shape of 1/10 of a circle facing leeward from the point of release/leak. When the solvent is released/leaked in the quantity from 10 to 5,000 t, the high lethality zone radius ranges from 100 to 1,000 m.

- When emitted, chloroform ($CHCl_3$), carbon tetrachloride (CCl_4), trichloroethylene (C_2HCl_3), and tetrachloroethylene (C_2Cl_4) form a dispersion cloud that propagates in the shape of 1/10 of a circle facing leeward from the point of release/leak. The high lethality zone radius ranges from 0 to 100 m when these solvents are released/leaked in the quantity from 10 to 5,000 t.

- When emitted, ethyl ether ($C_4H_{10}O$), acetaldehyde (C_2H_4O), methyl formate ($C_2H_4O_2$), and carbon disulphide (CS_2) form a dispersion cloud that propagates in the shape of a semi-circle facing leeward. The high lethality zone radius ranges from 25 to 500 m when these solvents are released/leaked in the quantity from 10 to 5,000 t.

- When emitted, ethyl chloride (C_2H_5Cl), which is stored above ground or transported in truck or rail tanks forms a circular dispersion cloud in the atmosphere. The high lethality zone radius ranges from 0 to 1,000 m when ethyl chloride is released/leaked in the quantity from 10 to 5,000 t.

Knowledge of dispersion propagations of the analyzed hazardous organic solvents used in the paints and varnishes industry, as well as in other industries, and their hazard mapping have practical implications in accident prevention and implementation of safety and mitigation measures. Additionally, mapping of dispersion propagation with the designation of vulnerability zones has also practical implications for design analysis and environmental impact assessment for project proposals in process plant design, because it is used to predict hazardous substance dispersion propagations through urban areas.

REFERENCES

[1] Carter RE. *Organic solvents: properties, toxicity, and industrial effects*. New York: Nova Science Publishers; 2011 ISBN: 978-1617618819.

[2] The U.S. Chemical Safety Board. https://www.csb.gov/lyondellbasell-fatal-chemical-release-/?msclkid. accessed 15. August 2022.

[3] Chemical and engineering news. https://cen.acs.org/articles/94/web/2016/04/Chemical-accident. accessed 15. August 2022.

[4] Hazardex. https://www.hazardexonthenet.net/article/111211/Casualties-reported-in-Taiwan-chemical-plant-blast.aspx. accessed 15. August 2022.

[5] The BARPI (Bureau for Analysis of Industrial Risks and Pollutions). https://www.aria.developpement-durable.gouv.fr/fiche_detaillee/47045_en/?lang=en. accessed 15. August 2022.

[6] China Dialogue. https://chinadialogue.net/en/pollution/8142-timeline-china-s-chemical-disasters/. accessed 25. August 2022.

[7] Portal-Srbija. https://www.portal-srbija.com/proizvodnja-veleprodaja-boja-i-lakova. accessed 25. August 2022.

[8] Republički zavod za statistiku, Republika Srbija. https://www.stat.gov.rs/media/5918/industrijska proizvodnja po proizvodima. accessed 25. August 2022.

[9] b92.net. https://www.b92.net/info/vesti/index.php. accessed 25. August 2022.

[10] Mondo. https://mondo.rs/Info/Drustvo/a67909/Ugasen-pozar-u-fabrici-Nijansa-kod-Nisa.html. accessed 27. August 2022.

[11] Južne Vesti. https://www.juznevesti.com/Hronika/Pirot-lokalizovan-pozar-u-fabrici-Suko.sr.html. accessed 27. August 2022.

[12] Srbija Danas. https://www.srbijadanas.com/vesti/hronika/povreden-radnik-u-pozaru-u-fabrici-kod-uzica-nakon-eksplozije-zadobio-teske-opekotine-opasne-po-2019-08-16. accessed 27. August 2022.

[13] Politika. https://www.politika.rs/sr/clanak/461621/Ugasen-pozar-u-magacinu-fabrike-Goeks-kod-Nisa. accessed 27. August 2022.

[14] The Industrial Emissions Directive 2010/75/EU. http://ec.europa.eu/environment/industry/stationary/ied/legislation.htm. accessed 27. August 2022.

[15] Putanov P. *Rastvarači*. Beograd:Tehnička knjiga; 1980. (na srpskom)

[16] *Rapid Environment and Health Risk Assessment, REHRA 2*. Italian Ministry for the environment and territory - Department for Global Environment; 2003.

[17] Đorđević A, Stevanović V. *Ekološki rizik*. Niš: Fakultet zaštite na radu u Nišu, Univerzitet u Nišu; 2020 ISBN 978-86-6093-091-2. (na srpskom)

[18] Classification, Labelling and Packaging of Substances and Mixtures Regulation 1272/2008 of the European Parliament and of the Council. http://ec.europa.eu/environment/chemicals/labelling/index_en.htm. accessed 25. September 2022.

[19] *UN Globally Harmonized System of Classification and Labelling of Chemicals (GHS)*. United Nations; 2015 https://doi.org/10.18356/591dabf9-en.

[20] Smallwood I. *Handbook of Organic Solvent Properties*. New York: John Wiley and Sons; 1996 ISBN: 9780080523781.

[21] NIOSH Chemical Listing and Documentation of Revised IDLH Values (as of 3/1/95). http://www.cdc.gov/niosh/idlh/intridl4.html. accessed 25. September 2022.

[22] Ludwig RH, Cairelli SG, Whalen JJ. *Documentation for Immediately Dangerous to Life or Health Concentrations (IDLHs)*. Ohio:U.S. Department of Health and Human Services, Public Health Service, Centers for Disease Control and Prevention, National Institute for Occupational Safety and Health, Division of Standards Development and Technology Transfer Cincinnati; 1994 https://www.cdc.gov/niosh/idlh/pdfs/1994-IDLH-ValuesBackgroundDocs.pdf.

Disperzija organskih rastvarača u atmosferi pri hazardnom događaju u industriji boja i lakova

Danijela J. Stojadinović, Amelija V. Đorđević, Ivan M. Krstić i Jasmina M. Radosavljević

Fakultet zaštite na radu, Univerzitet u Nišu, Niš, Srbija

(Stručni rad)

Izvod

Tehnogeni rizik proizilazi iz opasnosti koje nastaju pri akcidentima u tehnosferi i obuhvata emisije opasnih materija iz industrije u radnoj i životnoj sredini, požare, kontaminaciju radioaktivnim supstancama, kao i kontaminaciju toksičnim supstancama pri njihovom transportu i skladištenju. Kvalitativno-kvantitativnu procenu tehnogenog rizika potrebno je sprovoditi pri upotrebi, rukovanju, transportu i skladištenju opasnih supstanci, ukoliko se zaključi da postoji mogućnost da će na određenoj lokaciji doći do izlaganja okoline tim supstancama što će dovesti do degradacije životne sredine. U radu je dat prikaz zone ugroženosti koja se formira u vidu zone visoke smrtnosti i zone ireverzibilnih efekata usled hazardnih ili akcidentnih događaja u industriji boja i lakova. Akcidentni događaji se posmatraju sa aspekta formiranja ekspozicije rastvarača pri njihovoj disperziji u atmosferi, a koji se svrstavaju u grupu opasnih supstanci po komponente ekosistema, biosferu, antroposferu i ljudsku populaciju. Zona ugroženosti se u radu utvrđuje primenom metodologije REHRA, a njihovo prostorno definisanje omogućava procenu rizika sa ciljem obaveštavanja nadležnih institucija i javnosti o mogućem povećanom riziku na mestu hazarda i/ili neposrednoj okolini.

Ključne reči: referentna udaljenost, zona visoke smrtnosti, ireverzibilna zona, hazard

Improving the stability of a probiotic product with *Lactiplantibacillus plantarum* 299v by introducing flow pack bags

Gabor I. Katona[1], Davor J. Korčok[1,2], Nada A. Tršić-Milanović[2] and Nataša M. Jovanović-Lješković[1]

[1]Faculty of Pharmacy Novi Sad, Trg mladenaca 5, Novi Sad, Serbia
[2]Abela Pharm d.o.o., Viline vode bb, Belgrade, Serbia

Abstract

Probiotic products are becoming more common in everyday use around the world, while at the same time, the interest of scientists in researching probiotic production and use is increasing. Stability of a probiotic product in pharmaceutical production is affected by the choice of probiotic strain, formulation, and packaging. Packaging is the final stage of production and presents a crucial factor for the stability of probiotic products to maintain declared probiotic viability during the products' shelf life. The present research describes the influence of additional packaging material on the encapsulated probiotic product, which contains *Lactiplantibacillus plantarum* 299v. In specific, the effect of additional blister protection within flow pack bags was investigated. Blisters were made of a chloride/poly-vinylidene chloride/polyethylene-triplex foil (PVC/PVdC/PE foil) and aluminum foil. Viability of probiotic lactobacilli cells protected in blisters only was compared to those packed in flow pack bags filled with nitrogen as an inert gas. Better protection of probiotic cells from oxygen, light, and moisture was determined in the capsules in the latter case. In specific, introduction of additional blister protection in flow pack bags resulted in ~11 % higher probiotic viability when compared to the other blister samples without such protection after 24 months, and therefore it enabled more efficient storage of the product during use.

Keywords: quality of packaging; blisters; preservation of viability; packaging materials.

Available on-line at the Journal web address: http://www.ache.org.rs/HI/

1. INTRODUCTION

The increasingly widespread use of probiotic products worldwide is undoubtedly a result of proven, preventive and beneficial effects of probiotics on the improvement of numerous disorders, primarily in the gastrointestinal system [1]. Therefore, probiotic products are becoming more common in everyday use worldwide.

In recent decades, the most common definition of probiotics has been the one provided by the World Health Organization (WHO) and the Food and Agriculture Organization of the United Nations (FAO), according to which probiotics are: "Live microorganisms which, when administered in adequate amounts confer a health benefit on the host" [2].

Probiotics are microorganisms, bacteria and fungi, which contribute to the host's health by stimulating the growth of beneficial bacteria, suppressing pathogens by inhibiting their mucosal adhesion, and by stimulating production of antimicrobial agents [3]. Probiotics are used in food, as dietary supplements, and as medicines.

One of the most frequent probiotic strains in commercial use is *Lactiplantibacillus plantarum* 299v (*L. plantarum* 299v) [4], which is present in over 60 clinical studies on humans, proving its positive effects on relieving symptoms of irritable bowel syndrome (IBS) and contributing to iron absorption [5]. This strain is safe for human use (QPS list-Qualified Presumption of Safety) and it can survive in conditions of the human gastrointestinal tract by binding to mannose on epithelial cells [6-8].

The use of probiotic microorganisms within pharmaceutical dosage forms is certainly more effective than the use in food because pharmaceutical products usually contain selected probiotic strains with proven positive effects in an optimal formulation and involve monitoring the viability of probiotic cells in clinically confirmed product doses. The therapeutic effect of probiotics is confirmed in a daily dose of 10^8 to 10^{10} probiotic cells [7-9].

The final production phase of a probiotic product with the required number of microorganism cells is essential for preserving the selected strain's activity and, therefore, the product. This research describes the selection of the additional packaging material for encapsulated commercial probiotic products with the strain *Lactiplantibacillus plantarum* 299v. The effect of additional blister protection in flow pack bags was investigated. Blisters were made of a polyvinyl chloride/polyvinylidene chloride/polyethylene-triplex foil (PVC/PVdC/PE foil) and an aluminum foil and then such blisters were packed in flow pack bags filled with inert gas [10].

Based on the previous research on saccharomycetes, this paper aims to select the optimal packaging material for probiotics with lactobacilli, since these microorganisms are more affected by temperature. The number of lactobacilli probiotic cells has to be larger than that of saccharomycetes cells in the final product in order to produce a beneficial effect [10].

The stability of a probiotic product is primarily affected by light, moisture, and oxygen. Other factors that affect the survival of probiotics are temperature, pH value, storage time, water activity, other ingredients, and packaging material [11,12].

Oxygen is one of the key factors influencing the viability (activity of live strains) and stability of a probiotic strain, whether it is a bacterial strain or a yeast strain. Its effect is directly related to the technological process of production, which has to ensure the probiotic strain viability during all production phases as well as during the product shelf life [10,13]. Optimization of the technological production process aims to maintain the probiotic strain characteristics while adhering to all criteria that ensure its quality, bioavailability, and optimal therapeutic effects [6,14]. Prevention of the oxygen effects on the encapsulated probiotic strain provides a more stable probiotic product during its predicted shelf life and primary and secondary packaging materials have the crucial role in this attempt. Primary packaging consists of a material that is in direct contact with the product, while the secondary packaging material is an additional, protective packaging that preserves products packed in the primary packaging. Under the influence of oxygen, probiotic strains have reduced viability [15,16]. The information on the probiotic product declaration has to correspond to the product characteristics, which is the manufacturer's responsibility [17]. To maintain the probiotic viability, it is necessary to use a packaging material that acts as an absolute barrier to oxygen. This precondition is necessary, and this research aims to confirm that the choice of primary packaging material (primary product protection), which was used in this study, should result in the maximum protection for probiotic strains, in this case, lactobacilli. Thus, it was necessary to confirm that the selected packaging materials for blisters and flow pack bags of the encapsulated probiotic product Flobian® capsules will provide the appropriate protection so to meet the requirements for probiotic viability. The studies included investigations of viability and stability. To ensure the stability of the product and the perseverance of crucial characteristics of the probiotic strain, it is, firstly, necessary to limit the influence of oxygen. Therefore, this paper presents a hypothesis that an additional packaging material for blisters would provide greater stability to the encapsulated probiotic strain and, thus, greater efficiency during the shelf life of the product. With this aim, the influence of inert gas (nitrogen) as an additional factor that reduces the effect of oxygen on the probiotic product was also considered in this research.

2. EXPERIMENTAL

2. 1. Active ingredients, excipients, capsule

Lactiplantibacillus plantarum 299v (DSM 9483) was procured as a lyophilized powder from Probi AB (Probi AB, Lund, Sweden).

The following excipients were used: maize starch with 2 % moisture (UniPure FL, Germany), magnesium stearate (Magnesia, Germany), and colloidal silicon dioxide (Evonik, Belgium). For encapsulation, vegetable-origin capsules were used from the manufacturer ACG Lukaps, India.

Commercial dietary product Flobian® capsules were produced by using the listed active substances and excipients by filling capsules made of hydroxypropyl methylcellulose (HPMC) [20].

2. 2. Packaging material

A combination of PVC/PVdC/PE and aluminum foil was used as the primary packaging material, and the following samples were prepared:

1. Samples 1,2 (Flobian 1,2): blister combination of PVC/PVdC/PE foil and aluminum foil. Samples 1 and 2 represent technical replicates.
2. Sample 3 (Flobian 3): blister combination of PVC/PVdC/PE foil and aluminum foil enclosed in a flow pack bag filled with inert gas – nitrogen.

PVC/PVdC/PE foil had the following characteristics: PVC/PVdC/PE foil (polyvinyl chloride/polyvinylidene chloride/ /polyethylene-triplex foil) with the thickness of 383 μm.

For Sample 3, a secondary packaging, flow-pack foil, was used as an additional packaging material (also a triplex foil). This foil for flow pack bags in which the blisters were packed was made of PET/Al/TPE (polyethylene terephthalate/aluminum/transparent polyethylene).

Before sealing the flow pack bags, nitrogen as an inert gas, was injected to the flow pack bags.

2. 3. Production of capsules, blisters, and flow pack bags

A flow chart of the technological process for production of capsules and flow pack bags is presented in Figure 1.
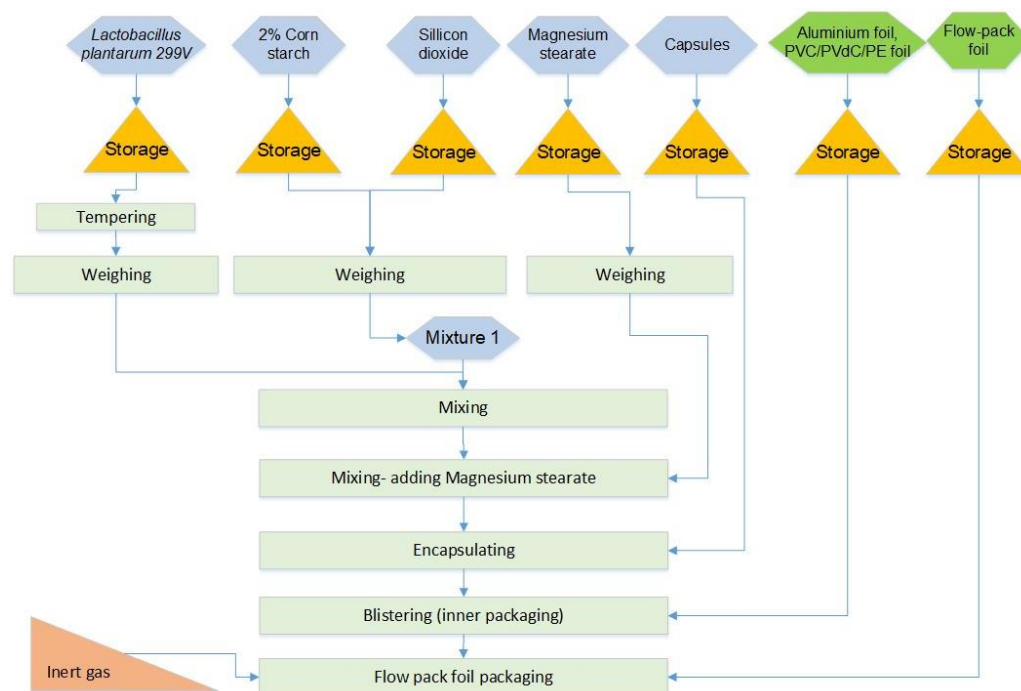
Figure 1. Flowchart of the production process of capsules, blisters, and flow pack bags of Flobian® samples

As presented in Figure 1, the production of capsules begins with weighing the active component and excipients. The active component was measured and dosed inside the capsule in such a way as to provide a minimum of 30×10^9 lactobacilli cells in each capsule immediately after manufacturing. The excipients were weighed and mixed with the active substance, and the encapsulation mass was formed inside a cubical-type device (Omniprojekt, Serbia). The mass was encapsulated, *i.e.* divided into individual doses (capsules) on an automatic encapsulation machine (Macofar, Italy).

During the following production phase, the capsules were blistered in all tested samples by using a blistering machine (Uhlmann, Germany), which combines two foil types: a PVC/PVdC/PE foil and an aluminum foil. These foils were fused to form blister packs containing ten capsules each. The PVC/PVdC/PE and Al blister packs for the sample 3 were then packed within flow pack bags (Sigmaproces, Serbia) made of a PET/Al/TPE triplex foil and filled with nitrogen. Each flow pack bag contained 1 blister pack.

All capsule and blister production phases were performed in strictly controlled ambient conditions at temperatures of 26±1 °C and humidity levels of 32±2 %.

The Flobian® blister is shown in Figure 2, while the appearance of a pack bag is shown in Figure 3.

Figure 2. Front and back side of a standard Flobian® blister pack used in all samples

Figure 3. Flow pack bag with 1 Flobian® blister pack inside (Sample 3)

2. 4. Analytical methods

The number of viable cells of the lactobacilli probiotic strain was determined in capsules within three investigated sample groups. In each sample group, lactobacilli were counted in 20 representative samples of blisters/flow pack bags.

Following the recommendations from the manufacturer, the probiotic strain *Lactiplantibacillus plantarum* 299v was cultivated in a MRS broth (Biokar Diagnostics, France) [18]. The cell count was determined by using the agar plate method (NMKL method, 2007, Probi). Probiotic strain samples in the form of powder (capsule content) were rehydrated in a sterilized purified water solution containing sodium-chloride 0.85 % w/v (Sigma Aldrich, USA), peptone 0.1 % w/v (Sigma Aldrich, USA), and then diluted in serial solutions. Aliquots (0.1 cm^3) of the last two diluted solutions were transferred to the agar plates (Sigma Aldrich, USA), which were then incubated under anaerobic conditions at 37 °C for

two days. After the incubation period, the colonies formed on the plates were counted. The results are presented as the number of colonies or CFU (colony forming units) per powder mass (*i.e.* the capsule content). The described procedure was performed three times, and each result presents the mean value of these three counts as recommended in literature [9,19].

This method of determining the number of lactobacilli was applied immediately after producing the commercial batches of the product Flobian® batch number 190793 for all the investigated samples (July 2019). Then the analysis was repeated at the end of the product shelf life, *i.e.* after 24 months (July 2021). Testing lasted longer than 24 months to confirm the product expiry date and determine whether it could be prolonged over 24 months. The total duration was 30 months, while the testing was performed at 24, 27, and 30 months. All the samples were stored at 25±2 ˚C and at air humidity of 55±5 % RH, which follows the prescribed storage conditions.

2. 5. Statistical analysis

Twenty blister samples in each group were analyzed (Samples 1 - 3). The Shapiro-Wilks test was used for the analysis of distribution normality. One-way ANOVA test and the post-hoc Tukey test was used for the inter-group comparison. The results for the three samples are expressed as the mean values ± standard deviations of all the obtained analyses.

3. RESULTS AND DISCUSSION

To preserve activity of a commercial probiotic product, one of the most important strategies is to increase its low resistance to environmental and technological factors. In this sense, capsules can provide primary protection against environmental factors and represent a dosage form that is easy to swallow [15,16,20].

Packaging of commercial probiotic products with lactobacilli should preserve the cell viability by protecting the cells from external influences. Hydroxypropyl methylcellulose capsules were used in this research as the primary protective element for lactobacilli during product storage at room temperature as shown in literature to preserve viability of this microorganism [20].

Materials containing polyethylene are recommended for protection against moisture and oxygen [16].

This paper is a continuation of previous research, which confirmed that packaging of saccharomycetes probiotics in capsules packed in PVC/PVdC/PE blister packs inserted in flow pack bags is the optimal choice of packaging for that microorganism [10]. The introduction of additional blister protection in flow pack bags greatly contributed to preserving the probiotic viability. Therefore, it enabled better quality of the product before its opening during the product shelf life. As a confirmation of the hypothesis in the present work, samples of Flobian® capsules of the same production batch were divided into three groups and tested simultaneously. Two samples were 20 blisters each without flow pack bags (Samples 1 and 2), and one sample presented 20 blisters each packed in a flow pack bag (Sample 3).

For this commercial dietary product, the manufacturer has declared on the product packaging the required number of living lactobacilli cells, which is at least 20×10^9 per capsule for two years (shelf life).

The obtained viability results together with statistical analysis results are shown in Table 1, together with the changes in average numbers of viable cells over time for each sample group.

Table 1. Cell numbers per capsule in the three tested sample groups at four measurement times with the statistical analysis results

Sample	Mean cell number ± standard deviation, CFU $\times 10^9$ / caps				$P^@$
	Immediately after production- Start	24 months after production	27 months after production	30 months after production	
Sample 1	31.4±1.9	23.0±1.7[aaa]	18.5±1.2[aaa,bbb]	/	<0.001
Sample 2	33.5±2.0	24.5±1.8[aaa]	19.2±1.5[aaa,bbb]	/	<0.001
Sample 3	32.6±1.9	27.5±1.6[aaa]	25.5±2.2[aaa,b]	21.2±2.9[aaa,bbb,ccc]	<0.001
$P^&$	ns	< 0.001 1 *vs.* 3: <0.001 2 *vs.* 3: <0.001	<0.001 1 *vs.*3: <0.001 2 *vs.* 3: <0.001	/	/

Data are presented as means ± standard deviations; *P* from one-way ANOVA test with posthoc Tukey test; ns - nonsignificant;
[aaa] *P* <0.001 *vs*. start; [b] *P* <0.05 *vs*. 24 months; [bbb] *P* <0.001 *vs*. 24 months; [ccc] *P* <0.001 *vs.* 27 months.
[&]difference between different samples in every study point; [@]difference between different times (study points) for any distinct sample

The lactobacilli numbers in the three samples immediately after production were similar amounting to about 32×10^9 lactobacilli per capsule (in the range 31.4-33.5$\times 10^9$ CFU/caps). The differences were not statistically significant. These results indicate that the production process of the encapsulated form of probiotic microorganisms corresponds to the defined technological procedure and that the targeted probiotic activity at the beginning of the shelf life in all three groups of samples is achieved (Table 1).

The stability study of Samples 1 and 2 showed that the number of lactobacilli decreased during the shelf life of 24 months yielding the survival rate of about 73 % without significant difference between the samples. Still, the final cell numbers of 23.0 to 24.5$\times 10^9$ CFU/caps met the required, declared value of 20×10^9 CFU/caps. Similarly, the number of lactobacilli in Sample 3 decreased during the shelf life but to a lower extent as compared to the other samples. The number of probiotic cells at the end of the shelf life (*i.e.* 27.5$\times 10^9$ CFU/caps) was also above the declared value, and the survival rate was 84.4 %, which is for ~11 % higher when compared to the other samples after 24 months. Furthermore, this difference was found to be statistically significant, *P* <0.001.

Thus, these results proved that the blisters packed in flow pack bags were protected significantly better from external ambient conditions as compared to blisters without this additional protective material resulting in significantly greater viability of the probiotic cells. Namely, the number of cells was significantly higher in Sample 3 as compared to Samples 1 and 2 at both time points: the 24th month and 27th month of the study (Table 1). Furthermore, after 27 months, the number of lactobacilli was below the declared number in Samples 1 and 2, whereas the number of lactobacilli cells in Sample 3 was above the declared value even after 30 months amounting to 21.2$\times 10^9$ CFU/caps. Thus, the results presented in Table 1 confirmed the influence of the novel package on the lactobacilli number decrease retardation in comparison to samples in standard packages. Sample's 3 P was <0.05 for the difference in the 27th month cells number, compared to both *P* (for Samples 1 and 2) which was <0.001 for the same study points comparison. This shows the beneficial effects of flow pack bags in lactobacilli cell protection, while the further research will be focused on evaluating these effects under conditions of potential exposure of the product to higher temperatures than the declared room temperature (for example under conditions of traveling).

Additional protection of the flow pack bags against light, moisture, and oxygen can be explained by the impermeable laminate foil that protects blisters and capsules from the exposure to light and moisture, while the inert gas within the bag further prevents penetration of oxygen to the product. Further research will focus on the individual impacts that light, moisture, and oxygen can have on the bacterial viability in the product.

4. CONCLUSION

In the age of increasing use of probiotics, a more significant commitment of manufacturers is needed to preserve the cell viability in commercially available probiotic products. Preservation of viability is a prerequisite for achieving the probiotic action of the selected strain during the shelf life and product use. In addition to optimizing the production processes, one of the crucial factors in preserving viability is the choice of packaging material for the probiotic product.

In this paper, the initial hypothesis was that for the commercial probiotic product Flobian® containing *Lactiplantibacillus plantarum* 299v probiotic strain, it is beneficial to pack the blisters containing capsules within flow pack bags to better preserve the viability of the probiotic strain during the product use.

First it was proved that the probiotic capsules packed within a PVC/PVdC/PE foil blister pack and stored at room temperature during the shelf life, at the declared storage conditions, retained the declared number of viable probiotic cells per capsule. However, the viability of lactobacilli cells was slightly but significantly higher (~11 %) after 24 months when the blisters were packed within additional flow pack bags filled with the inert gas (*i.e.* nitrogen) compared to the samples without this type of packaging material. Moreover, due to the probiotic higher viability, prolongation of the product shelf life to 30 months when stored at or below 25 °C can be considered.

Optimization of the production process and packaging conditions of probiotics is a continuous and constant challenge for the pharmaceutical industry because it involves continuous monitoring and control of process parameters and the possible introduction of modern and improved packaging materials. This research study is a contribution in this direction.

REFERENCES

[1] WGO Review Team. *World Gastroenterology Organisation Global Guidelines- Probiotics and prebiotics.* World Gastroenterology Organisation; 2017 https://www.worldgastroenterology.org/UserFiles/file/guidelines/probiotics-and-prebiotics-english-2017.pdf

[2] FAO (Food and Agriculture Organization of the United Nations), WHO (World Health Organization). *Health and nutritional properties of probiotics in food including powder milk with live lactic acid bacteria*. Cordoba, Argentina; 2001. https://www.iqb.es/digestivo/pdfs/probioticos.pdf.

[3] Salminen S, Ouwehand AC, Isolauri E. Clinical Applications of Probiotic Bacteria. *Int Dairy J*. 1998; 8(5-6): 563-572 https://doi.org/10.1016/S0958-6946(98)00077-6.

[4] Zheng J, Wittouck S, Salvetti E, et al. A taxonomic note on the genus Lactobacillus: Description of 23 novel genera, emended description of the genus Lactobacillus Beijerinck 1901, and union of Lactobacillaceae and Leuconostocaceae. *Int J Syst Evol Microbiol.* 2020; 70 (4): 2782-2858 https://doi.org/10.1099/ijsem.0.004107.

[5] Korčok D, Tršić-Milanović N, Ivanović N, Đorđević B. Development of Probiotic Formulation for the Treatment of Iron Deficiency Anemia. *Chem Pharm Bull*. 2018; 66(4): 347–352 https://doi.org/10.1248/cpb.c17-00634.

[6] Arvidsson Nordstrom E, Teixeira C, Montelius C, Jeppsson B, Larsson N. Lactiplantibacillus plantarum 299v (LP299V®): three decades of research. *Benef Microbes*. 2021; 12(5): 441-465 https://doi.org/10.3920/bm2020.0191.

[7] Abdelazez A, Abdelmotaal H, Zong-Tao Z, Fang-Fang J, Sami R, Zhang L, Rahman Al Twaha A, Meng X. Potential benefits of Lactiplantibacillus plantarum as probiotic and its advantages in human health and industrial applications. *Adv Environ Biol.* 2018; 12(1): 16-27 http://dx.doi.org/10.22587/aeb.2018.12.1.4.

[8] Axling U, Önning G, Martinsson Niskanen T, Larsson N, Hansson SR, Hulthén L. The effect of Lactiplantibacillus plantarum 299v together with low dose of iron on iron status in healthy pregnant women: A randomized clinical trial. *Acta Obstet Gynecol Scand*. 2021; 100(9): 1602–1610 https://doi.org/10.1111%2Faogs.14153.

[9] Ipek G, Juneja V, Ahmedna M. *Probiotics in food safety and human health*. 1st ed., Boca Raton, FL, USA: Taylor and Francis Group; 2006 https://doi.org/10.1201/9781420027570.

[10] Korčok D, Tršić- Milanović N, Ilić M, Mitić B, Đorđević B, Ivanović N. Improving the viability and stability of probiotic product with Saccharomyces boulardii DBVPG. *Hem Ind*. 2021; 75(1): 25-30 https://doi.org/10.2298/HEMIND201211008K.

[11] Wang G, Chen Y, Xia Y, Song X, Ai L. Characteristics of Probiotic Preparations and Their Applications. *Foods*. 2022; 11: 2472 https://doi.org/10.3390/foods11162472.

[12] Fenster K, Freeburg B, Holland C, Wong C, Rønhave Laursen R, Ouweghand AC. The Production and Delivery of Probiotics: A Review of a Practical Approach. *Microorganisms*. 2019; 7(3): 83 https://doi.org/10.3390/microorganisms7030083.

[13] Saarela M. Probiotic technology Maintaining viability and stability. *Agro Food Industry Hi Tech*. 2007; 18 (4): 19-21 https://www.researchgate.net/publication/289771526_Probiotic_technology_Maintaining_viability_and_stability.

[14] Uddin M, Mamun A, Rashid M, Asaduzzaaman M. In-process and Finished Products Quality Control Tests for Pharmaceutical Capsules According to Pharmacopoeias. *Int. J Pharm Res*. 2015; 9(2): 1-9 https://doi.org/10.9734/bjpr%2F2016%2F22044.

[15] Dao H, Lakhani P, Police A, Kallakunta V, Ajjarapu SS, Wu KW, Ponkshe P, Repka MA, Murthy SN. Microbial Stability of Pharmaceutical and Cosmetic Products. *AAPS Pharm SciTech*. 2018; 19(1): 60–78 https://doi.org/10.1208/s12249-017-0875-1.

[16] Das S, Bhattacharjee D, Manna A, Basu S, Chowdhury S, Mukherjee S, Bhattacharyya BK. Effect of Different Excipients and packaging Materials on Commercial Preparation of Probiotic Formulation. *Int J Pharm Sci Res*. 2014; 5(5): 1830-1836 http://dx.doi.org/10.13040/IJPSR.0975-8232.5(5).1830-36.

[17] Kolaček S, Hojsak I, Berni Canani R, Guarino A, Indrio F, Orel R, Pot B, Shamir R, Szajewska H, Vandenplas Y, van Goudoever J, Weizman Z, and ESPGHAN Working Group for Probiotics and Prebiotics. Commercial Probiotic Products: A Call for Improved Quality Control. A Position Paper by the ESPGHAN Working Group for Probiotics and Prebiotics. *J Pediatr Gastroenterol Nutr*. 2017; 65(1): 117–124 https://doi.org/10.1097/mpg.0000000000001603.

[18] De Man JC, Rogosa M, Elisabeth Sharpe M. A medium for the cultivation of lactobacilli. *J Appl Microbiol.* 1960; 23: 130-135 https://doi.org/10.1111/j.1365-2672.1960.tb00188.x.

[19] Tranberg A, Klarin B, Johnson J, Pahlman LI. Efficacy of *Lactiplantibacillus plantarum* 299 and 299 v against nosocomial oropharyngeal pathogens in vitro and as an oral prophylactic treatment in a randomized, controlled clinical trial. *Microbiologyopen*. 2021; 10(1): 1151 https://doi.org/10.1002/mbo3.1151.

[20] Sánchez Rodríguez M, Castán Urbano H, Muñoz de los Ríos D. Evaluation of Viability of Lactobacillus fermentum CECT 5716 in Gelatin and Gastroresistant Capsules. *J Pharm Pharmacol*. 2016; 4(8): 413-418 http://dx.doi.org/10.17265/2328-2150/2016.08.009.

Poboljšanje stabilnosti probiotskog proizvoda sa *Lactiplantibacillus plantarum* 299v uvođenjem laminatnih („flow pack") kesica

Gabor Katona[1], Davor J. Korčok[1,2], Nada A. Tršić-Milanović[2] i Nataša M. Jovanović-Lješković[1]

[1]Farmaceutski fakultet Novi Sad, Trg mladenaca 5, Novi Sad, Srbija
[2]Abela Pharm d.o.o., Viline vode bb, Beograd, Srbija

(Stručni rad)

Izvod

U svakodnevnoj upotrebi širom sveta sve su zastupljeniji probiotski proizvodi. Paraleno s tim, i u stručnoj javnosti raste interesovanje za istraživanja njihove proizvodnje i primene. Stabilnost probiotskog proizvoda se u farmaceutskoj proizvodnji obezbeđuje izborom probiotskog soja, formulacije i izborom pakovanja. Pakovanje je završna faza proizvodnje i presudni je faktor za stabilnost probiotika radi održanja vijabilnosti u toku roka upotrebe. U ovom radu opisan je izbor dodatnog pakovanja kapsuliranog probiotika *Lactiplantibacillus plantarum* 299v. Ispitivan je efekat dodatne zaštite blistera u laminatnim kesicama (engl. *flow pack bag*). Odabrani su blisteri napravljeni od PVC/PVdC/PE (polivinil hlorid/poliviniliden hlorid/polietilen) folije i aluminijumske folije, koji su zatim paraleno ispitani u poređenju sa blisterima pakovanim u dodatne kesice punjene inertnim gasom. Poređenjem vijabilnosti probiotskih ćelija laktobacila u uzorcima blistera u kesicama u odnosu na dva uzorka blistera bez tih kesica uočena je bolja zaštita probotskih ćelija od kiseonika, svetlosti i vlage u dodatnom pakovanju. Uvođenjem dodatne zaštite blistera u kesicama dobijena je za 11 % veća vijabilnost probiotika u poređenju sa uzorcima bez kesica posle 24 meseci što omogućava komformnije čuvanje proizvoda tokom upotrebe.

Utilization of solidified industrial hazardous waste in construction: A case study

Radmila M. Šerović[1], Ivana V. Jelić[2], Branislava I. Matić[3] and Aleksandar R. Savić[4]

[1]*Ministry of Environmental Protection of the Republic of Serbia, Belgrade, Serbia*
[2]*University of Belgrade, Vinča Institute of Nuclear Sciences, Belgrade, Serbia*
[3]*Institute of Public Health of Serbia „Dr. Milan Jovanović Batut", Belgrade, Serbia*
[4]*University of Belgrade, Faculty of Civil Engineering, Belgrade, Serbia*

Abstract

Utilization possibilities of solidified fractions of industrial hazardous waste obtained by mixing with inert materials in construction were investigated. Waste mineral oils, water-hydrocarbon emulsions mixture, and waste filter cakes from the physico-chemical treatment of wastewater generated by washing of patterned rollers for a printing machine, were used as models of industrial hazardous waste in the solidification process. Investigation comprised preparation of concrete and asphalt mixtures for further testing. The solidified powder was analyzed regarding the granulometric composition, while the obtained concrete samples were further subjected to compressive strength determination, whereas the asphalt mixtures were tested in the context of potential waterproofing materials. According to the obtained leaching test results, all the samples met the required conditions for further application. Compressive strength test results were in the range of 8.7 – 22.6 MPa. Still, the measured compressive strength values were lower than expected, which is explained using solidified powder fractions of smaller grain size. According to the results, it can be concluded that the investigated mixtures cannot be used for structural building elements, but their usage is recommended for elements such as pavements, roadside, path cubes, concrete haberdashery, *etc.* Asphalt mixtures showed acceptable properties in terms of mechanical, durability, and waterproofing tests.

Keywords: inertization; solidification; recycling; concrete; asphalt.

Available on-line at the Journal web address: http://www.ache.org.rs/HI/

1. INTRODUCTION

Accelerated industrial development accompanied by population growth has resulted in environmental degradation, mainly caused by the production of an increasing amount of waste with inevitable detrimental effects on human health [1]. From the Industrial Revolution to the present, the so-called "linear industrial waste management system" has been developed and utilized, which assumes that resources are abundant, accessible, and can be easily used and disposed of cheaply [2]. Today, the European Union (EU) waste management act is based on the "waste management hierarchy" principle. This act prioritizes waste management policies, as well as priorities in waste management at the operational level: prevention, preparation for reuse, recycling, reuse, and, as the least desirable option, waste disposal, *i.e.*, disposal and burning of waste without the use of energy [3,[2]. Over the last few years, waste recycling in the EU has been stimulated by appropriate regulations, while the EU legislation provides a tremendous boost to national governments in their efforts to improve recycling systems [4].

Approximately 3 billion t of all kinds of waste are generated annually worldwide [5]. The manufacturing sector (industry) generates approximately 360 Mt of waste annually, the construction sector produces 900 Mt of waste, while the water supply and energy generation sectors produce 95 Mt of waste annually [5]. Among the waste generated in the EU in 2020, 4.4 % of the total was classified as hazardous waste. Compared with 2010, another 5.1 % more hazardous waste was generated in 2020 in the EU, which is an increase in quantity from 90.8 to 95.5 Mt, with a peak in 2018 of 101.7 Mt [6]. The decline in 2020 as compared to 2018 is a result mainly due to the lower amount of combustion waste due to the lower

usage of solid fuels such as coal, coke, and oil shale. In 2020, the share of hazardous waste in total waste generation was between 0.5 % in Romania and 12.0 % in Bulgaria. Among the non-EU member countries, Turkey recorded the highest share of hazardous waste in total waste generation (28.5 %) and was followed by North Macedonia (28.2 %), Montenegro (27.6 %), Serbia (19.3 %) and Norway (13.3 %) [6]. In 2020, a total of 9.57 Mt of waste was generated in the Republic of Serbia (RS), of which approximately 68,000 t was hazardous waste [6-8].

Hazardous waste sources include industry, thermal power plants, mining, mineral processing sites, agricultural facilities, research laboratories, and the natural environment. Hazardous waste can be in the form of solids, liquids, sludge, gases, or aerosols, and it is generated primarily by chemical production, manufacturing, and other industrial activities. It may cause damage during inadequate storage, transportation, treatment, or disposal operations. Thermal energy facilities are the largest producers of waste. Ash, slag, and dust from the boiler and fly ash from coal combustion were generated in the amount of 7.78 Mt, *i.e.* 81% of the total waste produced in RS in 2020 [9]. Other types of waste originating from thermal processes are also present in significant quantities: unprocessed slag, waste from slag processing, and solid waste based on calcium, generated in the process of desulphurizing gases. Currently, fly ash is handed over for the needs of cement production. Certain quantities of gypsum from the desulphurization process are exported, which has the status of a by-product [4]. Thermal power facilities are also the major waste producers in the RS. In contrast, in hazardous waste stream production, sludge and scone filters from the process of gas treatment containing hazardous substances, dominate in quantity (in the amount of 10,800 t), followed by excavations of land during construction activities, solidified and other waste from waste treatment plants, waste packaging, and waste from metal processing [9-12].

In line with the waste management hierarchy, which highlights the reuse and recycling of waste, in particular, both in the EU and the RS, research is still being carried out regarding the reuse of waste in the process of making construction products containing certain amounts of waste. This research pursues the line of reusing the waste in creation of certain types of concrete products or asphalt, containing waste components [13-16]. Reusing waste contributes to preservation of natural resources, production profitability, and the development of recyclingmarket, through the placement of new products intended for the construction industry, possibly exhibiting better shaping abilities and better properties in terms of mass reduction, water-impermeability, hydro-thermal and acoustic insulation, fire resistance, *etc.* [17]. Moreover, the so-called supplementary cementitious materials reduce the amount of spent Portland cement in mortar and concrete, thus reducing the greenhouse effect [18]. In addition to the C–H structure, many types of hydrocarbon-based industrial waste materials usually contain elements such as oxygen, nitrogen, sulfur, phosphorus, chlorine, and heavy metals. Due to the presence of these elements, this waste is classified as hazardous waste material and has to be solidified to obtain inert dry hydrophobic powder for further use.

This research examined the possibility of further use of inertized or solidified industrial hazardous waste as fillers or fine aggregates in construction and road sub-base materials, *i.e.*, in concrete and asphalt mixtures that would be competitive in the market, as they are made of recycled materials. According to the authors' knowledge based on literature, there is scarce literature data concerning the utilization of solidificates in the concrete and asphalt mixtures [15]. However, previous investigations were based mainly on the use of concrete products made from construction waste, *i.e.* recycled aggregates [18].

The hazardous waste inertization, *i.e.* reducing its hazardous characteristics, includes fraction solidification (congestion and hardening) and waste stabilization [19-20]. Through this process, waste is physically bound or thickened into monolithic solid mass of high structural integrity. At the same time, stabilization is a process used to reduce the hazardous potential of waste by turning pollutants into the least melting, least immobile, or least toxic form [20]. The C–H waste solidification method is one of the most used techniques available to ultimately care for waste in an environmentally acceptable and safe manner, in line with the rules of the chemical and technological trade.

Solidification/stabilization is accepted as a well-established disposal technique for hazardous waste. In hazardous waste management, solidification/stabilization is a term typically used to designate a technology employing additives to alter hazardous waste and make it non-hazardous or acceptable for current land disposal requirements.

2. EXPERIMENTAL

Two types of industrial hazardous waste were utilized:

1. A mixture of waste oils and oil emulsions after the filtration process, index number 120107*/120109*/190207*, the Catalog of waste [10], which represent the products of the oil emulsion purification process from the ultrafiltration plant at the Holding company "FAM-DMB", ltd., Car engine factory "21. May", in Rakovica, Belgrade, Serbia.
2. Waste generated by washing in the UV machine in the PVC plant and waste filter cakes from the physical and chemical treatment of wastewater generated by washing the patterned rollers for a printing machine of the PVC plant, index number 190813*/190206, the Catalog of waste [10], from the company "Tarkett" ltd., BačkaPalanka, Serbia.

The reaction mixture for the solidification process consisted of a maximum of 20 wt.% organic phase composed of a mixture of waste oils and oil emulsions and 40 wt% of dry matter from the waste filter cake from the physico-chemical treatment of wastewater (created by washing patterned rollers for a printing machine in the PVC plant), called together as C–H-waste and 40 wt.% water, which is one of the basic components for ongoing exothermic reactions.

The waste inertization process (reducing the hazardous characteristics of hazardous waste) included solidification (thickening) and waste stabilization. In the process of solidification, a chemical reaction occurs and the formation of a stable, organo-Ca (Ca–C–H) lattice into which various ligands from the C–H-waste material are permanently incorporated/bonded. The product of the reaction is a qualitatively new inert, *i.e.* stabilized material in solid form, which, according to its chemical composition, is a mixture of organo-Ca hydrophobic (water-insoluble) salts, *i.e.* solidificate.

2. 1. Solidification of industrial hazardous waste

Inertization accompanied by solidification, which impliescomplex physico-chemical and thermal dissociation process with vacuum encapsulation and primary solidification of waste material, were performed in a specially built (patented) Reactor R-210/L-210/211 (Peters, Austria) by the MID-MIX® patented technology. The reaction proceeds according to overall stoichiometric equation (1) with an energy output of Q = 3,776 MJ [20]:

$$8,976 \text{ kg CHW} + 1,024 \text{ kg } H_2O + 3,200 \text{ kg CaO} = 12,176 \text{ kg S} \tag{1}$$
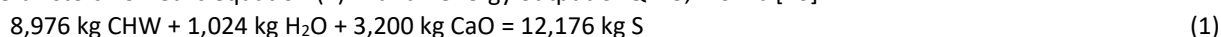
where CHW and S denote C–H-waste and solidificate, respectively.

For the purposes of the further investigation, 150 kg of solidificate was prepared.

The process was semi-continuous with the retention time of materials in the reactor of about 5 min, under steering. The reactor's frequency regulator adjusts the number of revolutions in the reactor. Solidified fraction arises as a result of a physico-chemical reaction in which waste containing mixtures of different hydrocarbons (*i.e.*, C–H bonds), with existing or added water molecules, reacts with dissociated elements created by the exothermal reaction with calcium oxide, which in the presence of water creates conditions for the formation of a mixed Ca–C–H-crystal lattice, also creating the calcium hydroxide and releasing heat of about 1.18 MJ kg^{-1} of calcium oxide [20]. The released heat is distributed to C–H bonds, hence the destruction of hydrocarbons, which results in the production of carbon dioxide and water, taking place at a temperature of around 100°C [20]. The total amount of released energy per kilogram of calcium oxide is sufficient to break the bonds in the benzene ring, *i.e.* the C–H structure, to evaporate almost all physically present water and achieve conditions for complete solidification of the entire mixture in the reactor. Further, released carbon dioxide can react with the calcium hydroxide and/or calcium oxide creating calcium carbonate, which remains in the solidification mixture. The temperature of the furthermost reacted solidified fraction is constantly above 100 °C, usually around 120 °C, while its cooling is very slow (about 45°C/24 h) [20].

In the process of solidification according to the MID-MIX® technology, with the mode of operation precisely selected according to the type and characteristics of waste being processed, the input waste is transformed into a whole new form of material, because each particle of waste material, helped by water vapor molecules, is encapsulated into a highly stable organo-Ca lattice and, under balanced conditions, is converted into inert stable powder, *i.e.*, solidificate. Solidificate is loose powder and if there is a balanced amount of hydrocarbon waste in the treatment, solidified powder has highly hydrophobic properties.

2. 2. Preparation of concrete and asphalt mixtures

Prior to mixture preparation, the granulometric composition of solidified powder was determined according to the ISO 3310-1:2016 standard [21], at the Vibratory Sieve Shaker AS 200 (Retsch, Germany).

The obtained solidified powder was mixed in different mass ratios with other inert materials (aggregates – river aggregate in fine 0/4 mm and 4/16 mm coarse fraction (Dunavac, Serbia), limestone powder (Granit Peščar, Serbia), water, cement PC 35 M(V-L) 42,5R (Lafarge, Serbia) and bitumenEuro 70/100 (NIS, Serbia) to obtain concrete and asphalt mixtures. The composition ratios of prepared concrete mixtures are shown in Table 1.

Table 1. Composition of concrete mixtures

Sample	Content, wt. %					
	Solidified powder fraction	Aggregate, fine fraction 0/4 mm	Aggregate, coarse fraction 4/16 mm	Cement	Limestone powder	Water
Bet-1	4	31.2	20.8	40	2.6	1.4
Bet-2	6	28.8	19.2	40	2.4	3.6
Bet-3	9	27.0	18.0	38	2.2	5.8
Bet-4	13	25.2	16.8	37	2.1	5.9
Bet-5	20	22.8	15.2	33	1.9	7.1
Bet-6	27	21.6	14.4	28	1.8	7.2
Bet-7	35	19.8	13.2	22	1.6	8.4
Bet-8	42	18.0	12.0	18	1.5	8.5
Bet-9	45	15.6	10.4	17	1.3	10.7
Bet-10	50	13.8	9.2	15	1.2	10.8

In addition, possibilities of solidificate application in asphalt mixtures were examined by partially supplementing a fine fraction of aggregates (river aggregate 0/4 mm, Dunavac,Serbia) with solidified powder in asphalt mixtures (Table 2).

Table 2. Composition of asphalt mixtures

	Content, wt.%		
	Asf-1	Asf-2	Asf-3
Solidified powder fraction	25	20	15
Aggregate, fine fraction0/4 mm	33	38	43
Aggregate, coarse fraction4/16 mm	20	20	20
Bitumen	22	22	22

2. 3. Sample preparation

The third phase of the research involved preparation of concrete samples for compressive strength determination and asphalt samples for the impact test (500 g weight impact from the height of 300 mm), cold stability (flexural test at -20 °C), water-tightness (5 bar water pressure for 1 h) and behavior in water [22].

Fresh concrete mixtures were cast into a 100 mm cubic-shaped mold according to the standard SRPS EN 12390-1:2021 [23]. Samples were made following the standard SRPS EN 12390-2:2019 [24]. Samples in the molds were dried in the air at room temperature of 20±2 °C, at a relative humidity of at least 90 %, for 24h, then arranged at a grid, 1 cm apart in water at a temperature of 20±2 °C. The water level in the container was always at least 2 cm above the sample in the mold. The compressive strength tests were performed after sample air drying for 28 days according to the standard SRPS EN 12390-3:2010 [25] by automated hydraulic press Cyber-plus Evolution (Matest, Italy). The tests were performed in duplicate, and the results are shown as mean values. The concrete cubic samples are shown in Figure 1.

Figure 1. Concrete samples made of mixtures with solidified powder

2. 4. Mixture characterization

Homogenized concrete samples and hardened asphalt mixtures were further subjected to leaching tests to assess potential impacts on the environment and toxicity characteristics.

The leaching procedure (LP) was performed according to the standard SRPS EN 12457-2 [26] for waste characterization by compliance test for leaching of granular waste materials and sludge. This is a standard mobility method for evaluating organic and inorganic substances present in liquid, solid, or multi-phase waste. The results of this test indicate a long-term leaching effect, *i.e.,* potential environmental hazard. Standards prescribe one-stage batch test at the liquid/solid ratio of 10 dm^3 kg^{-1} (10:1) for materials with high contents of solids and particle size of <4 mm (with or without decreasing particle size) [26][25]. Concrete samples and hardened asphalt mixtures were crushed by a Jaw Crusher BB 300 Mangan (Retsch, Germany), milled by a Planetary Ball Mill PBM 1-4 (Wibrotechnik, Russia) and sieved to a fraction with particle size under 4 mm by a Test Sieve (Retsch, Germany). The investigated samples were brought into contact with the distilled water during continuous stirring on the Orbital Shaker LBX ORB-PRO (Labbox, Spain) at 10 rpm at room temperature (20±2°C), with 24 h contact time, without pH control. After filtration, Pb, Cd, As, Cr, and Ni concentrations were determined by induction coupled plasma mass spectrometry at ICP-MS 7700 (Agilent, USA), according to the ISO 11885:2007 standard [27]. Tests were performed in duplicates and results were compared with the limits in the Regulation on categories, testing, and classification of waste Annex 10 [10].

After LP, liquid-liquid extraction was performed to completely dissolve possibly present organic phase. The toxicity characteristic of mixtures was estimated by the toxicity characteristic leaching procedure (TCLP) according to the standard US EPA 1311 [28]. The solid material is extracted for 18 hours with a slightly acidic fluid equal to 20 times its weight under following conditions: stirring on the Orbital ShakerLBX ORB-PRO (Labbox, Spain) at 30 rpm at room temperature (20±2°C). The possible organic phase was extracted with 20 ml diethyl ether from 100 ml TCLP liquid (extract), under defined conditions: continuous stirring on the same orbital shakerat 30 rpm and also at room temperature (20±2°C), with contact time of 18 h. The solution was evaporated to a dry residue and total hydrocarbons were determined by gas chromatography using a Gas Chromatograph 5890 Series II with Flame Ionization Detector (Hewlett Packard, USA).

3. RESULTS AND DISCUSSION

Granulometric composition of the solidified powder is presented in Figure 2.
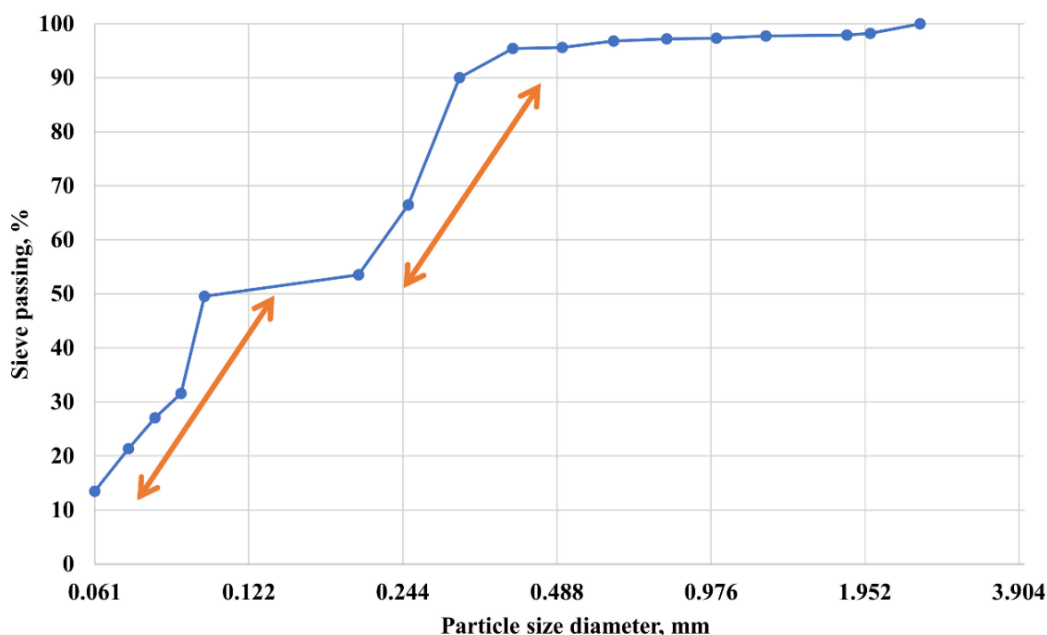
Figure 2. Granulometric composition of solidified powder fractions

As shown, if minor generalizations are applied, this composition can be considered discontinuous. Namely, particles of the fractions 0.061/0.100 mm and 0.200/0.400 mm dominantly contribute to the solidificate with 50% and 40%, respectively. Given that continuous curves are often used for producing concrete of a better quality[21][22].

The results of the compressive strength of concrete samples are shown in Table 3. along with the compressive strength of some tested materials obtained from industrial waste.

Table 3.Compressive strength results along with literature data on concrete materials supplemented with different industrial wastes (standard deviations are given in brackets)

Sample	Compressive strength, MPa
Bet-1	22.6 (0.8)
Bet-2	22.0 (0.9)
Bet-3	21.1 (0.9)
Bet-4	19.9 (0.7)
Bet-5	17.8 (0.8)
Bet-6	15.7 (0.7)
Bet-7	13.2 (0.6)
Bet-8	11.1 (0.6)
Bet-9	10.2 (0.7)
Bet-10	8.7 (0.6)
Concrete with fly ash [14]	4.5 – 17.5
Concrete with alum sludge (treated in a furnace at 200 °C) [29]	24.0 – 48.0
Concrete with Lime Stone [29]	33.0 – 53.0
Concrete with quarry dust [29]	36.0 – 65.0
Concrete with solidified wastewater treatment sludge [30]	3.9 – 5.8

The compressive strength results were in the interval of 8.7 – 22.6 MPa. Measured values were lower than expected, as explained by the presence of finer granulation in solidified powder (95.45 % of particle size <0.4 mm). Also, considering that continuous powder compositions are more favorable for better cement composites, some of the reasons for the poor behavior of the experimental mixtures can be found in the fact that the solidificate had discontinued powder composition. If a fraction of coarser granulation is used to create the sample, it is expected to gain higher compressive strength values. In particular, concrete samples that contained lower mass percentages of solidificate showed a higher strength. Therefore, samples of Bet-1, Bet-2, and Bet-3 showed satisfactory compressive strength values of over 20 MPa, bearing in mind that the typical compressive strength of Portland cement concrete varies between 20 – 40 MPa [31]. In addition, compressive strength values were still higher than in the case of some other concrete mixtures based on industrial waste (*e.g.* fly ash [14] and solidified wastewater treatment sludge [30]).

When using the MID-MIX® technology, it was experimentally confirmed that solidificates are very difficult to combine in mixtures with higher water contents, because they tend to float on the sample surface due to hydrophobicity [20]. It is also important to note that when adding solidificate to concrete or asphalt mixture, empirically determined ingredients of solidificate mixture should be used to achieve the required properties of the newly acquired material [20].

After analyzing the compressive strength results, it can be noted that solidificates in the concrete samples reduce the firmness of concrete and cannot be used in construction elements. However, utilization in some other construction elements such as pavements, roadside, path cubes, concrete haberdashery, *etc.*, could be recommended. In addition to solving the problem of disposal of one part of the total quantity of waste, the usage of industrial hazardous waste in this type of building element would undoubtedly reduce the amount of non-renewable natural raw materials used in the production, while making the production process more economically acceptable.

The experimental asphalt mixtures showed negligible differences in the tests. Namely, all mixtures stayed stable without fractures under the weight impact, without cracks during the flexural test at -20 °C, and all mixtures were water-tight (after 1 h of 5 bar water pressure), while finally, these properties did not change after one week in the water [22].

The obtained results were difficult to compare with any other research due to the lack of data regarding utilization of solidificates from industrial hazardous waste in asphalt mixtures, *i.e.*, waste mineral oils and hydrocarbon-based

emulsions [15,31-32]. In this regard, standardized data are lacking on the types of concrete elements containing organic types of industrial hazardous waste, and further research is needed.

The results of the LP test, implying the impact of investigated concrete and asphalt mixtures on the environment, are shown in Table 4.

Table 4. Results of LP tests expressed as heavy metal contents in leachate of samples of stabilized solidified powder in distilled water at the liquid/solid ratio of 10 dm³ kg⁻¹(standard deviations are given in the brackets)

Concrete and asphalt materials	c (SD) / µg dm⁻³				
	Pb	Cd	As	Cr	Ni
Bet-1	53.21 (1.10)	60.04 (1.26)	2.51 (0.06)	15.64 (0.09)	50.65 (1.20)
Bet-2	56.37 (0.64)	101.20 (1.49)	3.19 (0.03)	17.57 (0.06)	53.81 (0.81)
Bet-3	59.53 (0.75)	142.36 (1.71)	3.87 (0.04)	19.50 (0.07)	56.97 (0.98)
Bet-4	62.69 (0.95)	183.52 (0.61)	4.55 (0.03)	21.43 (0.09)	60.13 (1.00)
Bet-5	65.85 (0.98)	224.68 (2.38)	5.23 (0.03)	23.36 (0.06)	63.29 (0.96)
Bet-6	76.05 (1.19)	370.00 (2.97)	5.35 (0.04)	24.93 (0.04)	78.16 (0.92)
Bet-7	79.21 (0.93)	381.16 (1.84)	5.63 (0.03)	26.86 (0.04)	83.32 (1.00)
Bet-8	82.37 (1.34)	392.32 (2.97)	5.91 (0.05)	28.79 (0.03)	88.48 (1.00)
Bet-9	85.53 (1.58)	403.48 (3.25)	6.19 (0.04)	30.72 (0.09)	93.64 (1.02)
Bet-10	119.30 (1.89)	414.64 (2.97)	6.47 (0.03)	32.65 (0.03)	98.80 (1.08)
Asf-1	43.68 (0.91)	50.06 (1.10)	1.35 (0.03)	11.22 (0.03)	46.32 (0.99)
Asf-2	40.03 (0.79)	43.55 (0.58)	1.17 (0.02)	9.76 (0.03)	40.30 (0.92)
Asf-3	36.38 (0.54)	37.89 (0.71)	1.02 (0.02)	8.49 (0.02)	35.06 (0.88)
Reference value [10]	5000	1000	5000	5000	20000

The results of LP tests were under the prescribed values [28]. The TCLP results showed that total hydrocarbons were not detected in the tested samples, and therefore these materials do not show any toxicity characteristics. According to the obtained results, all samples meet the conditions for further applications [28].

4. CONCLUSION

In this work possibilities for further use of inertized, *i.e.*, solidified industrial hazardous waste were investigated with the focus on production of new building products that would be competitive on the market due to their origin from recycled materials. The inertization of hazardous waste, *i.e.*, reducing its hazardous characteristics, involves solidifycation and stabilization of waste. The method of waste solidification is one of the most used techniques available for the final care of waste in an environmentally acceptable and safe manner, following the rules of the chemical and techno-logical trade.

The experimental part had four phases. In the first part of the research, solidification/inertization of collected samples of industrial hazardous waste was carried out: waste mineral oils and a mixture of water-hydrocarbon emulsion, as well as waste filter scones from the physical and chemical treatment of wastewater caused by washing the patterned rollers for a printing machine. Waste fractions were solidified resulting in powder that was examined regarding granulometric composition. In the next phase, the solidified powder was mixed with the necessary ingredients to make concrete and asphalt mixtures. The concrete samples were tested on compressive strength and asphalt samples on waterproofing properties. The impact of waste-based samples on the environment and their potential toxicity were carried out by the standard leaching tests: leaching procedure (LP) and the toxicity characteristic leaching procedure (TCLP).

The compressive strength results were in the interval of 8.7 to 22.6 MPa, which was lower than expected, and explained by small granulation in the solidified powder (95.45 % of particle size <0.4 mm). The granulometric composition can be considered discontinuous, which is a disadvantage in obtaining high-quality concrete. Samples with lower contents of the solidified powder (*i.e.* Bet-1, Bet-2, and Bet-3) showed satisfactory compressive strength values of over 20 MPa, bearing in mind that the typical compressive strength of Portland cement concrete varies between 20 to 40 MPa. Thus, the obtained results indicate that addition of solidificates to the concrete reduces the concrete strength, so that it cannot be exploited in structural building elements, but it is recommended for pavements, roadside, path cubes, concrete haberdashery, and similar. All of the asphalt mixtures had similar properties regarding the

conducted tests (the impact test, cold stability, water-tightness, and water soaking), implying that the inertized hazardous waste does not induce adverse effects on asphalt mixtures.

The results of the LP were under the prescribed values, and the TCLP results showed that total hydrocarbons were not detectable. Hence, these kinds of recycled mixtures do not represent environmental hazard and do not show toxicity characteristics.

The obtained results indicate significant potentials of the applied procedure and waste materials for further use, but additional investigations are necessary since there is a major lack of literature data and research regarding the utilization of inertized industrial hazardous waste in concrete and asphalt mixtures.

REFERENCES

[1]   United Nations Environment Programme 2005; Solid Waste Management Volume 1. ISBN: 92-807-2676-5. https://wedocs.unep.org/20.500.11822/30733

[2]   Scheel C., Bello B. Transforming Linear Production Chains into Circular Value Extended Systems. *Sustainability* 2022; 14: 3726. https://doi.org/10.3390/su14073726

[3]   Directive 2008/98/EC of the European Parliament and of the Council of 19 November 2008 on waste and repealing certain Directives, OJL 312, 22. 11. 2008, p. 3-30. https://eur-lex.europa.eu/legal-content/EN/TXT/?uri=celex%3A32008L0098

[4]   European Commission. Communication from the Commission to the European Parliament, the Council, the European Economic and Social Committee and the Committee of Regions, *A new Circular Economy Action Plan For a cleaner and more competitive Europe*, EU 2020.https://eur-lex.europa.eu/legal-content/EN/TXT/?uri=CELEX:52020DC0098

[5]   EEA, 2015, The European environment–state and outlook 2015: synthesis report, European Environment Agency, Copenhagen.Luxembourg: Publications Office of the European Union, 2015. ISBN 978-92-9213-515-7. https://doi.org/10.2800/944899

[6]   Waste statistics, Eurostat. https://ec.europa.eu/eurostat/statistics-explained/index.php?title=Waste_statistics#Total_waste_generation%20]

[7]   Waste Management in the Republic of Serbia for the period 2011–2020, 2021; Serbian Environmental Protection Agency (SEPA). http://www.sepa.gov.rs/download/UpravljanjeOtpadomRS_2011_2020.pdf (in Serbian)

[8]   State of the Environment Report 2020, Serbian Environmental Protection Agency (SEPA), 2021. http://www.sepa.gov.rs/download/Report_2020.pdf (in Serbian)

[9]   Waste management program of the Republic of Serbia for the period 2022–2031. Official Gazette of the RS, No. 30/18. https://www.ekologija.gov.rs/sites/default/files/2022-02/program_upravljanja_otpadom_u_rs_za_period_2022-2031._god_0_2.pdf (in Serbian)

[10]   Regulation on categories, testing, and classification of waste. Official Gazette of the RS, No.56/10, 2010. https://www.paragraf.rs/propisi/pravilnik-kategorijama-ispitivanju-klasifikaciji-otpada.html (in Serbian)

[11]   Products becoming special waste flows after utilization in the Republic of Serbia in 2020; Serbian Environmental Protection Agency (SEPA), Belgrade, June 2021. http://www.sepa.gov.rs/download/PTO20.pdf

[12]   Životić M, Stojiljković D, Jovović A, Čudić V, The possibility of using ash and slag from the landfill of the "Nikola Tesla" thermal power plant as waste with usable value, *Hem Ind.* 2012; 66(3): 403-412. https://doi.org/10.2298/HEMIND110905095Z

[13]   MIlošević N, Jelić I, Serović R, Amounts of hazardous industrial and commercial waste in Serbia. In: Proceedings of *Conference Wastewater, municipal solid waste and hazardous waste,* Serbia (2018), pp. 218-222. ISBN 978-86-82931-83-6 (in Serbian)

[14]   Terzić A, PavlovićLj, MiličićLj, Evaluation of Lignite Fly Ash for Utilization as Component in Construction Materials, *Int J Coal Prep Util.* 2013; 33 (4): 159-180. https://doi.org/10.1080/19392699.2013.776960

[15]   Šerović R., Jelić I., Pavićević V., Use of solidification of industrial waste in construction industry. In*: Proceedings of International conference wastewater, municipal solid waste and hazardous waste*, Serbia, 2017, pp. 196-200. ISBN 978-86-82931-83-6 (in Serbian)

[16]   Jevtić D., Zakić D., Savić A., Investigation of cement-based composites made with recycled rubber aggregate, *Hem Ind.* 2012; 66 (4): 609-617. https://doi.org/10.2298/HEMIND111203010J

[17] Chen J., Li X., Huang K., Eckelman M., Chertow M., Jiang D., Non-hazardous industrial waste in the United States: 100 Million tonnes of recoverable resources, *Resour Conserv Recycl.* 2021; 167: 105369. https://doi.org/10.1016/j.resconrec.2020.105369

[18] Jevtić D, Zakić D, Savić A, Specifičnosti tehnologije spravljanja betona na bazi recikliranog agregata, *Materijali i konstrukcije* 2009; 52(1): 52-62. https://scindeks-clanci.ceon.rs/data/pdf/0543-0798/2009/0543-07980901052J.pdf (in Serbian)

[19] Dabić P, BarbirD.Implementation of natural and artificial materials in Portland cement. *Hem Ind.* 2020; 74, 3: 147-161. https://doi.org/10.2298/HEMIND191216014D

[20] Spanovic M, Process and plant for preparation and treating of communal and industrial wastes into usable products, Patent No. EP1109633B1, European Patent Office, 2005. https://patents.google.com/patent/EP1109633B1/en

[21] ISO 3310-1:2016, Test sieves – Technical requirements and testing – Part 1: Test sieves of metal wire cloth. https://www.iso.org/standard/62410.html

[22] Muravljov M. Construction materials, The Construction book, Belgrade, Serbia, 1995. (in Serbian). https://www.scribd.com/document/391283579/Mihailo-Muravljov-Gradjevinski-Materijali

[23] SRPS EN 12390-1:2021, Testing hardened concrete - Part 1: Shape, dimensions and other requirements for specimens and moulds.https://iss.rs/en/project/show/iss:proj:71095

[24] SRPS EN 12390-2:2019, Testing hardened concrete - Part 2: Making and curing specimens for strength tests. https://iss.rs/en/project/show/iss:proj:62271

[25] SRPS EN 12390-3:2010, Testing hardened concrete – Part 3: Compressive strength of test specimen. https://iss.rs/en/project/show/iss:proj:62276

[26] SRPS EN 12457-2:2008, Characterization of waste – Leaching – Compliance test for leaching of granular waste materials and sludges – Part 2: One stage batch test at a liquid-solid ratio of 10 l/kg for materials with a high content solids and particle size of less than 4 mm (with decreasing particle size, or without decreasing). https://iss.rs/sr_Cyrl/project/show/iss:proj:20734

[27] ISO 11885:2007, Water quality – Determination of selected elements by inductively coupled plasma optical emission spectrometry (ICP-OES). https://www.iso.org/standard/36250.html

[28] Environmental Protection Agency USA, US EPA, Method 1311: Toxicity Characteristic Leaching Procedure, Environmental Protection Agency, Washington, D.C., USA 1992.https://www.epa.gov/sites/default/files/2015-12/documents/1311.pdf

[29] Odimegwu TC, Kaish ABMA, Zakaria I, Abood MM, Jamil M, Ngozi KO, Nondestructive Determination of Strength of Concrete Incorporating Industrial Wastes as Partial Replacement for Fine Aggregate, *Sensors*. 2021, 21: 8256. https://doi.org/10.3390/s21248256

[30] Govedarica O, Aškrabić M, Hadnadev-Kostić M., Vulić T, Lekić B, Rajaković-Ognjanović V, Zakić D. Evaluation of Solidified Wastewater Treatment Sludge as a Potential SCM in Pervious Concrete Pavements. *Materials* 2022; 15: 4919. https://doi.org/10.3390/ma15144919

[31] Piro N, Salih A, Hamad S, Kurda R, Comprehensive multiscale techniques to estimate the compressive strength of concrete incorporated with carbon nanotubes at various curing times and mix proportions, *J Mater Res Technol.* 2021; 15: 6506-6527.https://doi.org/10.1016/j.jmrt.2021.11.028

[32] Brkljač N, Šević D, Beker I, Kesić I, Milisavljević S. Procedure for treatment of hazardous waste by MID-MIX procedure in Serbia, *Int J Phys Sci. 2*012; 7 (18): 2639-2646.https://doi.org/10.5897/IJPS12.139

Upotreba solidifikovanih frakcija industrijskog opasnog otpada u niskogradnji: Studija slučaja u Republici Srbiji

Radmila M. Šerović[1], Ivana V. Jelić[2], Branislava I. Matić[3] i Aleksandar R. Savić[4]

[1]*Ministarstvo zaštite životne sredine Republike Srbije, Beograd, Srbija*
[2]*Univerzitet u Beogradu, Institut za nuklearne nauke „Vinča", Beograd, Srbija*
[3]*Institut za javno zdravlje Srbije „Dr Milan Jovanović Batut", Beograd, Srbija*
[4]*Univerzitet u Beogradu, Građevinski fakultet, Beograd, Srbija*

(Stručni rad)

Izvod

Ispitivane su mogućnosti korišćenja solidifikovanih frakcija industrijskog opasnog otpada dobijenog njegovim mešanjem sa inertnim materijalima u građevinarstvu. Kao predstavnici industrijskog opasnog otpada u procesu solidifikacije korišćena su otpadna mineralna ulja, mešavina vodeno-ugljovodonične emulzije i otpadne filter pogačeiz fizičko-hemijskog tretmana otpadnih voda nastalih pranjem dezen valjaka na mašini za štampanje. Istraživanje je podrazumevalo pripremu betona i asfaltne mešavine za dalja ispitivanja. Utvrđen je granulometrijski sastav solidifikovanog praha, uzorci betona su dalje podvrgnuti određivanju čvrstoće na pritisak, a asfaltne mešavine su ispitivane u kontekstu hidroizolacionih materijala. Prema dobijenim rezultatima ispitivanja luženja, svi uzorci su ispunjavali potrebne uslove za dalju primenu. Rezultati ispitivanja čvrstoće na pritisak bili su u opsegu od 8,7 – 22,6 MPa. Izmerene vrednosti čvrstoće na pritisak bile su niže od očekivanih, što se objašnjava upotrebom solidifikovanih frakcija manje granulacije. Na osnovu dobijenih rezultata može se zaključiti da se ispitivane mešavine ne mogu koristiti za konstruktivne građevinske elemente, te se preporučuje njihova upotreba za građevinske elemente kao što su trotoari, ivičnjaci, kocke za staze, betonska galanterija i dr. Asfaltne mešavine su pokazale prihvatljiva svojstva u pogledu mehaničkih, ispitivanja izdržljivosti i hidroizolacije.

Improvement of energy properties of lignocellulosic waste by thermochemical conversion into biochar

Zorica Lopičić[1], Anja Antanasković[1], Tatjana Šoštarić[1], Vladimir Adamović[1], Marina Orlić[1], Jelena Milojković[1] and Milan Milivojević[2]

[1]*Institute for Technology of Nuclear and Other Mineral Raw Materials, Bulevar Franše d'Eperea 86, 11000 Belgrade, Serbia*
[2]*University of Belgrade, Faculty of Technology and Metallurgy, Karnegijeva 4, 11120 Belgrade, Serbia*

Abstract

Peach stones, a valuable agro-industrial by-product available in many countries worldwide, comprise a renewable resource, which can be widely applied for multifunctional purposes. Its important advantages such as high-energy value, low ash content, low price and wide abundance, make peach stones an ideal fuel for energy production, but also for new materials synthesis. Although peach stones exhibit adequate combustion properties, allowing their direct use with minimal physical/chemical treatment, they often need further modification in order to improve their thermal properties, where slow pyrolysis is frequently used. This study aims to provide a practical and effective solution to the revalorization of waste biomass originating from the fruit processing industry, through slow pyrolysis in order to convert this waste into carbonaceous material – biochar. The thermo-chemical conversion of raw biomass resulted in a stable material with excellent fuel properties, with higher mass energy density and grinding ability, providing biochar with properties, in energy sense, similar or even better than a coal. Biochar has a higher fixed carbon content and a higher energy potential than biomass itself, and its application as a biofuel might reduce emissions of greenhouse gases, as it reduces the amount of waste landed and increases the share of energy generated from renewable sources.

Keywords: waste biomass, peach stones, renewable sources, pyrolysis, fuel properties.

Available on-line at the Journal web address: http://www.ache.org.rs/HI/

1. INTRODUCTION

Continuous growth of energy inputs is the result of intensive technological development and ongoing society industrialization worldwide. Exhaustion of fossil fuels, increasing energy costs (especially nowadays) and environmental pollution associated with fossil fuel application have resulted in intensive efforts to find alternative energy sources. In 2014, the European Commission proposed the EU Energy Security Strategy that has identified several renewable alternatives that can deliver clean and renewable energy (RE) to replace fossil fuels, so to possibly decreasing the EU dependence on fossil fuels, diversify energy supplies and reduce greenhouse gas emissions [1]. It was expected that energy produced by biomass would contribute to more than half of the EU's RE objective (which was set to be 32 % share of RE in gross final energy consumption), identifying biomass as an important RE source to reach the EU objectives [2]. Analysis of the Serbian energy sector reveals that it is primarily based on coal combustion. According to the data contained in the Strategy for the development of the energy sector up to 2025 of the Republic of Serbia, the greatest potential of RE lies in biomass reaching 3.4 tonne of oil equivalent (142.36 GJ), which represents more than half of renewables potential. Although significant, this potential is still underutilized. One of the important biomass sources in Serbia might be food processing industry wastes, such as different fruit stones, nutshells, residues from orchards/vineyards, etc. Most of this biomass has great importance as being a source of energy for domestic purposes

by direct combustion, which is neither economical nor environmental, so these biomass sources have to be converted into forms that are more useful by using different conversion technologies [3]. Having in mind that the production of biomass waste is constantly increasing, the application of suitable biowaste materials for heat/electricity and functional materials production might significantly reduce the amount of landfill waste, slowing the depletion of fossil resources and minimizing negative impacts on the climate change.

Biomass, as one of the main renewable resources, can play a considerable role in a more diverse and sustainable energy mix. It includes all biodegradable organic materials produced as industrial and municipal waste. Although there are multiple methods for utilisation of energy stored in biomass, the most common forms include direct combustion and co-firing, which are often connected with certain risks such as fire-explosions, excessive slagging, and ash formation, as well as chlorine corrosion. Among all the techniques for biomass conversion, the pyrolysis process offers a number of benefits, including lower emissions of greenhouse gases (GHG) and reusing of all by-products. Another benefit that can be obtained by thermochemical conversion of raw biomass lies in better and easier grinding of biochars compared to raw biomass.

Pyrolysis is a thermal decomposition process, which takes place in the absence of oxygen representing one of the fundamental thermochemical conversion processes that can be used to transform biomass into the energy rich fuel materials. The pyrolysis process is mainly characterised by solid fuel thermal degradation, involving the rupture of carbon–carbon bonds and formation of carbon–oxygen bonds, most often in the temperature range from 400 to 550 °C. The yields and product quality depend on operating conditions such as heating rate, residence time and pyrolysis temperature. Biochar, solid carbon-rich material, obtained by slow pyrolysis, has a completely different set of properties in comparison to the respective feedstock, and can bring sustainable changes in securing future supply of green energy and as well turn the bioenergy into carbon-negative industry [4]. Biochar can be used as a product itself or as a component of a blended product, with a wide range of applications such as a soil improvement agent, improved energy source, remediation agent in particular environmental pollution problems, and certainly as an avenue for GHG mitigation.

In this paper, raw waste biomass generated in the Serbian food-processing sector and derived carbonaceous material, biochar, was investigated regarding some of the main physico-chemical properties with the focus on potentials of these materials for use as solid fuels.

2. MATERIALS AND METHODS

Waste biomass of peach stones (*Prunus persica* L.) was obtained from the Juice Factory Vino Župa Aleksandrovac, Serbia. After washing and drying, stones were grinded by using a vibrating disk mill (Siebtechnik GmbH, Germany), and sieved into different particle sizes, where the class between 0.1 to 0.5 mm was used for further investigations. Part of the grounded peach samples (PS) were pyrolysed at 500 °C under oxygen-limited conditions in a Nabertherm 1300 muffle furnace (Nabertherm, Germany) in order to obtain biochar (PS-B). For that purpose, argon (Ar) gas with gas flow of 100 cm^3 min^{-1} was used, where the heating rate was 10 °C min^{-1} and pyrolysis time was 1 h.

Bulk density of both samples was determined by using a filling and tapping procedure [5]. The average bulk density was determined in triplicates.

Analyses of moisture, volatile matter (VM) and ash were performed according to the ASTM D1762-84 (2007) standard. Fixed carbon (FC) was calculated by subtracting the ash, moisture and VM contents from 100 wt.%. Elemental analysis (C, H, N, and S) of PS and PS-B was conducted by using a Vario EL III CHNS Elementar Analyzer (Hanau, Germany). The content of oxygen was calculated by subtracting the C, H, N and S and ash contents from 100 wt.%. Inorganic analysis (K, Mg, Ca, Na, Fe, Si, Pb, Cu, and Ni) in ash samples (dissolved by the nitric-perchloric acid digestion method) was carried out directly from the solution by using atomic absorption spectroscopy, AAS (Perkin Elmer, AAS Analyst 300).

The mass yield of PS-B (MY, wt.%) was calculated according to equation (1) [6]:

$$\text{MY} = \frac{m_{\text{pyrolised sample}}}{m_{\text{raw sample}}} 100 \qquad (1)$$

where $m_{\text{pyrolised sample}}$ represents mass of biochar and $m_{\text{raw sample}}$ is the mass of raw peach stone sample.

Higher heating value (HHV) was calculated according to the equation (2) given by Channiwala and Parikh [7], while the energy yields (EY) and energy densifications (ED) were calculated by equation (3) proposed by Nachenius RW *et al.* [8] and equation (4), proposed by Kim D *et al.* [9].

$$HHV = 0.3491C + 1.1783H + 0.1005S - 0.1034O - 0.015N - 0.0221Ash \tag{2}$$

$$EY = MY \frac{HHV_{biochar}}{HHV_{raw\ feedstock}} \tag{3}$$

$$ED = \frac{HHV_{biochar}}{HHV_{raw\ feedstock}} \tag{4}$$

Fuel ratio (FR) was calculated as the weight ratio between contant of fixed carbon (FC) and content of volatile matter (VM), as presented ba equation (6) [6]:

$$FR = \frac{FC}{VM} \tag{5}$$

In the present study, the sample weight loss (thermogravimetric) and the rate of weight loss (derivative thermogravimetric) of both samples were performed by Simultaneous Thermal Analyzer, STA 449 F5 Jupiter (Netzsch, Germany), which operated at air flow of 100 cm^3 min^{-1}, while heating from 25 to 900 °C at a rate of 10 °C min^{-1} at atmospheric pressure.

3. RESULTS AND DISCUSSION

Main physic-chemical properties of raw peach stones and its carbonaceous solid obtained by slow pyrolysis are presented in Table 1. The elemental analysis of the investigated materials has shown very low contents of sulphur (less than 0.2 %) and nitrogen (less than 0.3 %), which might contribute to reduction of emissions of gaseous NO$_x$ and SO$_2$ pollutants if these samples are used for energy purposes.

Table 1. Chemical and fuel properties of raw peach stone, biochar and lignite samples

Parameter		PS	PS-B	Lignite [12]
Bulk density (kg m^{-3})		675	540	-
Content, wt.% (air dried)	Moisture	7.70	2.18	6.31
	VM	82.42	25.20	34.23
	Ash	0.34	0.73	44.53
	FC	9.54	71.89	14.93
Fuel properties	O/C weight ratio	0.97	0.40	-
	H/C weight ratio	0.13	0.04	-
	HHV, MJ kg^{-1}	18.89	24.58	13.12
	EY, %	-	36.62	-
	ED	1	1.3	-
	FR , %	0.12	2.85	0.44

Mass yield of peach stone biochar was found to be 28.1 %. This value is close to those presented by Weber *et al.* [11] who obtained 29.5 and 27.6 % for the mass yield of forest residue and walnut shells, respectively. The results of elemental composition analysis show a decrease in oxygen and hydrogen contents and an increase in the carbon content in pyrolysed sample as compared to the raw material. PS is composed of 47 % of carbon, 6 % of hydrogen and 46% of oxygen, while biochar contains 69 % of carbon, 3 % of hydrogen and 27 % of oxygen [12]. During the pyrolysis process, a series of chemical reactions occurs, resulting in the increase in the condensation and aromatization degrees of the material, which translates into the change in molar ratios O/C (carbonization degree) and H/C (aromatization degree) [13]. From the combustion point of view, fuels with lower O/C and H/C weight percent ratios are favourable because their application reduces energy loss, and production of smoke and water vapour [14]. As it can be seen, the O/C and H/C weight percent ratios for the PS fuel are 0.97 and 0.13. When PS was subjected to the pyrolysis process at 500 °C these ratios are reduced to 0.4 and 0.04, respectively (Table 1). These results suggested that pyrolysis changed the elemental proportions of the biomass bringing them closer to those of coal [1].

As can be also seen from Table 1, the volatile matter content of the PS material is high (about 82 wt.%), while its fixed carbon content is low (about 9.5 wt.%). For the carbonaceous materials, PS-B, the content of volatile matter is reduced, and the fixed carbon content is increased (25 and 72 wt.%, respectively). This increase in the fixed carbon content of biochar is due to the relative increase of this fraction (which is thermally stable and constant on the absolute basis) as the fraction of thermally unstable volatile matter is lost.

The ash content also increased from 0.13 wt.% for PS to 0.73 wt.% for PS-B. The mineral components in biomass do not contain aluminosilicates, but consist of simple inorganic salts of potassium, calcium, magnesium, and sodium in the form of phosphates, sulphates, and chlorides. Analysis of major components of the mineral matter in ashes of PS and PS-B revealed K, Ca and Mg as major components. The content of K was 25.4 and 19.9 wt.%, for PS and PS-B, respectively. Magnesium content ranged between 7 and 9 wt.%, while the Ca content was close to 20 wt.% for both samples. The amount of Fe was approximately 2 wt.%, while the amount of other components analysed was close to 0.1 wt.% in both samples. A characteristic feature of the biomass ash is the high content of phosphorus and potassium compounds, where the portion of phosphorous in the PS ash sample was found to be close to 27 wt.%. Considerable contents of calcium, magnesium, phosphorus, and potassium were noted in the ashes produced by combustion of both samples. Ca and Mg compounds usually increase the ash melting temperature, while the effect of K and Na is opposite [15]. These processes are highly important, given the risk of fouling and ash slagging on the walls of furnaces or heat-exchangers surfaces. Having in mind low quantities of ashes after combustion, it is assumed that this ash content cannot have significant effects on combustion behaviour of both samples.

Bulk density represents one of the factors that have to be considered for estimation of the space requirements for transport and storage. The bulk density value of PS is higher than the value for PS-B (Table1). In general, pyrolysis decreases the bulk density of biochars, which should be further subjected to a densification process in order to improve its mechanical stability, and transport and storage-related properties. This can be achieved by pelletisation, resulting in a secondary fuel with higher energy parameters suitable for use in combustion/co-firing processes [15].

Energy yield calculation is based on the mass yield and is always lower than 100 %. It is observed that the energy yield was around 36% (Table 1), which is a consequence of lower mass yield at 500 °C. The fuel ratio (FC/VM) increased from 0.12 for PS to 2.85 for PS-B (Table 1), due to the FC increase and VM decrease during thermochemical conversion and loss of volatiles in the gaseous form. Pyrolysis reactions lead to a significant increase in the mass energy density of biochars, which can be explained by the higher energy contained in carbon−carbon bonds than in carbon−oxygen and carbon−hydrogen bonds [14].

Pyrolysis considerably modified the structure of the peach stone sample, resulting in elevated carbon and FC contents, which strongly influence the high heat value. Specifically, HHV increased from 18.89 MJ kg^{-1} for the PS to 25.84 MJ kg^{-1} for the carbonaceous solid PS-B (Table 1), which are higher than the values of the most lignites. Compared with HHVs of lignites widely used in Serbia's thermal plants (which is 13.12 MJ kg^{-1} for coal from Kolubara or 14.00 MJ kg^{-1} for coal from Kostolac) [10], it can be seen that HHV of both raw biomass and biochar are significantly higher. Gross calorific value of peach stone biochar is higher by 30 % than the calorific value of the raw feedstock, which suggests that biochar is a better solid fuel than biomass. In addition, high content of volatiles in raw biomass, might induce higher emissions of CO, CO_2, NO_x, SO_2 *etc.* [16], so the direct combustion of this kind of fuel should be avoided.

TGA represents an effective way to analyse the thermal and combustion behaviour of different kinds of materials such as coal, biomass, and their blends [17]. The thermal profiles of PS and PS-B degradation obtained by thermos-gravimetric analyses are shown in Figure 1.

The curves of the raw material (Fig 1a) revealed several stages of mass loss, presenting a heterogeneous decomposition, as it has been previously described [18]. The TG and DTG curves of thermal degradation of peach stones were associated to decomposition of its main components: hemicellulose, cellulose, and lignin. The greatest mass loss associated with volatile compounds was relatively fast (220 to 380 °C) due to the thermal decomposition of hemicellulose/cellulose components, and reached 58 % of the total mass loss, indicating that a great part of the VM contained in PS has been decomposed. The curves of the raw material (Fig 1a) revealed several stages of mass loss, presenting a heterogeneous decomposition, as it has been previously described [18].
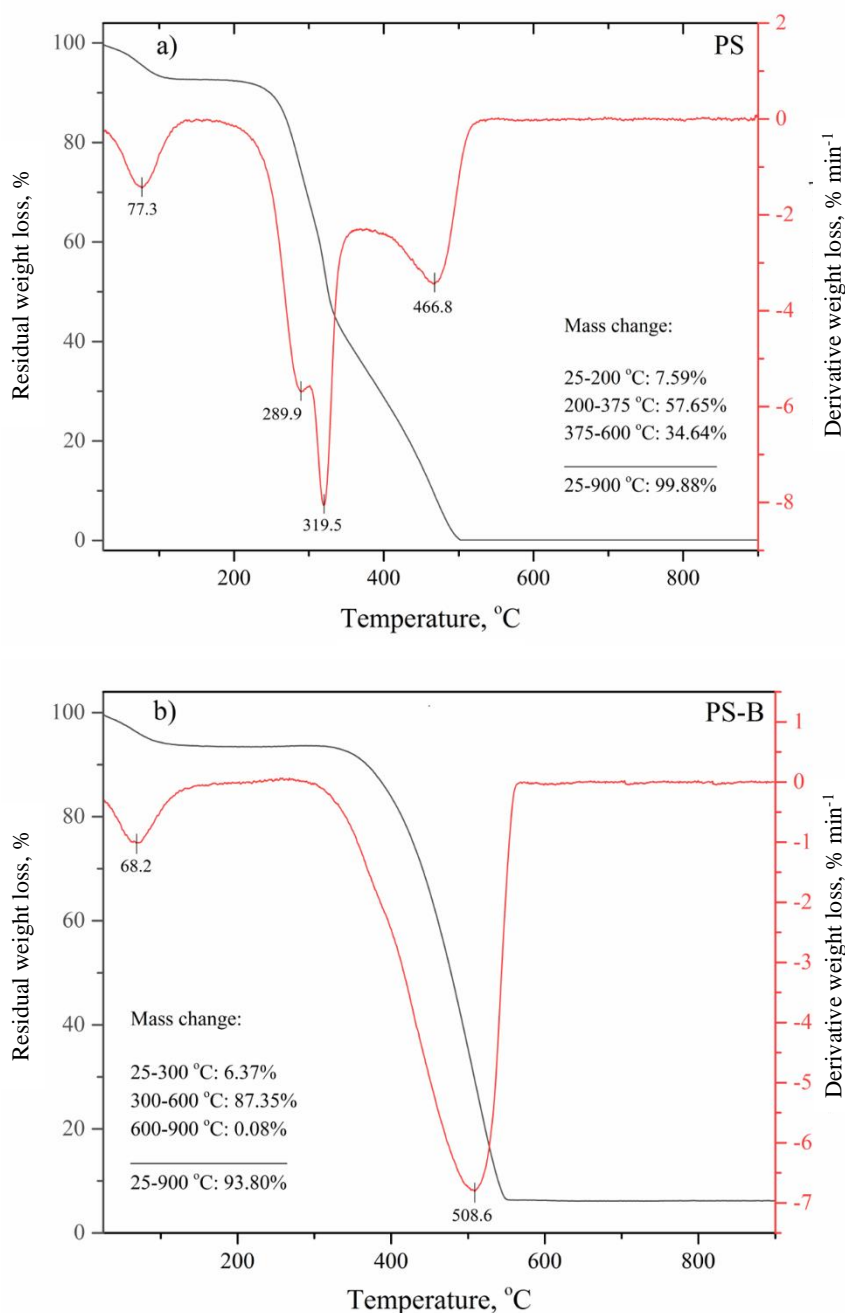
Figure 1. Thermal degradation of (a) PS and (b) PS-B obtained by slow pyrolysis at 500 °C

The TG and DTG curves of thermal degradation of peach stones were associated to decomposition of its main components: hemicellulose, cellulose, and lignin. The greatest mass loss associated with volatile compounds was relatively fast (220 to 380 °C) due to the thermal decomposition of hemicellulose/cellulose components, and reached 58 % of the total mass loss, indicating that a great part of the VM contained in PS has been decomposed. The final step of mass loss from 380 to 800 °C is given by the slow lignin degradation and carbon oxidation in air atmosphere. Compared to TG curve of native PS, TG/DTG curves of PS-B (Fig 1b) indicate smaller number of steps of mass loss. The greatest difference to the PS TG/DTG curve is the disappearance of the pronounced peak of thermal degradation of hemicellulose and cellulose, indicating their total elimination during pyrolysis. The sample PS-B was relatively unreactive at lower temperatures (up to 370 °C), indicating higher thermal stability of the obtained biochar, where the maximum weight loss occurred at 508.6 °C. Similar trends were observed in literature when comparing the TG curves of a carbonaceous material and raw olive cake [1]. During pyrolysis, cellulose and hemicellulose are thermally cleaved to

form mainly volatile products whilst lignin mainly forms char due to its stability to thermal degradation. In pyrolysis, hemicellulose decomposes at temperatures of 200 to 260 °C to form more volatiles and less tar and char than cellulose, which degrades at 240 to 350 °C to produce anhydrocellulose and levoglucosan as initial products, which further decompose to volatiles, tars, and char [19]. Lignin decomposes in the temperature range between 280 and 500 °C producing phenols and carbon–carbon bonds, resulting in higher formation of char than cellulose. According to the literature [20], the char containing ash fraction of the biomass obtained after pyrolysis, also might have application as a fuel and furthermore, it may have potential for the improvement of soil quality and might allow carbon sequestration for a long time.

4. CONCLUSION

In this paper, slow pyrolysis of lignocellulosic peach stone waste was studied as a method for preparing solid biofuel-biochar. Main changes on physical/chemical properties of biochar obtained by the thermal conversion were analysed and compared with those of the starting material. Direct application of the waste biomass as a fuel is hindered by the low bulk and energy densities, poor grinding ability and lower fuel ratio. Conversion of the raw biomass into biochar by pyrolysis can result in stable materials with excellent fuel properties, higher mass energy density and better grinding ability, providing properties in energy sense similar or even better than those of coal. The PS and PS-B materials were characterised by higher proportions of potassium compounds and lower proportions of calcium compounds, which might promote formation of low-melting eutectics. Still, the low ash content in biomass reduces the risk of slagging and fouling of heating surfaces. Biochar has higher fixed carbon and higher energy potential than biomass itself, and its application as biofuel might reduce the emissions of greenhouse gases, as it reduces the amount of waste landed and increases the share of energy generated from renewable sources.

REFERENCES

[1] Martín-Lara MA, Pérez A, Vico-Pérez MA, Calero M, Blázquez G. The role of temperature on slow pyrolysis of olive cake for the production of solid fuels and adsorbents. *Process Saf Environ Prot*. 2019; 121: 209-220. https://doi.org/10.1016/j.psep.2018.10.028

[2] Council of the European Union. Proposal for a Directive of the European Parliament and of the Council on the promotion of the use of energy from renewable sources. 2018; http://data.consilium.europa.eu/doc/document/ST-10308-2018-INIT/en/pdf

[3] Özçimen D, Ersoy-Meriçboyu A. Characterization of biochar and bio-oil samples obtained from carbonization of various biomass materials. *Renew Energ*. 2010; 35(6): 1319-1324. https://doi.org/10.1016/j.renene.2009.11.042

[4] Kwapinski W, Byrne CMP, Kryachko E, Wolfram P, Adley C, Leahy JJ, Novotny EH, Hayes MHB. Biochar from biomass and waste. *Waste Biomass Valorization*. 2010; 1: 177–189. https://doi.org/10.1007/s12649-010-9024-8

[5] Obernberger I, Thek G. Physical characterisation and chemical composition of densified biomass fuels with regard to their combustion behaviour. *Biomass Bioenergy*. 2004; 6: 653-669. https://doi.org/10.1016/j.biombioe.2003.07.006

[6] Huang YF, Cheng PH, Chiueh PT, Lo SL. Leucaena biochar produced by microwave torrefaction: Fuel properties and energy efficiency. *Appl Energy*. 2017; 204: 1018-1025. https://doi.org/10.1016/j.apenergy.2017.03.007

[7] Channiwala SA, Parikh PP. A unified correlation for estimating HHV of solid, liquid and gaseous fuels. *Fuel*. 2002; 8: 1051-1063. https://doi.org/10.1016/S0016-2361(01)00131-4

[8] Nachenius RW, van de Wardt TA, Ronsse F, Prins W. Torrefaction of pine in a bench-scale screw conveyor reactor. *Biomass Bioenergy*. 2015; 79: 96–104. https://doi.org/10.1016/j.biombioe.2015.03.027

[9] Kim D, Lee K, Park KY. Hydrothermal carbonization of anaerobically digested sludge for solid fuel production and energy recovery. *Fuel*. 2014; 130: 120-125. https://doi.org/10.1016/j.fuel.2014.04.030

[10] Janković B, Manić N, Stojiljković D, Jovanović V. The assessment of spontaneous ignition potential of coals using TGA–DTG technique. *Combust Flame*. 2020; 211: 32-43. https://doi.org/10.1016/j.combustflame.2019.09.020

[11] Weber K, Heuer S, Quicker P, Li T, Løvås T, Scherer V. An Alternative Approach for the Estimation of Biochar Yields. *Energy Fuels.* 2018; 32 (9), 9506-9512. https://doi.org/10.1021/acs.energyfuels.8b01825

[12] Lopičić Z, Avdalović J, Milojković J, Antanasković A, Lješević M, Lugonja N, Šoštarić T. Removal of diesel pollution by biochar – Support in water remediation. *Hem Ind*. 2021; 75(6): 329-338. https://doi.org/10.2298/HEMIND210514029L

[13] Jindo K, Mizumoto H, Sawada Y, Sanchez-Monedero MA, Sonoki T. Physical and chemical characterization of biochars derived from different agricultural residues. *Biogeosciences*. 2014; 11:6613–6621. https://doi.org/10.5194/bg-11-6613-2014

[14] Abdullah H, Wu H. Biochar as a Fuel: 1. Properties and grindability of biochars produced from the pyrolysis of Mallee wood under slow-heating conditions. *Energy Fuels*. 2009; 23(8); 4174-4181. https://doi.org/10.1021/ef900494t

[15] Lalak J, Martyniak D, Kasprzycka A, Żurek G, Moroń W, Chmielewska M, Wiącek D, Tys, J. Comparison of selected parameters of biomass and coal. *Int Agrophys*. 2016; 30(4): 475-482. https://doi.org/10.1515/intag-2016-0021

[16] Dołżyńska M, Obidziński S, Piekut J, Yildiz G. The utilization of plum stones for pellet production and investigation of post-combustion flue gas emissions. *Energies*. 2020; 13(19): 5107. https://doi.org/10.3390/en13195107

[17] Idris SS, Rahman NA, Ismail K, Alias AB, Rashid ZA, Aris MJ. Investigation on thermochemical behaviour of low rank Malaysian coal, oil palm biomass and their blends during pyrolysis via thermogravimetric analysis (TGA). *Bioresour Technol*. 2010; 101(12): 4584-4592, https://doi.org/10.1016/j.biortech.2010.01.059

[18] Lopičić Z, Stojanović M, Kaluđerović Radoičić T, Milojković J, Petrović M, Mihajlović M, Kijevčanin M. Optimization of the process of Cu(II) sorption by mechanically treated *Prunus persica* L. - Contribution to sustainability in food processing industry. *J Clean Prod*. 2017; 156: 95-105, https://doi.org/10.1016/j.jclepro.2017.04.041

[19] Serapiglia M, Cameron KD, Stipanovic A, Smart LB. Analysis of biomass composition using high-resolution thermogravimetric analysis and percent bark content for the selection of shrub willow bioenergy crop varieties. *Bioenergy Res*. 2009 2: 1-9. https://doi.org/10.1007/s12155-008-9028-4

[20] Laird DA. The charcoal vision: a win-win-win scenario for simultaneously producing bioenergy, permanently sequestering carbon, while improving soil and water quality. *Agron J.* 2008; 100: 178-181. https://doi.org/10.2134/agronj2007.0161

Poboljšanje energetskih svojstava lignoceluloznog otpada termohemijskom konverzijom u biočađ

Zorica Lopičić[1], Anja Antanasković[1], Tatjana Šoštarić[1], Vladimir Adamović[1], Marina Orlić[1] Jelena Milojković[1] i Milan Milivojević[2]

[1]Institut za tehnologiju nuklearnih i drugih mineralnih sirovina, Bulevar Franš d'Eperea 86, 11000 Beograd, Srbija
[2]Univerzitet u Beogradu, Tehnološko-metalurški fakultet, Karnegijeva 4, 11120 Beograd, Srbija

(Stručni rad)

Izvod

Koštice breskve, otpadna biomasa poreklom iz industrije prerade voća, dostupna u mnogim zemljama širom sveta, predstavlja obnovljivi resurs koji može imati različitu primenu. Prednosti koje se ogledaju u velikom energetskom potencijalu, malom sadržaju pepela, niskoj ceni i širokoj rasprostranjenosti, čine koštice breskve idealnim resursom za proizvodnju energije, ali i za sintezu novih materijala. Iako koštice breskve imaju svojstva koja im omogućavaju da se koriste uz minimalni fizičko-hemijski tretman, često im je potrebna dodatna modifikacija kako bi se poboljšala njihova svojstva. Jedan on načina poboljšanja energetskih karakteristika otpadne biomase predstavlja termohemijska konverzija materijala u vidu spore pirolize. Ispitivanja prikazana u ovom radu obavljena su sa ciljem obezbeđivanja praktičnog i efikasnog rešenje za revalorizaciju otpadne biomase koja potiče iz industrije prerade voća, putem spore pirolize kojom se vrši konverzija ovog otpada u ugljenični materijal – biočađ. Prikazani rezultati ukazuju na glavna svojstva dobijene biočađi u funkciji njene primene kao čvrstog goriva, istovremeno ih upoređujući sa svojstvima sirove biomase. Termohemijska konverzija polazne lignocelulozne biomase daje stabilni ugljenični material odličnih gorivih karakteristika, veće energetske gustine i boljih mehaničkih svojstava, što rezultuje energetskim svojstvima koja su bolja od uglja. Biočađ poseduje znatno veći energetski potencijal od same biomase, i njegova primena kao biogoriva može redukovati emisiju gasova sa efektom staklene bašte, pri čemu se istovremeno smanjuje količina deponovanog otpada ali i povećava udeo energije generisane iz obnovljivih izvora.

Ključne reči: Otpadna biomasa, koštice breskve, obnovljivi izvori, piroliza, osobine goriva

Microstructure, hardness and fracture resistance of P235TR1 seam steel pipes of different diameters

Walid Musrati[1], Bojan Međo[2], Ivana Cvijović-Alagić[3], Nenad Gubeljak[4], Primož Štefane[4], Zoran Radosavljević[5] and Marko Rakin[2]

[1]University of El Mergib, Faculty of Engineering, Khoms, Libya
[2]University of Belgrade, Faculty of Technology and Metallurgy, Belgrade, Serbia
[3]University of Belgrade, Institute of Nuclear Sciences "Vinča", Belgrade, Serbia
[4]University of Maribor, Faculty of Mechanical Engineering, Maribor, Slovenia
[5]Research and Development Institute Lola, Belgrade, Serbia

Abstract

Steel pipelines in industrial plants consist of different elements, including seamless and/or welded (seam) pipes. Properties of welded pipes, including their fracture behaviour, depend on the characteristics of both, the base metal, and the weld metal. In this work, two seam pipes are considered having different diameters and manufactured of P235TR1 steel. Hardness and microstructure were examined on the samples which contained the seam zone, to capture the influence of heterogeneity. Fracture resistance of the pipeline material, *i.e.* of both base metals and both seams, was determined by experimental examination of the recently proposed Pipe ring notch bending specimens with sharp stress concentrators. Differences between the two tested pipes, including the influence of the heterogeneity caused by the welded joint, were determined by comparison of the crack growth resistance curves. Effects of the initial stress concentrator shape, sharp machined notch or fatigue pre-crack are discussed.

Keywords: pipe ring testing; microstructural analysis; welded joint hardness; fracture mechanics; non-standard specimens.

Available on-line at the Journal web address: http://www.ache.org.rs/HI/

1. INTRODUCTION

Pipelines in process industry plants can contain different types of sharp and/or blunt defects. Regardless of the moment when these defects occur, or their mechanism of initiation/development, they represent a risk that can endanger safe exploitation of the pipeline and the connected equipment. Therefore, the load carrying capacity, integrity, and failure resistance of pipes, as well as other process equipment elements (vessels [1,2], nozzles [3], valves [4], *etc.*), were considered in numerous studies, some of which will be mentioned in this section.

Generally, an important source of initial defects in pipelines are welds, which can be formed during fabrication (axial or spiral welds on seam pipes) or assembly (circumferential - girth joints). Examples of works which deal with the seam pipes are papers [5-7]. Quality testing for the pipes fabricated by different welding techniques is considered in [5], while fracture resistance comparison between the weld zones is presented in [6,7]. Mechanical properties and microstructure of the seam steel pipes were examined in literature [8], with a consideration of on-line spray water cooling (OSWC) process applied during manufacturing of the welded pipes. Besides longitudinally welded pipes, spiral welded pipes typically having larger diameters are also used in some applications. In a study on this type of pipes [9] influences of material anisotropy and spiral welding were analysed on the pipe behaviour under the loading.

Standards for the fracture toughness measurement typically require thick specimens, *i.e.* the requirement for the plane strain state is imposed. Two most frequently used standard specimens are SENB (Single Edge Notch Bending) and CT (Compact Tension) specimens. Such specimens for testing the pipeline material fracture resistance can be fabricated

by cutting the pipes only if the pipe wall is relatively thick. To fabricate the required specimen geometries for thin-walled pipes, predominantly used in most industrial applications, is very problematic.

One of the alternative specimen geometries is proposed in literature [10]; termed the curved CT specimen. Their intention is to obtain the stress and stress distribution, which resemble those in a pressurised pipe with the initial defect in axial direction. However, the testing procedure requires fabrication of the appropriate rig which corresponds to only one pipe diameter.

Single edge notched tension (SENT) specimen type is applied by many authors in fracture analysis of pipes with circumferential position of the initial defect, including those positioned in the girth welded joints of the pipes. Comparison of SENT and SENB specimens, which have the same shape but different loading conditions, is shown in literature [11-13]. These studies revealed that SENB specimens give conservative results in some cases, and that SENT specimens are more appropriate for examination of pipes with circumferential cracks exposed to axial loading. As a result of the efforts of the researchers worldwide, SENT specimen geometry has been standardised in several countries. Unfortunately, it is not convenient for failure assessment of pipes exposed dominantly to internal pressures, where the most critical defects are positioned axially (*i.e.* critical stress is the hoop stress).

In several studies, tensile compact pipe (CP) specimens were proposed and examined [14,15]. This specimen consists of a pipe segment with a circumferential initial defect and two levers welded to its sides. The role of the levers is to transfer the loading from the testing machine.

A series of interesting thin-walled non-standard geometries were also proposed [16,17], where loading conditions and additional tools resemble the standard specimens. They are fabricated by cutting and subsequent shaping of the pipe segments and include both axial and circumferential positions of the pre-cracks.

A new specimen geometry (curved SENB) was also proposed [7] and it was compared with the standard CT specimen. This study was performed on seam API 5L X52 steel pipes. Cutting of the standard CT specimens was possible because the considered pipe had relatively thick walls. The work also included investigation of the seam fracture behaviour, as well as the difference between C-R and C-L directions (C-circumferential, R-radial, L-longitudinal).

Generally, all mentioned studies aimed at providing new possibilities for fracture examination of pipeline materials. They were performed on different pipeline steels, since many different materials are used in the process industry, depending on exploitation conditions of a particular plant/pipeline. The significance of material selection for pipelines is discussed in [18].

In this work, pipeline materials of two seam steel pipes were assessed by application of the recently proposed PRNB (Pipe ring notch bending) specimens [19], which have been experimentally and numerically examined and established previously [20-23]. The influence of residual stresses was also considered [24], while micromechanical analysis was the topic of a previous study [25]. The initial experimental results obtained on the larger-diameter pipes considered here were shown previously in [26] but were limited only to the pipe fracture behaviour. Here, microstructural analysis and hardness for both pipes are considered, and their fracture resistances are compared and discussed.

2. MATERIALS AND METHODS

Two groups of samples (for hardness and microstructural analysis) and specimens (for fracture examination) were prepared from seam pipes of two different diameters (Arcelor Mittal, Romania; the pipes were new, *i.e.* not previously used). The material of both pipes is P235TR1 steel, in accordance with the EN 10217-1 standard [27]. Chemical composition and tensile properties, obtained from the manufacturer certificate, are shown in Table 1, along with the standard requirements. In the Table, $R_{p0.2}$ is the conventional (proof) strength, R_m is the ultimate tensile strength and A is the elongation at fracture. Despite some deviations, properties of both pipe materials are within the bounds set by the standard for this material grade.

The samples for microstructural characterization and hardness testing were prepared by the standard metallographic technique, *i.e.* grind with SiC abrasive papers, polished by using diamond suspension, and cleaned in an ultrasonic bath with ethanol. The metallographically prepared samples were next subjected to etching with the Nital

reagent, containing 100 cm³ of 96% ethanol and 3 cm³ of 65 % nitric acid, for 30 s. The microstructural characteristics of both pipe materials were examined by optical microscopy (OM, Carl Zeiss Opton Axioplan, Carl Zeiss AG, Germany).

Table 1. Chemical composition and tensile properties of steel P235TR1 ($R_{p0.2}$ is the conventional (proof) strength, R_m is the ultimate tensile strength and A is the elongation at fracture) [27,28]

	Content, %						$R_{p0.2}$ / MPa	R_m / MPa	A / %
	C	Mn	S	P	Si	Al			
P235TR1 standard requirements	max 0.16	max 1.2	max. 0.02	max 0.025	max. 0.35	-	min. 235	360-500	min. 25
pipe ext. diam. 88.9 mm	0.08	0.52	0.013	0.014	0.02	0.043	389	417	40.2
pipe ext. diam. 168.3 mm	0.13	0.54	0.012	0.01	0.02	0.052	328	420	38

Figure 1 shows the samples used for hardness measurement; welded joint zone is included in examination. Hardness is measured by using a Buehler microindentation hardness tester (model Micromet 5101, Buehler, Germany) by applying a load of 1000 gf (9807 mN) for 15 s at positions along the measurement lines shown on each sample, while the seam width is determined by the microstructural analysis. The samples are denoted with respect to the pipe diameter: samples S168 (Figure 4a) and S89 (Figure 4b) for diameters 168.3 and 88.9 mm, respectively.
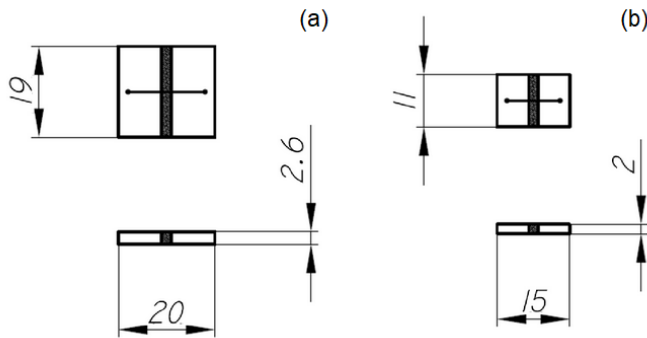
Figure 1. Samples for hardness measurement: (a) S168 and (b)S89

Fracture resistance, *i.e.* resistance to crack growth by ductile mechanism, is tested on recently proposed pipe ring notch bending specimens - PRNB. These specimens, as mentioned previously, have been developed as a convenient and reliable way for fracture testing of pipeline materials, especially thin-walled ones. The main specimen dimensions: external diameter *D*, width *W*, wall thickness *B* and sharp stress concentrator length a_0, are shown in Figure 2 and Table 2.
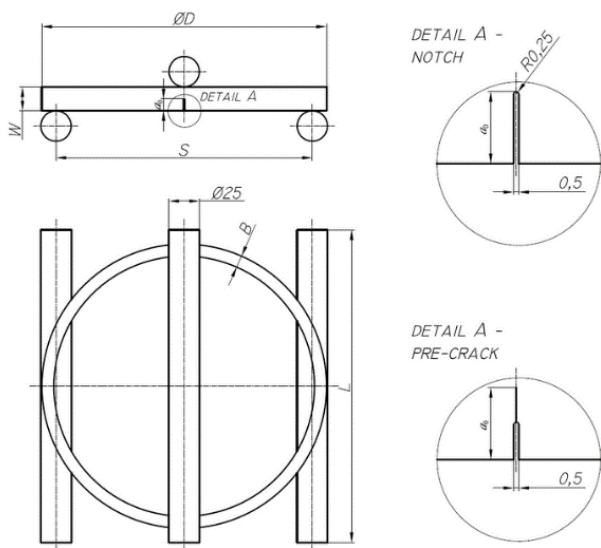
Figure 2. Specimen dimensions and testing scheme (Reprinted with permission from [23], Copyright by Elsevier, 2023

Machined notches were fabricated as stress concentrators on most specimens and fatigue pre-cracks were formed on a smaller-diameter specimen. The notches were formed by electrical discharge machining (EDM, Robofil 400, Charmilles, Switzerland), with the radius of 0.25 mm. Distance between the supports *S* is equal to 90 % of the external diameter for all specimens.

Table 2.Measures of pipe ring specimens: D -external diameter, W - width, B - wall thickness and a_0 - sharp stress concentrator length

	Position of the stress concentrators	*D* / mm	*B* / mm	*W* / mm	*W/B*	a_0/W
S-WM(168)-1	in WM and BM	168.18	3.21	12.99	≈ 4	0.5
S-WM(168)-2	in WM and BM	168.43	3.46	21.05	≈ 6	0.5
S-WM(168)-3	in WM and BM	168.21	3.24	19.26	≈ 6	0.5
S-BM(168)-6	in BM	168.28	3.22	19.23	≈ 6	0.5
S-WM(89)-7	in WM and BM	88.28	2.71	11.05	≈ 4	0.5
S-WM(89)-8	in WM and BM	88.59	2.58	10.48	≈ 4	0.5
S-BM(89)-9	in BM	88.62	2.55	10.30	≈ 4	0.45
S-BM(89)-10C	in BM - pre cracks	88.46	2.63	10.48	≈ 4	0.25 + crack = 0.38/0.46

Note: WM and BM stand for the weld metal (seam) and base metal, respectively

Digital image correlation (DIC) system Gom Aramis (Gom Metrology, Germany) [4,29,30] is applied for tracking the parameters related to deformation during the testing on the universal testing machine (model 1255, Instron, USA): displacement field, strain field, as well as CMOD - Crack mouth opening displacement and CTOD - Crack tip opening displacement. Aramis system consists of two cameras, acquisition equipment and software.

After the fracture testing, plastically deformed ring specimens are broken, after cooling in liquid nitrogen; this resulted in a brittle final fracture. Prior to this, the specimens were exposed to heating (in a furnace, during 30 min) to 400 °C, which enables a clear final crack distinction; this procedure is often called heat-tinting. Examination of fracture surfaces is performed on a stereo microscope (model SZX12, Olympus, Japan).

3. RESULTS AND DISCUSSION

3. 1. Hardness and microstructure

Microstructural analysis is performed by optical microscopy of etched welded joint (seam) samples. Figures 3-5 (sample S168) are obtained for the larger-diameter pipe, while the other microphotographs are obtained on the smaller-diameter pipe (Figures 6-8, sample S89) [31].

Two microconstituents are observed in the base metal (BM), shown in Figures 3a and 6a for both specimens: ferrite and pearlite. The former can be distinguished as white grains in these figures, while the latter is visible as dark islands positioned at the ferrite grain boundaries.

Figures 3b and 6b correspond to the weld metal (WM) of both pipes, and they are shown alongside each base metal. Ferrite can be seen as side plates nucleated at the austenite grain boundaries; additionally, fine acicular ferrite and ferrite-carbide aggregates (pearlite) are found. In the weld metal of the lower-diameter pipe (Figure 6b - sample S89), primary intragranular polygonal ferrite is also noticed.

Figures 4 and 5 contain transitions between the welded joint zones for the sample S168. In Figure 4, the transition base metal - heat affected zone (HAZ) is shown and the boundary is marked. Figure 4b represents a magnified part of Figure 4a marked by the rectangle. Inspection of the microstructure of this part of the transition zone reveals similar structures of the base metal and the heat affected zone. Microstructure in HAZ similar to the WM structure is observed only close to the fusion line, Figure 5.

Analysis of the variation of microstructure enabled estimation of the heat affected zone width: ~0.35 mm for sample S168 and cca. 0.4 mm for sample S89. In a similar way, overall variation of microstructure along the entire joint gives approximate weld metal widths: 2.6 mm for sample S168 and 2 mm for sample S89.
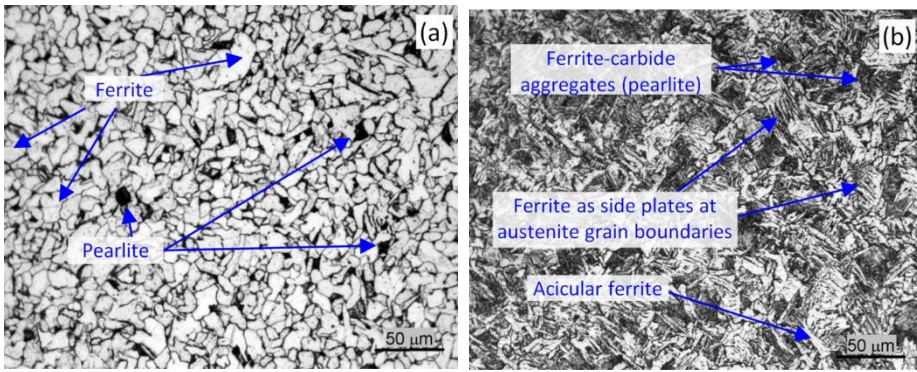
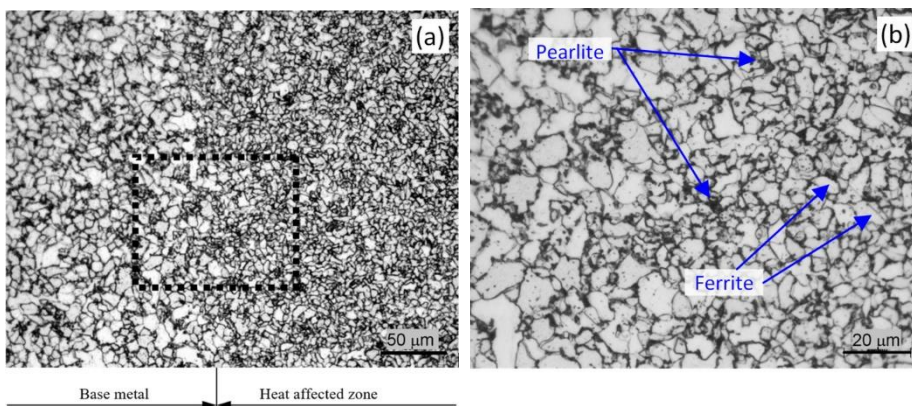*Figure 3. Micrographs of sample S168: (a) base metal and (b) weld metal*

Figure 4. Micrographs of sample S168: (a) transition base metal - heat affected zone; (b) rectangular zone marked in (a) at higher magnification
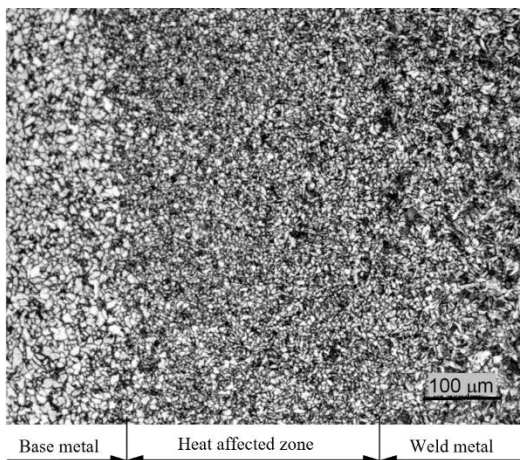

Figure 5. Micrograph of sample S168: Transition base metal - heat affected zone - weld metal
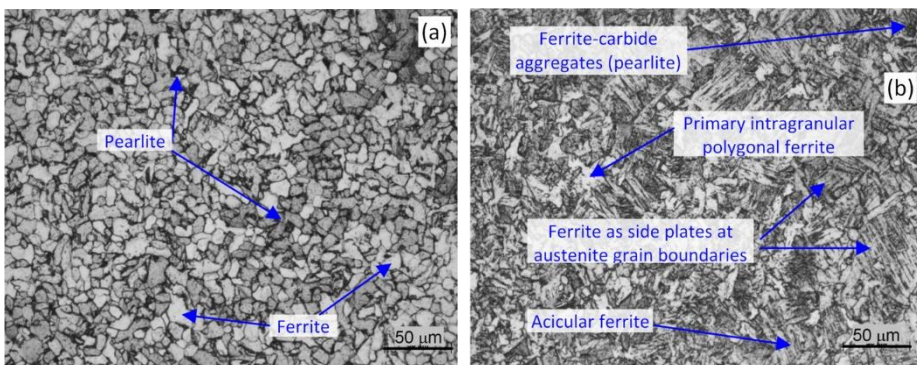

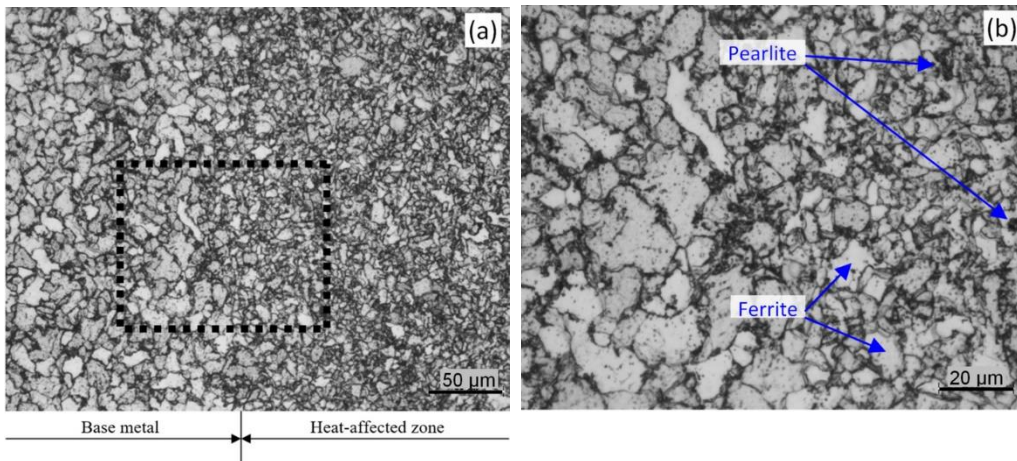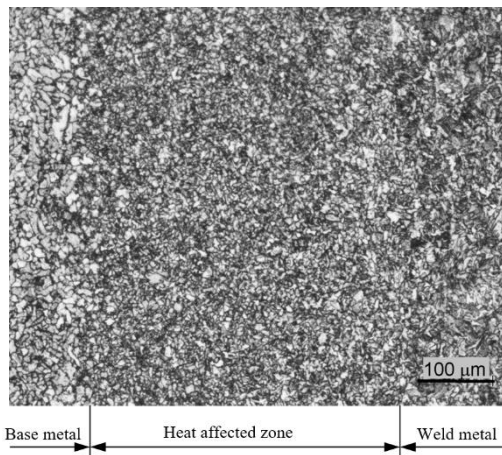*Figure 6. Micrographs of sample S89: (a) base metal and (b) weld metal*

Figure 7. Micrographs of sample S89: (a) transition base metal - heat affected zone; (b) rectangular zone marked in (a) at higher magnification

Figure 8. Micrograph of sample S89: Transition base metal - heat affected zone - weld metal

Variation in hardness across the seam region is presented in Figure 9. In these diagrams, the position and width of WM and HAZ, determined from the microphotographs, are also marked for both samples. Since the obtained values are higher in the seam zone, this hardness profile indicates overmatching.
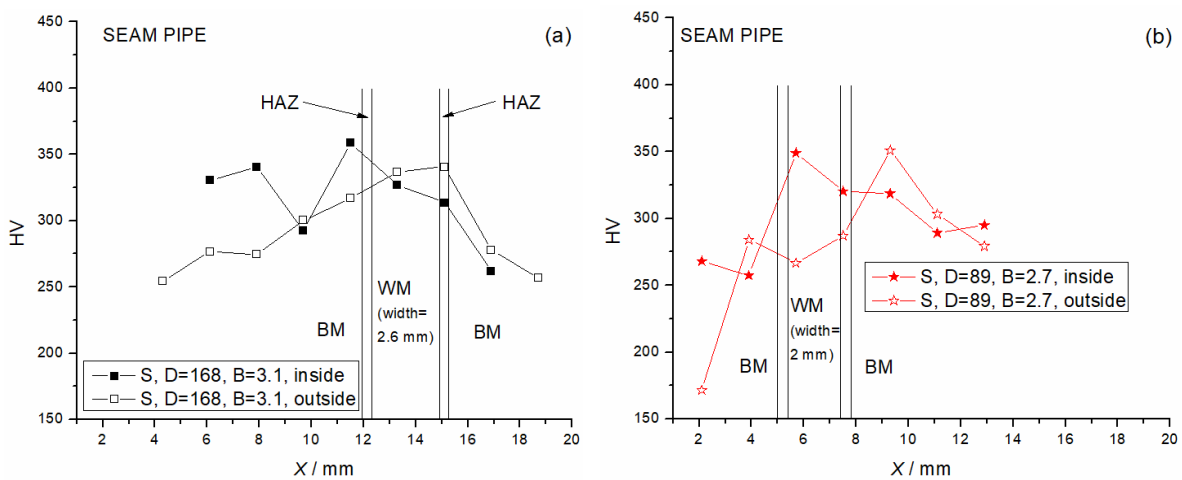
Figure 9. Variations in hardness across the joint - (a) sample S168 and (b)sample S89

Hardness is generally affected by the composition and ratio of phases present in the microstructure. Accordingly, the ratio of pearlite and ferrite in the microstructure shows a decisive influence on the hardness level of every single

region. Since pearlite is characterized by higher carbide content as compared to ferrite, the seam regions with higher contents of this phase are characterized by higher hardness. On the other hand, regions with more ferrite in the microstructure show lower hardness. In the analysed seams, a somewhat larger amount of pearlite is observed in the weld metal than in the base metal which corresponds to the higher hardness of this region. An increase in hardness in the heat affected zone and the base metal close to this zone was also observed.

3. 2. Fracture resistance examination

The final observed crack shape (Fig. 10) is characteristic for ductile fracture, *i.e.* growth of the crack is the most pronounced in the central part, due to the high stress triaxiality (*i.e.* much higher than in the vicinity of the specimen surfaces). This is obtained for both machined notches (Figs 10a,b), and fatigue pre-crack (Fig. 10c).

However, fatigue pre-cracking results in an uneven initial crack. This is caused by the cylindrical specimen shape, and fatigue crack growth is more pronounced on the internal side of the specimen (right-hand side of Figure 10c) than on the external one. However, even though the initial pre-crack is uneven, ductile crack growth is still relatively uniform, *i.e.* the crack length is the largest near the mid-thickness of the specimen.
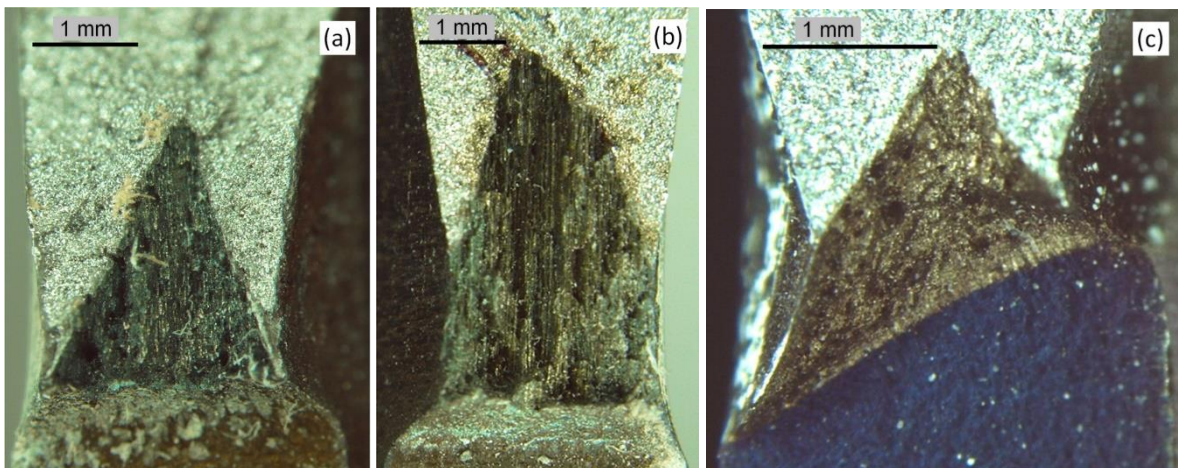
Figure 10. Photographs of fracture surfaces obtained from stereo microscope: (a, b) two PRNB specimens with an initial notch and (c)one with an initial fatigue pre-crack

As it was discussed and concluded previously [20], machined notch is a suitable stress concentrator for this geometry, and it gives reliable and repeatable results. As mentioned previously and shown in Figure 10, symmetric blunting and crack growth are obtained on the notched specimens. Also, it is possible to obtain a more precise and straight stress concentrator shape than for the fatigue pre-cracked specimens.

Figure 11 presents *F*-CMOD curves for the examined specimens (Fig. 11a for diameter 168.3 mm and Fig. 11b for diameter 88.9 mm); the force is obtained from the testing machine, while CMOD values are determined by the DIC system.

In these diagrams, basic measures of the specimens are shown alongside the specimen labels: the position of the stress concentrator, external diameter × wall thickness, ratio a_0/W, ratio W/B. For example, notation "Seam, 168.3x3.2, a0.5, W4" means that the specimen has one of the notches in the seam, diameter 168.3 mm, wall thickness $B = 3.2$ mm, ratio $a_0/W = 0.5$ and ratio $W/B = 4$ [31]. Near the legend, the stress concentrator position (WM or BM) is shown in all diagrams. The specimen 10C contains fatigue pre-cracks (therefore, letter C is included in its denotation), while the other ones contain machined notches.

The *F*-CMOD curves can be used to compare the load carrying capacity of structures with similar geometries. For example, in Figure 11a specimen 1 has significantly lower force values because its width-to-thickness ratio is 4, while for the remaining three specimens this value is 6. Also, there are some differences in the shape of these curves for the base and weld metal, if specimen 6 (BM) is compared with the specimens 2 or 3 (WM). However, these curves do not describe the development of fracture through the material, *i.e.* they do not include the crack growth data.
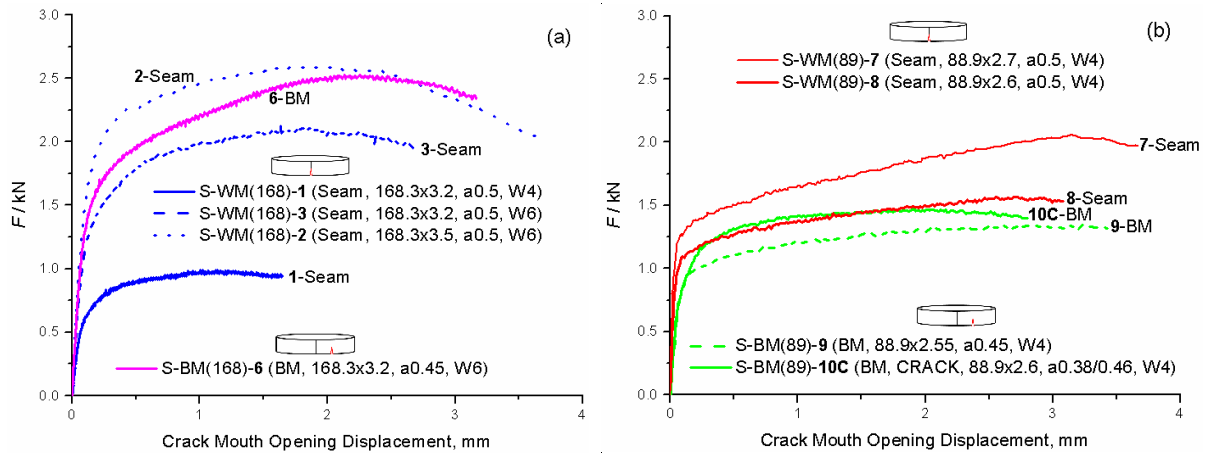
Figure 11. F-CMOD curves: ring specimens with D = 168.3 mm (a) and D = 88.9 mm (b); basic measures of the specimens with the specimen labels: e.g. "Seam, 168.3x3.2, a0.5, W4" means that the specimen has one of the notches in the seam, diameter 168.3 mm, wall thickness B = 3.2 mm, ratio a_0/W = 0.5 and ratio W/B = 4; the specimen 10C contains fatigue pre-cracks, while the other contain machined notches

The crack growth through all specimens is determined by the normalisation method [32], and these values are used in forming CTOD-Δ*a* curves, *i.e.* the crack growth resistance curves. In order to apply the normalisation method, the final crack length is measured on fracture surfaces; three of such surfaces are presented in Figure 10. In the following diagrams, δ_5 technique was used for measurement of CTOD, in accordance with the literature [33]. Therefore, denotation (CTOD-δ_5) is used and it is obtained by measurement by using the Aramis system, as the increase in the distance of two points, which are initially 5 mm apart (2.5 mm on each side of the initial tip of the stress concentrator).

CTOD-Δ*a* curves for both pipe base metals are shown in Figure 12; this diagram reveals two important trends. First, the smaller pipe is significantly more resistant to crack growth than the larger pipe. Also, the result obtained for the fatigue pre-cracked specimen S-BM(89)10C is very similar to that obtained for the specimen with notches S-BM(89)9.
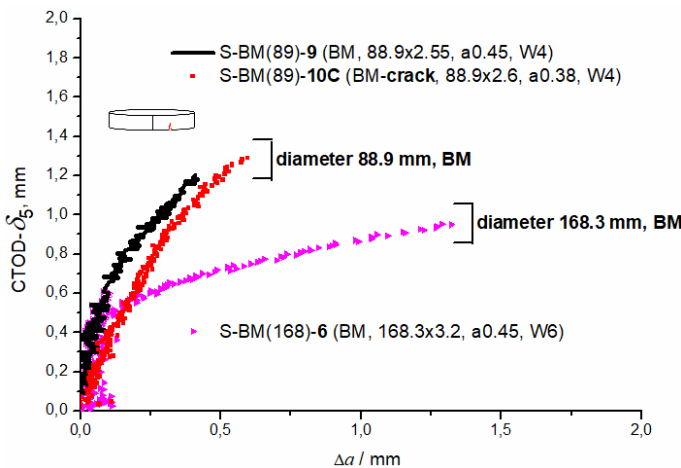
Figure 12. CTOD-Δa curves of the base metal for the two pipe diameters

In Figure 13, crack growth resistance curves for weld metals (seams) for both pipe diameters are shown. Similarly as for the base metals, the seam of the smaller-diameter pipe exhibits higher fracture resistance.

Finally, in order to have an overall view of the fracture testing results, all 4 materials are shown in Figure 14, *i.e.* both base metals and both weld metals (seams). Higher resistance to crack growth of the lower-diameter pipe is mentioned above. However, there is also another significant difference: the base metal and the seam in the smaller diameter pipe show more similar fracture behaviours than those in the larger diameter pipe.
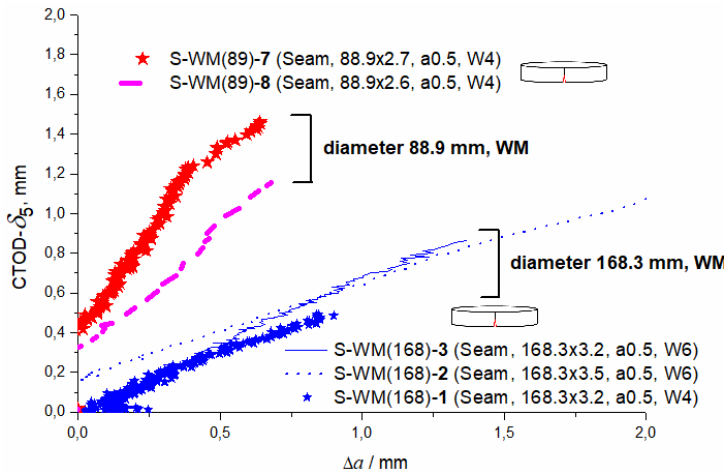
Figure 13. CTOD-Δa curves of the seam for the two pipe diameters

Generally, the results show a pronounced dependence of fracture resistance on material properties, rather than on the specimen or stress concentrator dimensions, which is certainly favourable.
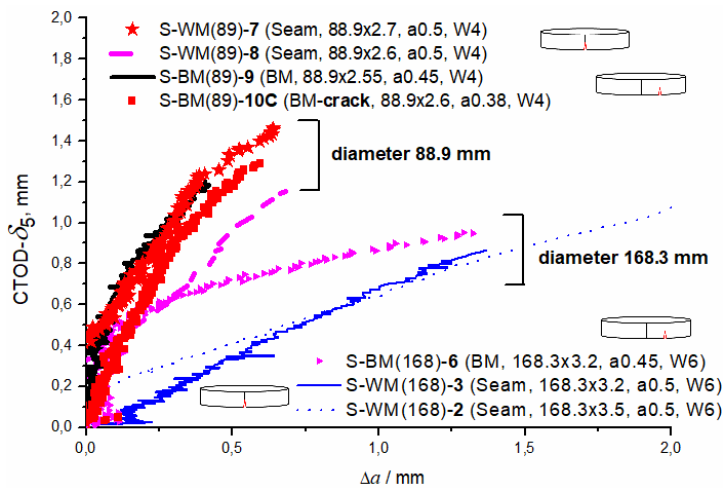

Figure 14. CTOD-Δa curves of the base metal and seam for the two pipe diameters

4. CONCLUSION

This work presents examination of hardness, microstructure and fracture toughness of two seam pipes fabricated of the same material, but with different diameters. Despite the similarity of the materials, hardness and microstructure, the base metals exhibit significantly different fracture resistances, expressed by the crack growth resistance curves. Also, another difference is determined: while the larger-diameter pipe base metal is more resistant to fracture than its weld metal, the smaller-diameter pipe exhibits different behaviour – the base and weld metals are characterised by similar fracture resistances. It can be said that testing of the pipe ring specimens successfully captured these differences between the examined pipes. The influence of the stress concentrator shape is also assessed on one of the smaller-diameter ring specimens, and an EDM notch resulted in similar fracture resistance as a fatigue pre-crack for this material. Having in mind that the vast majority of pipelines in process industry consist of thin-walled pipes, the new specimen geometry has a good potential for application in material selection, fracture testing, integrity assessment and safety assurance procedures.

REFERENCES

[1] Moattari M, Moshayedi H, Sattari-Far I. Application of new constraint based Master Curve in fracture assessment of pressure vessels. *Int J Pres Ves Pip*. 2019; 174: 25–31. https://doi.org/10.1016/j.ijpvp.2019.05.009

[2] Golubović T, Sedmak A, Spasojević Brkić V, Kirin S, Veg E. Welded joints as critical regions in pressure vessels - case study of vinyl chloride monomer storage tank. *Hem Ind*. 2018; 72: 177–182. https://doi.org/10.2298/HEMIND171009006G

[3] Murtaza UT, Javed Hyder M. Fracture analysis of the set-in nozzle of a PWR reactor pressure vessel - Part 1: Determination of critical crack. *Eng Fract Mech*. 2018; 192: 343–361. https://doi.org/10.1016/j.engfracmech.2016.03.049

[4] Mitrović N, Petrović A, Milošević M, Momčilović N, Mišković Ž, Maneski T, Popović P. Experimental and numerical study of globe valve housing. *Hem Ind*. 2017; 71: 251–257. https://doi.org/10.2298/HEMIND160516035M

[5] Šarkoćević Ž, Rakin M, Arsić M, Sedmak A. Fabrication of high strength seam welded steel tubes and quality indicator testing. *Struct Integr Life*. 2008; 8: 81–98. http://divk.inovacionicentar.rs/ivk/ivk08/ivk0802-1.html

[6] Choupani N, Asghari V, Kurtaran, H. Fracture Characterization of Base Metal, Seam Weld, and Girth Weld of Welded Line Pipe Steel at Room and Low Temperatures. *J Mater Eng Perf*. 2021; 30: 1046–1053. https://dx.doi.org/10.1007/s11665-020-05431-3

[7] Angeles-Herrera D, Albiter-Hernández A, Cuamatzi-Meléndez R, González-Velázquez JL. Fracture toughness in the circumferential-longitudinal and circumferential-radial directions of longitudinal weld API 5L X52 pipeline using standard C(T) and nonstandard curved SE(B) specimens. *Int J Fract*. 2014; 188: 251–256. https://dx.doi.org/10.1007/s10704-014-9949-1

[8] Chen Z, Chen X, Zhou T. Microstructure and Mechanical Properties of J55ERW Steel Pipe Processed by On-Line Spray Water Cooling. *Metals*. 2017; 7: paper No. 150. https://doi.org/10.3390/met7040150

[9] Van Minnebruggen K, Hertelé S, Thibaux P, De Waele W. Effects of specimen geometry and anisotropic material response on the tensile strain capacity of flawed spiral welded pipes. *Eng Fract Mech*. 2015; 148: 350–362. https://doi.org/10.1016/j.engfracmech.2015.04.031

[10] Gajdos L, Sperl M. Evaluating the integrity of pressure pipelines by fracture mechanics. In: *Applied Fracture Mechanics*, London: InTech Publishing; 2012: 283–310. https://dx.doi.org/10.5772/51804

[11] Zhang ZL, Xu J, Nyhus B, Østby E. SENT (single edge notch tension) methodology for pipeline applications. *In: Proceedings of the 18th European Conference on Fracture*, Dresden, Germany, 2010, pp. 1-8, published on CD.

[12] Xu J, Zhang ZL, Østby E, Nyhus B, Sun DB. Effects of crack depth and specimen size on ductile crack growth of SENT and SENB specimens for fracture mechanics evaluation of pipeline steels. *Int J Pres Ves Pip*. 2009; 86: 787–797. https://dx.doi.org/10.1016/j.ijpvp.2009.12.004

[13] Xu J, Zhang ZL, Østby E, Nyhus B, Sun DB. Constraint effect on the ductile crack growth resistance of circumferentially cracked pipes. *Eng Fract Mech*. 2010; 77: 671–684. https://dx.doi.org/10.1016/j.engfracmech.2009.11.005

[14] Mahajan G, Saxena S, Mohanty A. Numerical characterization of compact pipe specimen for stretch zone width assessment. *Fatigue Fract Engng Mater Struct*. 2016; 39: 859–865. https://dx.doi.org/10.1111/ffe.12400

[15] Koo JM, Park S, Seok CS. Evaluation of fracture toughness of nuclear piping using real pipe and tensile compact pipe specimens. *Nucl Eng Design*. 2013; 259: 198–204. https://dx.doi.org/10.1016/j.nucengdes.2013.03.001

[16] Bergant M, Yawny A, Perez Ipiña J. Experimental determination of J-resistance curves of nuclear steam generator tubes. *Eng Fract Mech*. 2016; 164: 1–18. https://dx.doi.org/10.1016/j.engfracmech.2016.07.008

[17] Bergant M, Yawny A, Perez Ipiña J. Numerical study of the applicability of the g-factor method to J-resistance curve determination of steam generator tubes using non-standard specimens. *Eng Fract Mech*. 2015; 146: 109–120. https://dx.doi.org/10.1016/j.engfracmech.2015.07.059

[18] Capelle J, Pluvinage G, Modification of failure risk by the use of high strength steels in pipelines, *Struct Integr Life*. 2013: 13; 23–27 http://divk.inovacionicentar.rs/ivk/ivk13/ivk1301-4.html

[19] Matvienko YG, Gubeljak N. Model for Determination of crack-resistance of the pipes. Patent No. RU 2564696 C, 2015 (in Russian)

[20] Gubeljak N, Likeb A, Matvienko Y. Fracture toughness measurement by using pipe-ring specimens. *Proc Mater Sci*. 2014; 3: 1934–1940. https://dx.doi.org/10.1016/j.mspro.2014.06.312

[21] Likeb A. Suitability of pipe-ring specimen for determination of fracture toughness. PhD Thesis, University of Maribor, Faculty of Mechanical Engineering, Slovenia, 2014 (in Slovenian)

[22] Likeb A, Gubeljak N, Matvienko Y. Finite element estimation of the plastic η_{pl} factors for pipe-ring notched bend specimen using the load separation method. *Fatigue Fract Eng Mater Struct*. 2014; 37: 1319–1329. https://dx.doi.org/10.1111/ffe.12173

[23] Musraty W, Medjo B, Gubeljak N, Likeb A, Cvijović-Alagić I, Sedmak A, Rakin M. Ductile fracture of pipe-ring notched bend specimens - micromechanical analysis. *Eng Fract Mech*. 2017; 175: 247–261. https://dx.doi.org/10.1016/j.engfracmech.2017.01.022

[24] Damjanović D, Kozak D, Gubeljak N. The influence of residual stresses on fracture behavior of Pipe Ring Notched Bend specimen (PRNB), *Eng Fract Mech*. 2019; 205: 347–358. https://dx.doi.org/10.1016/j.engfracmech.2018.10.016

[25] Musrati W, Međo B, Gubeljak N, Štefane P, Veljić D, Sedmak A, Rakin M. Fracture assessment of seam and seamless steel pipes by application of the ring-shaped bending specimens. *Theor Appl Fract Mech*. 2019; 103: paper No. 102302. https://dx.doi.org/10.1016/j.tafmec.2019.102302

[26] Musraty W., Međo B., Gubeljak N., Štefane P., Radosavljević Z., Burzić Z., Rakin M. Seam pipes for process industry - fracture analysis by using ring-shaped specimens. *Hem Ind*. 2018; 72: 39–46. https://dx.doi.org/10.2298/HEMIND170530014M

[27] EN 10217-1: Welded steel tubes for pressure purposes. Technical delivery conditions Electric welded and submerged arc welded non-alloy steel tubes with specified room temperature properties, 2019.

[28] Inspection certificates No. 31042 and No. 33131/1, Arcelor Mittal Tubular Products Iasi S.A., Romania, 2015.

[29] GOM Precise Industrial 3D Metrology. www.gom.com. Accessed in January, 2023.

[30] Gubeljak N. Application of stereometric measurement on structural integrity. *Struct Integr Life*. 2006; 6: 65–74. http://divk.inovacionicentar.rs/ivk/ivk06/ivk0601-7.html

[31] Musrati W. Characterisation of damage and fracture of pipeline material using ring-shaped specimens. PhD Thesis, University of Belgrade, Faculty of Technology and Metallurgy, Serbia, 2019.

[32] ASTM E1820: Standard test method for measurement of fracture toughness. 2015.

[33] Displacement gauge system for applications in fracture mechanics. Patent Publication, GKSS Research Center, Geesthacht, Germany, 1991.

Otpornost prema lomu, tvrdoća i mikrostruktura šavnih cevi različitog prečnika izrađenih od čelika P235TR1

Walid Musrati[1], Bojan Međo[2], Ivana Cvijović-Alagić[3], Nenad Gubeljak[4], Primož Štefane[4], Zoran Radosavljević[5] i Marko Rakin[2]

[1]University of El Mergib, Faculty of Engineering, Khoms, Libya
[2]Univerzitet u Beogradu, Tehnološko-metalurški fakultet, Beograd, Srbija
[3]Univerzitet u Beogradu, Institut za nuklearne nauke "Vinča", Beograd, Srbija
[4]Univerzitet u Mariboru, Mašinski fakultet, Maribor, Slovenija
[5]Istraživačko-razvojni institut Lola, Beograd, Srbija

(Naučni rad)

Izvod
Čelični cevovodi u industrijskim postrojenjima se sastoje od različitih elemenata, uključujući bešavne i/ili zavarene (šavne) cevi. Osobine šavnih cevi, uključujući ponašanje materijala cevi pri lomu, zavise i od osnovnog metala i od metala šava. U ovom radu razmatrane su dve šavne cevi različitih prečnika, izrađene od čelika P235TR1. Tvrdoća i mikrostruktura su analizirane na uzorcima isečenim iz cevi u zoni šava, da bi se odredio uticaj heterogenosti. Otpornost prema lomu materijala cevovoda, tj. oba osnovna metala i oba šava, je određena na osnovu ispitivanja epruveta oblika prstena sa oštrim koncentratorima napona, predloženih u prethodnim studijama. Poređenjem krivih otpornosti prema rastu prsline određene su razlike između dve ispitivane cevi, kao i uticaj heterogenosti izazvan postojanjem zavarenog spoja. Razmotren je uticaj oblika početnog koncentratora napona, oštrog žleba odnosno zamorne početne prsline.

Ključne reči: ispitivanje epruveta oblika prstena; mikrostrukturna analiza; tvrdoća zavarenog spoja; mehanika loma; nestandardne epruvete

Rubbing stability of printed innovative paper substrates containing cereal straw pulp

Irena Bates, Ivana Plazonić, Katja Petric Maretić and Maja Rudolf

University of Zagreb Faculty of Graphic Arts, Zagreb, Croatia

Abstract
Paper is one of the most important materials for packaging and the demand for this material is constantly increasing. The printing and packaging industries are researching alternative sources of fibre, to produce more environmentally friendly paper without compromising quality. As a packaging material, paper must meet high strength requirements, and it has to exhibit acceptable surface properties to preserve the printing quality. This research had two objectives: to produce paper made from pulp of recycled fibre reinforced with virgin straw fibre and to evaluate the print quality on such papers. Straw pulp used for this purpose was obtained from three cereal crops: wheat, barley, and triticale. The paper produced was printed by using five printing techniques. Rubbing stability was evaluated by the difference in colour and reflectance spectra before and after performing rub tests and a comparison was made for the best interaction of paper and ink determined by the printing technique. For the prints with the highest colour difference after the rub test, the surface of the rub test receptor (uncoated recycled paper) was examined for signs of ink transfer during the test and the areas of transferred ink coverage were calculated on their processed microscopic images.

Keywords: alternative fibre sources; durability; paper production; printing techniques; UV-curable black inks.

Available on-line at the Journal web address: http://www.ache.org.rs/HI/

1. INTRODUCTION

Packaging industry is rapidly developing, and its further growth is expected in the coming years [1]. At the same time, this industry sector is turning towards sustainable and environmentally friendly packaging solutions. Today, the ecological aspect of packaging is considered even more important than the economic one [2]. The evolving regulatory environment, increasing competition and changing consumer preferences for certain packaging solutions are just some of the challenges facing the packaging industry [3]. Therefore, substantial research is needed in this sector of printing industry to provide the market with sustainable, environmentally friendly and, at the same time, high-quality packaging that does not jeopardize quality of the packaged product or the environment that we leave as a legacy to future generations. One of the most important trends that will undoubtedly shape the future of packaging industry is the shift towards paper-based packaging solutions. Considering that paper packaging, unlike plastic, is not only biodegradable, but also recyclable, it represents a more sustainable option that is in line with the growing preferences for sustainable and environmentally friendly packaging options [4]. When it comes to packaging recycling, fibre-based packaging has the highest recycling rate in Europe amounting to 82 % and the goal is to reach 90 % recycling rate for fibre-based packaging by 2030 [5]. In general, the main raw materials used in pulp and papermaking industry can be classified into three categories: wood, non-wood, and non-plant (mainly waste paper) [6]. However, it should be kept in mind that wood as a forest resource is still the main source of cellulose fibres in the paper industry. Therefore, sustainably managed forests are crucial for our environment, as well as the transition to other lignocellulosic raw materials, which will reduce the amount of virgin wood fibres for the paper industry needs while providing the needed length and quality of the cellulose fibres. The recycling process incorporates removal of ink from printed papers to produce a fibrous

material called recycled pulp from which fibres are reprocessed and incorporated into new products, which provides the added value. Recycled pulp, however, is a mixture of different types of waste paper and varies in composition from source to source and from day to day from a single source. Variability of pulp raw materials which is increasing as the proportion of recycled fibres increases, is a very common problem for the packaging industry worldwide. It is therefore constantly faced with the challenge of ensuring a satisfactory strength of packages despite the increase in the recycled paper content as the main fibrous component. Nowadays, packaging grade papers contain 60-100 % recycled fibres [7, 8]. Recycled fibres tend to be broken or damaged and they have different physical properties than virgin fibres (*e.g.*, micro-fibrils on the fibre surface more likely tend to collapse) resulting in weaker inter-fibre bonding and consequently lower strength of paper or paper board products [7]. With each cycle of the recycling process, the fibres become shorter and more damaged, limiting their potential uses. To provide the crucial strength properties for paper packaging made from recycled fibres, a certain amount of fresh virgin fibres has to be incorporated into the pulp [9]. Although waste paper is the main raw material for paper production, it should be emphasized that without fresh virgin fibres, utilization of the recycled fibres would not be possible. Therefore, it is important to find alternative sources of virgin fibres for printing and packaging industries, to produce more environmentally friendly paper without compromising quality. Selection of packaging materials is very complex, as they have to fulfil various packaging functions, such as protecting the contents, conveying information about the products, and facilitating their transportation. Only the right combination of materials allows benefits such as longer durability and better protection against external damage. Research in this paper focuses on the possibility of substituting virgin wood fibres with the aim of refining recycled pulp in the production of packaging paper intended for printing. Evaluation of the possibility for using virgin fibres from cereal straw for this purpose was carried out after printing the produced innovative paper substrates with the addition of cereal straw pulp. Five printing techniques commonly utilized in the printing industry (digital, flexographic, offset, gravure, and screen printing) were used followed by exposure of the prints to rubbing at low pressure as a simulation of handling of this packaging.

2. MATERIALS AND METHODS

The research was conducted in four phases:
1. production of paper substrates on the laboratory scale with and without cereal straw pulp;
2. printing of paper substrates with UV-curable black inks by using five different printing techniques;
3. testing of rub resistance of the prints;
4. spectrophotometric measurements of the prints before and after the rub resistance tests to determine the difference in coloration.

2. 1. Production of paper substrates with cereal straw pulp

Circular paper substrates weighing 42.5±2.6 g/m^2 and 200 mm in diameter were produced in the laboratory by mixing recycled wood pulp from newsprint and unbleached wheat, barley, or triticale straw pulp in a weight ratio of 7:3 by a Rapid-Köthen sheet former (FRANK-PTI, Austria) according to the standard EN ISO 5269-2:2004 [10]. Straw was used as an alternative raw material to obtain cellulose pulps. Straw pulp of each crop type was prepared in laboratory conditions after straw was collected from fields in central Croatia immediately after harvest. In contrast to wood materials, there is less lignin in wheat straw [11] resulting in a more open structure that is more susceptible to reactions with alkalis. Sodium hydroxide used in soda pulping easily dissolves phenolic lignin structures. Therefore, alkaline pulping process was chosen as it provided straw pulp with good strength properties [12] which was needed for the purpose of this research. Namely, in this research, virgin straw fibres were used with the aim of refining recycled fibres, which were increasingly shortened and damaged by repeated recycling processes. Before cooking, foreign materials and grains were removed, and the straw of each crop was chopped to a length of 1 to 3 cm. Each type of straw was cooked under the same process conditions, which are kept constant during the soda pulping process [13]. Wheat (W), barley (B) and triticale (TR) straw was cooked separately by placing the materials in autoclave along with the classical reagent

(sodium hydroxide) at a 10:1 liquid/solid ratio and pulped by using the reagent concentration of 16 %, at a temperature of 120 °C and a pressure of 170 kPa for 60 min.

After pulping, the cooked material was washed to remove residual cooking liquor and fiberized in a Holländer Valley mill (AB Lorentzen & Wettre, Sweden) at 500 rpm for 40 min. The pulp was drained and allowed to dry to a moisture content of about 10 % at room temperature.

In total, at laboratory scale, four different types of paper substrates were produced with and without cereal straw pulp (used as a reference and marked with 100N). Table 1 lists abbreviations and contents of the paper substrates produced according to the type of pulp used.

Table 1. Laboratory produced paper substrates

Abbreviation	Amount of recycled wood pulp fibres, %	Amount of straw pulp fibres, % (cereal type)
100N	100	0
70N30W	70	30, wheat
70N30B	70	30, barley
70N30TR	70	30, triticale

2. 2. Printing of paper substrates with UV-curable inks

Printing of paper substrates was conducted by five common printing techniques to observe the interaction between inks, printing conditions and the produced paper substrates with added cereal straw pulp. All paper substrates were printed in full tone with black UV-curable inks that use polymerization of the ink as the drying (curing) technique when irradiated with UV light.

2. 2. 1 Digital ink-jet printing

Digital ink-jet printing was carried out on an EFI Rastek H652 UV-curable printer (EFI, USA, CA) with EFI propriety ink. Printing quality was set on high quality mode (8 passes) with a speed of 12.1 m^2/h and a resolution of 600×600 dpi. Fast drying was performed during printing under two mercury-based UV lamps with the power of 700 W.

2. 2. 2 Offset printing

Prints by offset printing technique were obtained on a Prüfbau multipurpose printability testing machine (Prüfbau, Germany) with SunCure Starluxe low migration UV-curable inks (Sun Chemical, USA, NJ). Printing conditions were set at a temperature of 23 °C and a relative humidity of 50 % with the printing speed of 0.5 m/s and a pressure of 600 N. Drying was performed immediately after printing by a Technigraf Aktiprint L 10-1 dryer (Technigraf, Germany), UV-C tube with a light source power of 120 W/cm and an intensity of 60 %.

2. 2. 3 Flexographic printing

Flexographic prints were made on an Esiproof (RK Print Coat Instruments Ltd, UK) laboratory device using UV-curable ink Solarflex Integra (Sun Chemical, USA, NJ) at a temperature of 23 °C and a relative humidity of 50 %. After printing, the prints were dried in the same manner as prints obtained by offset printing.

2.2.4. Gravure printing

Gravure printing was performed on a KPP Gravure system with (RK Print Coat Instruments Ltd, UK) with UV-curable ink Solarflex Integra (Sun Chemical, USA, NJ) at a temperature of 23 °C and a relative humidity of 50 %. Printing speed was 20 m/min, with using a 65 Shore impression roller and a 39.37 lines/cm engraving plate. Gravure prints were dried on the same device under the same drying conditions as for the offset and flexographic printing.

2. 2. 5. Screen printing

For screen printing, a semi-auto Shenzhen Juisun screen printing machine (Juisun, China) with a squeegee of a mechanical hardness of 75 Shore and a mesh line of 140 lines/cm was used. The prints (140×140 mm) were made with UltraGraph UVAR UV-curable inks (Marabu GmbH & Co.,Germany). All prints were printed at a temperature of 23 °C and a relative humidity of 50 %. After printing, the UV prints were dried in two passes by UV irradiation.

2. 3. Rub resistance testing of prints

One of the most important indicators of the quality of printed paper packaging is the stability to rubbing. Low quality prints have a tendency of smearing, scratching, or scuffing off the printed text or image when pressure or abrasion is applied [14], which is not acceptable for secondary packaging. Rubbing off is most noticeable in solid printed areas that come into contact with other surfaces [15] and the main factors affecting the amount of ink loss are the interaction between the ink and substrate, chemical composition of the ink, the drying process and the thickness of the applied ink layer [16]. Therefore, the goal was to obtain a similar ink layer thickness on solid areas on all paper substrates using different printing techniques. Yet, due to different ink transfer methods, it was impossible to obtain exactly the same ink layer thickness on each print. The rub resistance test was conducted by using a Hanatek T4 Rub and Abrasion Tester device (Rhopoint Instruments, UK) according to the standard BS 3110 [17]. Prior to testing, the prints were cut into round samples, 5 cm in diameter, and subjected to a pressure of 0.23 kg (0.5 lb) by 20, 40 and 60 circular movements at a speed of 1 rotation per second to simulate handling of this packaging. In addition to analysing spectrophotometric changes in the print after the rub stability test, surface of the opposite paper (receptor) used for rubbing was also analysed under microscope in order to determine the amount of printing ink transferred during the test. The microscopic images of the surface of the opposite paper taken by an optical microscope (Dino-Lite AM413T, Dino-Lite, Taiwan) after rubbing the print that had the least stability were analysed by ImageJ software, which was used to calculate the surface area of ink transferred to the opposite paper.

2. 4. Spectrophotometric measurements of prints

To evaluate the amount of the rubbed off ink from the surface of the paper substrate, the colour difference ΔE_{00}^* was calculated by using spectrophotometric measurements of CIE L*a*b* values before and after each cycle of rubbing tests. CIE L*a*b* values are chromatic scale values representing human colour perception, where L* value indicates the lightness, a* value indicates red-green component of a colour, and b* value indicates yellow-blue component of a colour. CIE L*a*b* values and spectral reflectance were measured by using the X-Rite SpectroEye device (X-Rite, USA, MI) under standard D50 illumination and a 2° observer. The measurements were performed on 50 printed paper substrates. The colour difference of the prints was calculated by equation (1) [18]:

$$\Delta E_{00}^* = \sqrt{\left(\frac{\Delta L'}{K_L S_L}\right)^2 + \left(\frac{\Delta C'}{K_C S_C}\right)^2 + \left(\frac{\Delta H'}{K_H S_H}\right)^2 + R_T \left(\frac{\Delta C'}{K_C S_C}\right)\left(\frac{\Delta H'}{K_H S_H}\right)} \tag{1}$$

Tolerance for the acceptable colour difference in the printing industry is based on a small noticeable colour difference by a standard observer with the value of $\Delta E_{00}^* \leq 2$ [19].

To confirm the visual results, the transfer of ink that rubbed off the prints was calculated as the percentage of black pixels in the processed microscopic images, which were converted to bitmaps with a threshold of 50 %.

To determine the colour changes on prints more clearly, the spectral reflectance was also analysed. It was measured for the visible part of the spectrum from 400 to 700 nm wavelength in steps of 10 nm. The reflectance spectra of all prints before and after the rubbing test were measured, and the results of reflectance measurements for prints with the highest ΔE_{00}^* are presented as ΔR according to equation (2):

$\Delta R = R_2 - R_1$ \hfill (2)

where: ΔR represents the spectral reflectance difference; R_2 represents the reflectance spectra after the rubbing test with 60 rotations, and R_1 represents the reflectance spectra before the rubbing test.

Statistical analysis of the obtained results was performed by calculating the one-way ANOVA method, with the probability value for significance ($p < 0.05$) using the OriginPro v2023b software.

3. RESULTS AND DISCUSSION

Since rub resistance is highly dependent on the thickness of the ink layer on the printing substrate, Table 2 shows the results of the optical ink density (D_i) of black prints with regard to the printing technique and the paper substrate.

Table 2. Optical ink density for printed paper substrates

Printed paper substrates	Optical ink density				
	Digital prints	Offset prints	Flexog. prints	Gravure prints	Screen prints
100N	0.96±0.01	0.96±0.01	1.14±0.01	1.18±0.02	1.24±0.03
70N30W	0.93±0.02	0.98±0.03	1.13±0.01	1.18±0.04	1.23±0.02
70N30B	0.90±0.01	1.02±0.02	1.13±0.01	1.07±0.03	1.22±0.01
70N30TR	0.91±0.02	1.01±0.02	1.10±0.01	1.10±0.06	1.27±0.04

The spectrophotometric colour difference calculated as ΔE_{00}^* was used to describe the best interactions between the black UV-curable ink and the paper substrate when printing by using five most commonly used printing techniques (digital, offset, flexographic, gravure, and screen printing). Lower values of colour difference represent better adhesion of the ink to the surface of the paper substrate and thus the higher rub resistance. Figure 1 shows the colour difference obtained from prints for all 5 printing techniques after the 20, 40 and 60 rotations in the rubbing test.
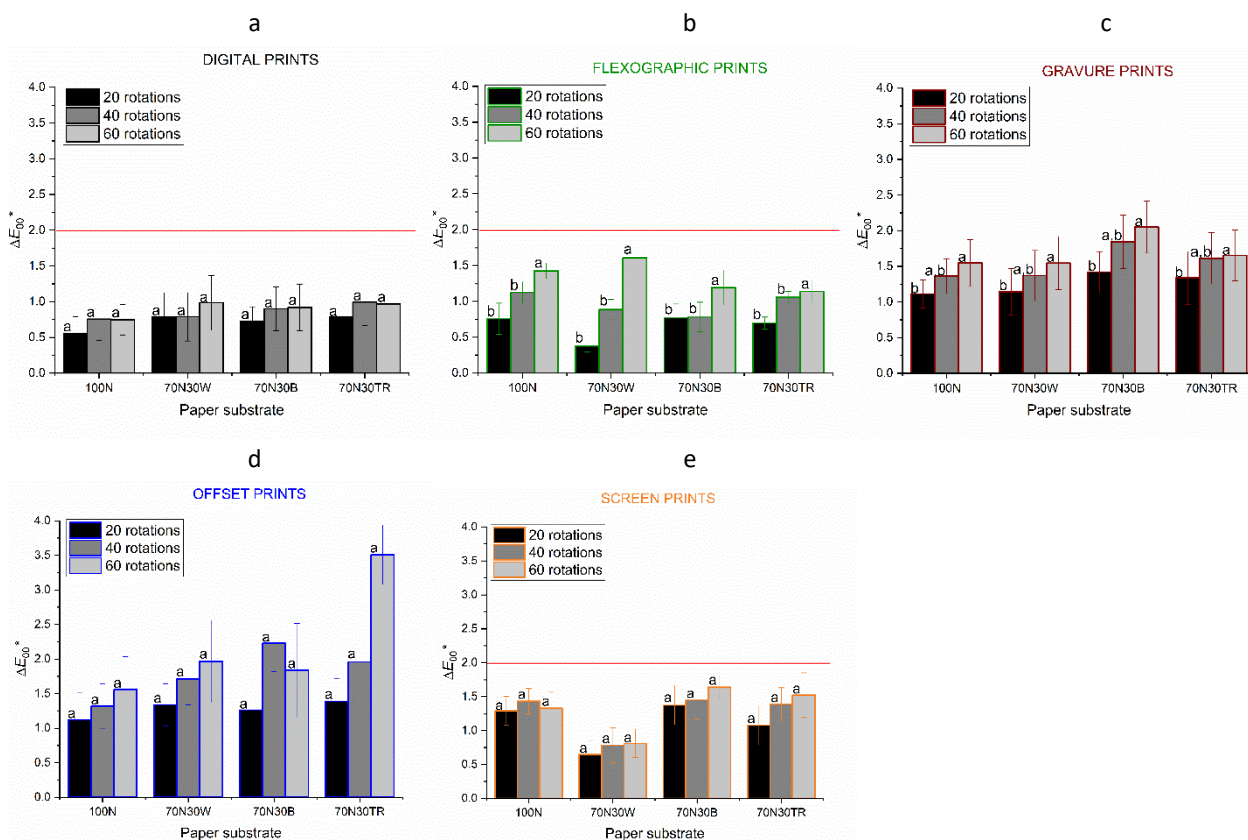
Figure 1. The colour difference (ΔE_{00}^*) of a) digital, b) flexographic, c) gravure, d) offset, and e) screen prints on paper substrates (100N, 70N30W, 70N30B, 70N30TR) after 20, 40 and 60 rotations in the rub resistance test; letters a and b designate statistically different values

The rub stability, evaluated by the colour difference ($\Delta E_{00}*$) calculated from CIE L*a*b* values before and after the rubbing tests, shows the lowest colour changes ($\Delta E_{00}* < 1$) for digital prints on all printing substrates regardless of the type of pulp used (Fig. 1a) even after prolonged rubbing cycles (up to 60 rotations). Similarly low values are obtained for the reference paper 100N without added straw pulp, as well as papers with 30 % addition of wheat, barley, or triticale pulp. The ANOVA analysis resulted in a significance level (marked "b", Fig. 1) only for flexographic and gravure prints at rotations of 20 and 40, while for all other prints the results were not significantly different when the prints are observed under the same rubbing conditions. Rub tests at higher number of rotations (40 and 60) show stable values of $\Delta E_{00}*$ that are the same or with a negligible difference compared to the first iteration of the test with 20 rotations. The flexographic prints also show good stability ($\Delta E_{00}* < 0.76$) to the initial impact of the rub resistance test of 20 rotations (Fig. 1b). The colour difference increases as the applied number of rubbing rotations is increased to 40 and 60 ($\Delta E_{00}* < 1.61$). The gravure prints (Fig. 1c) show greater $\Delta E_{00}*$ (ranging from 1.11 to 1.42) after the initial test of 20 rotations, with a relatively low increase of $\Delta E_{00}*$ (less than 2.05) in further iterations of the rub resistance test. For offset prints, while the initial impact of rub resistance (20 rotations) is comparable to gravure prints ($\Delta E_{00}*$ ranging from 1.12 to 1.39), greater variance and colour difference are observed with increasing the number of test rotations (Fig. 1d). Screen prints show good rub resistance at the initial 20 rotations ($\Delta E_{00}* < 1.37$) for all paper substrates, with the stable rub resistance under prolonged rubbing conditions ($\Delta E_{00}* < 1.63$). The best results are evident for the paper substrates with the wheat straw pulp addition (70N30W). It is certainly important to emphasize that regardless of whether the prints were made on paper substrates without or with triticale pulp, they had shown sufficient rub resistance after a cycle of 60 rotations, indicating the difference in colour that only an experienced observer can perceive. This is in correlation with the previous research of rub resistance estimated on digital UV prints on paper substrates with wheat straw pulp, where the amount of wheat straw pulp in the paper substrate had not significantly affected results [20]. Indeed, the type of ink was found to have a greater influence on the stability of the print during rubbing than the paper substrate itself [21].

Most prints, regardless of the paper substrates and printing techniques used, have colour difference values within the acceptable range (below $\Delta E_{00}* = 2$), which means that the colour difference cannot be perceived by an untrained eye. By comparing the print stability in relation to the type of straw pulp added in recycled wood pulp during the production of the paper substrates and the number of rotation cycles in the rubbing test performed, it can be seen that the most stable prints within 20 rotations of rub resistance tests are obtained on paper substrates with 30 % of wheat straw pulp when using the flexographic technique ($\Delta E_{00}* = 0.38\pm0.09$). The worst stability when simulating packaging handling ($\Delta E_{00}* = 1.39\pm0.33$) is observed for offset prints on papers substrates with 30 % of triticale pulp (Fig. 2a). When observing the mechanical resistance within 40 rotations (Fig. 2b), the best results are obtained for flexographic prints on the paper substrate with 30 % barley ($\Delta E_{00}* = 0.78\pm0.21$), but digital prints on the other substrates show similarly good results ($\Delta E_{00}*$ ranging from 0.75 ± 0.30 to 0.99 ± 0.33). The worst results are obtained for offset prints for all types of paper substrates with addition of cereal straw pulp (70N30W, 70N30B and 70N30TR) with $\Delta E_{00}*$ between 1.71 ± 0.37 and 2.22 ± 0.41, while the reference sample 100N showed the worst results with screen prints ($\Delta E_{00}* = 1.43\pm0.19$).
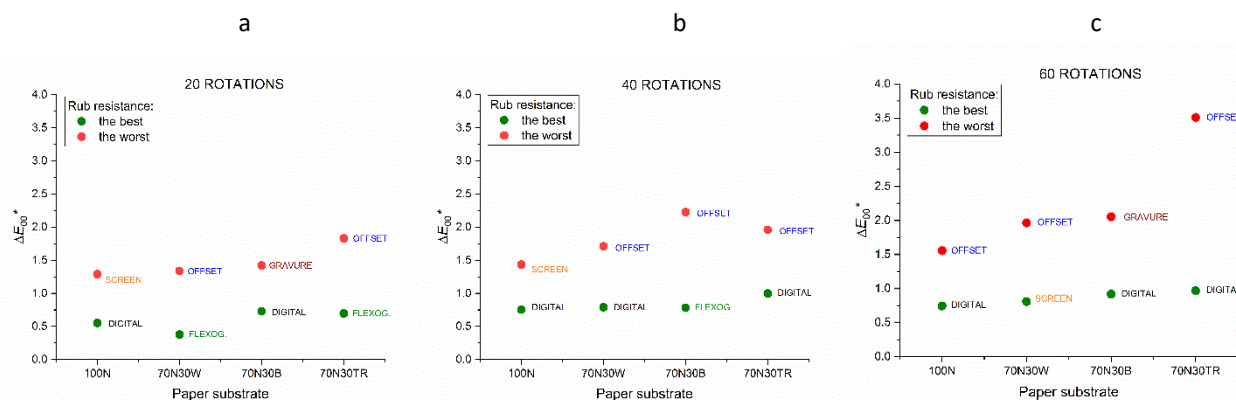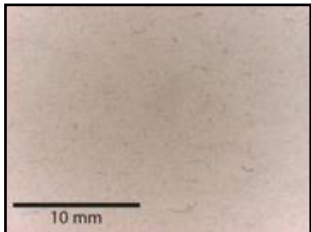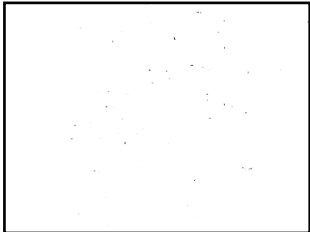

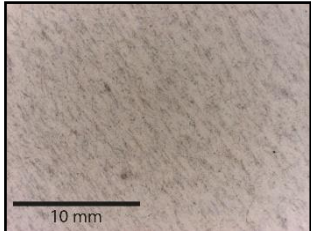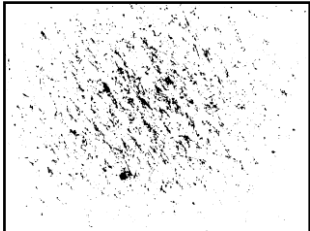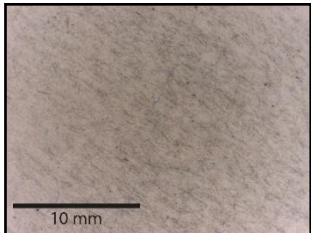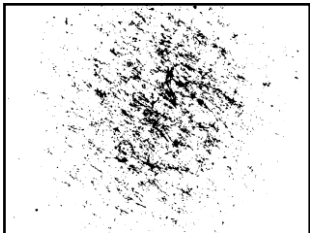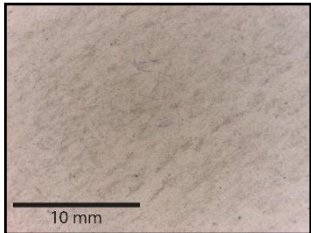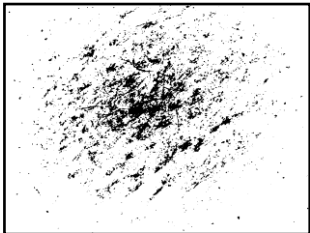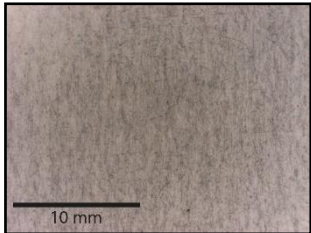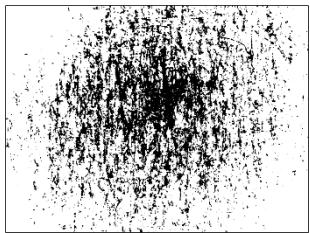
Figure 2. Comparison of the best and the worst colour differences $\Delta E_{00}*$ for three rub resistance iterations: a) 20 rotations, b) 40 rotations and c) 60 rotations

The best stability in the longest rub resistance test performed with 60 rotations (Fig. 2c) was shown for digital prints with similar results for the reference sample 100N (ΔE_{00}^* = 0.75±0.22) and papers with 30 % barley (ΔE_{00}^* = 0.92±0.32) or triticale straw pulp (ΔE_{00}^* = 0.97±0.27) as well as for screen prints on the paper substrate with added wheat straw pulp (ΔE_{00}^* = 0.81±0.21). The worst stability results, again, are determined for offset prints on most printing substrates (ΔE_{00}^* between 1.56±0.48 and 3.51±0.43).

Further examination of the worst evaluated prints after 60 rotations of the rubbing test was conducted by analysing the transferred ink from prints to the opposite uncoated recycled paper that served as the contact surface in the rubbing tests. First, a visual examination was performed on the microscopic images that recorded the transferred ink. Table 3 shows the original and analysed images of opposite paper surface (uncoated unprinted recycled paper) with the traces of ink from the prints after rubbing (60 cycles) and their percentages.

Table 3. Originally acquired and analysed images of the opposite uncoated recycled paper used as a receptor (a), and images and surface coverage by ink transferred after 60 rotations in the rubbing test for prints which showed the worst rub resistance 100N offset (b), 70N30W offset (c), 70N30B gravure (d) and 70N30TR offset (e)

	Original micrograph	Analysed micrograph	Surface coverage by transferred ink, %
a)			0.05
b)			5.02
c)			7.70
d)			8.84
e)			21.71

From the analysed image of the opposite paper surface (Table 3a) that was used as a receptor during rubbing tests, the area covered with ink was 0.05 %. This very small percentage could come from the ink remaining in the paper pulp during the recycling process. The lowest percentage of ink coverage (~5 %) was observed on the receptor surface after performed rubbing test of offset print on the paper 100N without the addition of straw pulp (Table 3b). Very similar coverage by the transferred ink (7.7 and 8.8 %) were observed on the surfaces of the receptor after the rubbing test of offset print on the paper 70N30W with 30 % wheat straw (Table 3c) and gravure print produced on the paper 70N30B with 30 % barley pulp (Table 3d). The highest percentage of ink transfer (21.7 %) was observed on the opposite paper surface after the rubbing test of offset printing on paper with 30 % triticale pulp (Table 3e).

Figure 3 shows the difference in the reflectance spectrum (ΔR) of the prints with the highest ΔE_{00}^* after 60 circular motions.
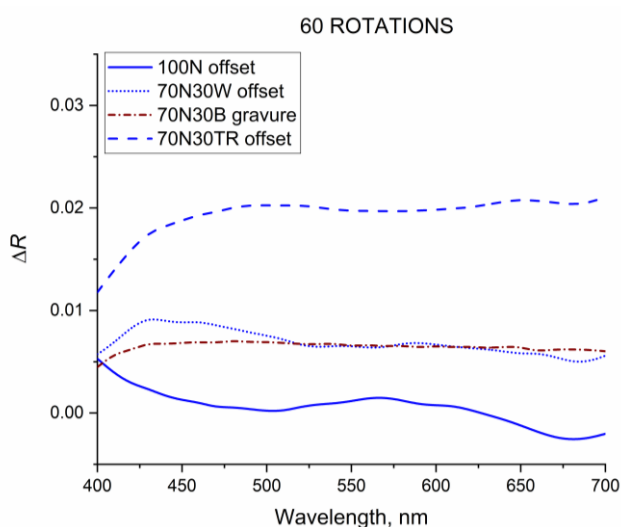

Figure 3. Differences in the reflection of the print (ΔR) which have shown the worst rub resistance after 60 rotations

In general, after performed rubbing test, the reflection of black prints increased slightly in the entire visible part of the spectrum. Namely, rubbing reduces the ink layer on the paper surface to a greater or lesser extent, causing light absorption to decrease and light reflection to increase. As a result of rubbing the print, the smallest difference in reflectance was observed for the printing substrate without straw pulp printed by the offset printing technique (100N). Very similar differences in reflectance were detected for offset print on the paper with 30 % wheat straw (70N30W) and gravure print on the paper with 30 % barley pulp (70N30B), while the highest difference in reflectance was observed after the rubbing test of offset print on the paper with 30 % triticale pulp (70N30TR). The obtained results additionally confirm the colour change shown in Figure 2c and calculated percentage of ink transfer to the receptor surface (Table 3).

4. CONCLUSION

By comparing the stability of UV-curable inks applied by different printing techniques on innovative paper substrates obtained by the addition of cereal straw pulp from wheat, barley, or triticale crops to reinforce pulp from recycled fibres, it can be concluded that digital prints are the most stable to rubbing based on the lowest colour differences even with prolonged rubbing treatment. Screen print had a slightly higher colour differences than digital prints, but again stability over longer rub cycles was good. Flexographic prints showed better stability under initial rubbing conditions simulating hand pressure and daily package handling (similar to digital prints) but deteriorated slightly under prolonged rubbing. The worst results were observed for the offset prints with the highest colour changes at the initial rubbing conditions, which can be compared to the colour changes of gravure prints. However, longer rubbing conditions showed greater colour differences indicating poorer acceptance of the ink on the paper substrate. Surface coverage by the transferred ink on the receptor surface (opposite uncoated recycled paper) after rubbing tests was in correlation with the difference

in spectral reflectance. Offset prints on paper containing triticale straw pulp showed higher reflectance difference and greater ink transfer after rubbing test. Gravure prints on paper containing barley straw pulp and offset prints on paper containing wheat straw pulp showed similar reflectance difference and ink transfer. According to the conducted research, it is possible to conclude that all the examined prints have an acceptable quality and stability according to the tolerance standards of the printing industry. Since production of the paper substrates was carried out at the laboratory level, it is necessary to perform surface improvements such as smoothing or coating for offset printing with low-migration inks. These processes would significantly improve the adhesion of the ink to the paper surface, which is an area for further research.

REFERENCES

[1] Marinova V. Trends in Packaging Sector. *Izvestia*. 2021; 10(1): 3-13. https://doi.org/10.36997/IJUSV-ESS/2021.10.1

[2] Petljak K, Naletina D, Bilogrević K. Considering ecologically sustainable packaging during decision-making while buying food products. *Econ Agr*. 2019; 66(1): 107-126. https://doi.org/10.5937/ekoPolj1901107P

[3] Asim Z, Shamsi IRA, Wahaj M, Raza A, Abul Hasan S, Siddiqui SA, Aladresi A, Sorooshian S, Seng Teck T. Significance of Sustainable Packaging: A Case-Study from a Supply Chain Perspective. *Appl Syst Innov*. 2022; 5(6):117. https://doi.org/10.3390/asi5060117

[4] Oloyede OO, Lignou S. Sustainable Paper-Based Packaging: A Consumer's Perspective. *Foods.* 2021; 10(5):1035. https://doi.org/10.3390/foods10051035

[5] Parkinson L. Associations report European packaging recycling rates, *Food packaging forum*, 2022. https://www.foodpackagingforum.org/news/associations-report-european-packaging-recycling-rates Accessed April 27, 2023.

[6] Liu Z, Wang H, Hui L. Pulping and Papermaking of Non-Wood Fibers, *InTech 2018*, https://www.intechopen.com/chapters/62223, Accessed April 27, 2023. http://dx.doi.org/10.5772/intechopen.79017

[7] Adamopoulos S, Oliver JV. Fiber Composition of Packaging Grade Papers as determined by the Graff "C" Staining Test. *Wood Fiber Sci*. 2006; 38(4): 567-575. ISSN 0735-6161. https://wfs.swst.org/index.php/wfs/article/view/2111

[8] Adamopoulos S, Martinez E, Ramirez D. Characterization of packaging grade papers from recycled raw materials through the study of fibre morphology and composition. *Global NEST* . 2013; 9(1):20-28. https://doi.org/10.30955/gnj.000384

[9] Hubbe MA, Venditti RA, Rojas OJ. What happens to cellulosic fibers during papermaking and recycling? A review. *BioResources*. 3(4); 2007: 739-788. https://doi.org/10.15376/biores.2.4.739-788

[10] ISO 5269-2, Pulps — Preparation of laboratory sheets for physical testing — Part 2: Rapid-Köthen method, 2004

[11] Fang G, Shen K. Wheat Straw Pulping for Paper and Paperboard Production. In: Fahad S, Basir A, Adnan M eds. *Global Wheat Production.* InTechOpen 2018. http://dx.doi.org/10.5772/intechopen.77274

[12] Sood YV, Kapoor SK. Modified soda pulping of wheat straw-(Triticum volgare). *IPPTA*. 1984; 21:1-6.

[13] Plazonić I, Bates I, Barbarić-Mikočević Z. The Effect of Straw Fibers in Printing Papers on Dot Reproduction Attributes, as Realized by UV Inkjet Technology. *BioResources*. 2016;11(2): 5033–5049. https://doi.org/10.15376/biores.11.2.5033-5049

[14] Zhou WH, He BH, Zhang CX, Han Y. Analysis on Ink Layer Rub Resistance for Coated Paper Prints. *Adv Mater Res*. 2011; 380:173-178. https://doi.org/10.4028/www.scientific.net/amr.380.173

[15] Koivula H, Gane P, Toivakka M. Influence of ink components on print rub. *Nordic Pulp & Paper Research Journal*. 2008; 23(3): 277-284. https://doi.org/10.3183/npprj-2008-23-03-p277-284

[16] Kipphan H. Fundamentals. In: *Handbook of Print Media*. Berlin, Heidelberg: Springer. 2001. https://doi.org/10.1007/978-3-540-29900-4

[17] BS 3110, Methods for measuring the rub resistance of print, 2017

[18] Sharma G, Wu W, Dalal EN. The CIEDE2000 color-difference formula: Implementation notes, supplementary test data, and mathematical observations. *Color Res Appl*. 2004; 30(1): 21-30. https://doi.org/10.1002/col.20070

[19] Bates I, Plazonić I, Petric Maretić K, Rudolf M, Radić Seleš V. Assessment of the UV inkjet ink penetration into laboratory papers within triticale pulp and its influence on print quality. *Color Technol*. 2022; 138: 16– 27. https://doi.org/10.1111/cote.12563

[20] Rudolf M, Petric Maretić K, Bates I, Plazonić I, Radić Seleš V. Assessment of durability of inkjet prints on laboratory paper substrates with wheat pulp based on rub resistance. *Eur. J Eng Sci Tech..* 2020; 5(1): 72-77. ISSN 2458-8156.

[21] Rudolf M, Plazonić I, Bates I, Radić Seleš V, Petric Maretić K. Evaluation of the rub resistance of offset UV ink layers on papers with wheat pulp, *Proceedings of the 6th International Conference on Design and Graphic Arts (CIDAG) Alameda. Revista de Educação, Artes e Ciências*, Lisabon, Portugal, 2021; 33-39. ISBN 9770016459949.

Otpornost na otiranje otisnutih inovativnih papirnatih podloga s pulpom slame žitarica

Irena Bates, Ivana Plazonić, Katja Petric Maretić i Maja Rudolf

Sveučilište u Zagrebu Grafički fakultet, Zagreb, Hrvatska

(Naučni rad)

Izvod

Papir je jedan od najvažnijih materijala za pakovanje i potražnja za njim je u stalnom porastu. Grafička industrija i industrija pakovanja neprestano istražuju alternativne izvore vlakana kako bi proizveli ekološki prihvatljiviji papir bez ugrožavanja kvaliteta. Papir kao ambalažni materijal mora ispunjavati visoke zahteve za čvrstoću, ali mora imati i prihvatljive površinske karakteristike kako bi se očuvao kvalitet štampe. Proizvodnja papirnih podloga od pulpe recikliranih vlakana ojačanih primarnim vlaknima slame žitarica te ocenjivanje kvaliteta štampe na takvim papirima dva su cilja ovog istraživanja. Pulpa za ovu svrhu dobivena je od slame tri žitarice: pšenice, ječma i pšenoraži. Otisci na papirnim podlogama dobijeni su primenom pet tehnika štampe. Stabilnost otisaka na trljanje je procenjena na osnovu izračunate razlike u boji i refleksiji od kolorimetrijskih vrednosti otisaka izmerenih pre i posle ispitivanja mehaničke otpornosti, te je načinjeno poređenje rezultata za predlog tehnike štampe koja će dati najstabilniji otisak na papirnim podlogama. Za otiske sa najvećom razlikom u boji u testu otiranja, površina receptora za test otiranja ispitana je na znake prenosa boje tokom testa, a površine pokrivenosti prenosa boje izračunate su na njihovim obrađenim mikrografijama.